Investigation of Half-Metallic Ferromagnetism in NiMnSb Spin Dependent Tunnel Junctions

by

Clifford Takashi Tanaka

B.S., Physics
Carnegie Mellon University (1994)

S.M., Materials Science & Engineering
Massachusetts Institute of Technology (1996)

Submitted to the Deparment of Materials Science & Engineering in Partial Fulfillment of the Requirements for the Degree of

Doctor of Philosophy in Materials Science & Engineering
at the
Massachusetts Institute of Technology

September 1999

Signature of Author_____
Department of Materials Science & Engineering
August 5, 1999

Certified by_____
Dr. Jagadeesh S. Moodera
Research Scientist
Thesis Supervisor

Certified by_____
Ronald M. Latanision
Professor of Materials Science and Engineering
Thesis Co-Supervisor

Accepted by_____
Linn W. Hobbs
John F. Elliott Professor of Materials
Chair, Departmental Committee on Graduate Students

INVESTIGATION OF HALF-METALLIC FERROMAGNETISM IN NiMnSb SPIN DEPENDENT TUNNEL JUNCTIONS

by

CLIFFORD TAKASHI TANAKA

Submitted to the Department of Materials Science & Engineering
on August 5, 1999 in partial fulfillment of the
requirements for the
Degree of Doctor of Philosophy in Materials Science & Engineering

ABSTRACT

A study of spin dependent tunneling with epitaxial NiMnSb as an electrode is presented. This material is theoretically predicted to have fully spin-polarized conduction electrons, which is of great interest for magnetoelectronic devices. In this work, we address this prediction by fabricating spin dependent tunnel junctions capable of directly measuring the spin-polarization of the NiMnSb conduction electrons. Growth of multilayer structures such as tunnel junctions with this complex material presents a considerably greater challenge compared with normal ferromagnetic materials like Fe, Co and Ni. Since the major difficulty with this material is actually forming the desired structure, we studied extensively the growth of NiMnSb in order to determine the optimum growth conditions. Epitaxial NiMnSb thin films were grown by molecular beam epitaxy on MgO (001) substrates with V seed layers, and characterized by Auger electron spectroscopy, x-ray diffraction, atomic force microscopy and magnetometry.

In order to obtain direct information about the conduction electron spin-polarization of NiMnSb, tunnel junctions consisting of NiMnSb/Al_2O_3/Al and NiMnSb/Al_2O_3/$Ni_{80}Fe_{20}$/CoO multilayers were fabricated. The superconducting Al electrode in the former junctions was used as a spin detector to measure the spin-polarization (P) of the NiMnSb conduction electrons. This measurement revealed a P of 28%, in contrast to the predicted 100%. Transport measurements on the NiMnSb/Al_2O_3/$Ni_{80}Fe_{20}$/CoO junctions showed magnetoresistance consistent with this value of P. The low P value probably reflects spin-scattering at the ferromagnet/insulator interface, since tunneling is extremely sensitive to the quality of this interface. In comparison, a less interface sensitive technique, point contact Andreev reflection, which uses ballistic transport across a ferromagnet/superconductor interface, shows a P of 58% for the NiMnSb films. The reduced P may also reflect the influence of defects, especially those at the surface. These include threading dislocations, as well as disorder in the atomic arrangement in the NiMnSb unit cell. Recent theoretical calculations have shown that even a few percent of the latter disorder can close the minority spin energy gap and reduce the spin-polarization dramatically.

Thesis Supervisor: J. S. Moodera, Research Scientist

Thesis Co-Supervisor: Ronald M. Latanision, Professor of Materials Science & Engineering

Table of Contents

List of Figures

List of Tables

Acknowledgements

There are a number of people who made by experience at M.I.T. deeply rewarding. First and foremost, my advisor Dr. Jagadeesh Moodera, who continually encouraged me to reach my full potential. I have learned a tremendous amount of knowledge from him, and for that, I will be forever grateful.

I am also deeply indebted to Dr. Janusz Nowak, whose arrival really put this project on the right track. His technical skills were of incalculable value, and his love of science was truly an inspiration In addition, his open and friendly personality contributed immensely to the atmosphere of our laboratory.

Special thanks go to Patrick LeClair, who was always willing to trade ideas with me on our respective projects.

The Dutch contingent passing through our lab also deserve thanks. Drs. Ronnie Jansen and Rene van de Veerdonk brought an exceptional amount of knowledge in tunneling and physics in general to our lab. Listening to their heated discussions in the coffee room was always entertaining and enlightening.

A number of others at MIT who contributed to my MIT experience: Professor Ronald Latanision for his encouragement and his support within the DMSE. Professors Gene Fitzgerald and Caroline Ross for their useful input. Fellow grad student Michelle Corte-Real who certainly made the lab interesting the short time she was here. The grizzled veteran of the FBML, Dr. Simon Foner who was always a source of great insight into magnetism and experimentation, as well as into life in general. Meanwhile, the UROPs, Shikha Gupta, Barry Davis and Steve Tobias provided their youthful enthusiasm to the lab. Thanks to Dr. Geetha Berrera and Minha Hwang for taking the time to assist me with the VSM measurements, and Dr. Tae Hee Kim for carefully reviewing this document.

Thanks also go to our collaborators on parts of this project, Drs. Robert Soulen and Boris Nadgorny at the Naval Research Lab for their work on the Andreev reflection data, and Professor Roger Kirby's group at the University of Nebraska-Lincoln for magneto-optical work.

Thanks also to Dr. Kristl Hathaway at the Office of Naval Research for her belief in and support of this work.

Finally, I would like to thank my parents, whose love and support allowed me to grow into the person I am now.

Introduction

Spin dependent transport in magnetic multilayers, e.g. giant magnetoresistive (GMR) multilayers and magnetic tunnel junctions (MTJs), has attracted significant interest in recent years for magnetoelectronic applications, including magnetic sensors in hard drives and magnetic random access memory (MRAM) elements. These devices rely on changes in the resistance of the multilayer in response to a magnetic field, i.e., its magnetoresistance (MR). As sensors in hard drive read heads, their high sensitivity has enabled higher storage densities to be achieved. In addition, in MRAMs, these devices have a number of key advantages over current semiconductor based memory. For example, they are radiation hard and nonvolatile, important for mission critical applications such as in space and defense. They also have the potential for densities comparable to DRAM yet operating at speeds faster than high-speed SRAM.

The spin of the electron plays a fundamental role in the operation of magnetic multilayers, and one of the key parameters affecting the magnitude of the MR is the degree of spin-polarization (P) of the conduction electrons in the ferromagnetic layers. P here is defined as

$$P = \frac{n_\uparrow - n_\downarrow}{n_\uparrow + n_\downarrow},$$

where $n_\uparrow$ and $n_\downarrow$ are the number of spin up and spin down electrons, respectively in the ferromagnet (FM). It is thus of great importance to develop materials with high P. In 1983, a promising new class of FMs for spin transport devices was identified from theoretical band structure calculations by deGroot *et al.* [1] on the Heusler alloys NiMnSb and PtMnSb. These calculations predicted that the conduction electrons in these materials were 100% spin-polarized. These were called half-metallic ferromagnets (HMF), since they showed simultaneously metallic

behavior for the majority spin up electrons and semiconducting behavior for the minority spin down electrons. Since then, a number of other HMFs have been identified, at least theoretically, including CrO_2, Fe_3O_4, and $La_{0.67}Sr_{0.33}MnO_3$. Experimental confirmation of HMF has proven difficult, however.

The prediction by de Groot could have important applications in magnetoelectronic devices. For example, a 100% spin-polarized material allows for devices with virtually infinite magnetoresistance to be achieved, *i.e.*, a device which is insulating in one state and conducting in the other. This would allow for magnetic sensors of orders of magnitude higher sensitivity than sensors with convential ferromagnetic materials. In addition, higher density and higher speed magnetic memories could potentially be reached using such materials. Furthermore, in the case of MTJs, some of the fundamental limitations of these devices can be eliminated by using HMF electrodes, in particular the bias voltage dependence of the magnetoresistance.

The focus of this work then was to test the prediction of half-metallic ferromagnetism in the Heusler alloy NiMnSb. This was accomplished by spin dependent tunneling in planar tunnel junctions with this material. Two types of junctions were fabricated, ferromagnet-insulator-superconductor (FM/I/SC) and ferromagnet-insulator-ferromagnet (FM/I/FM) tunnel junctions. The former configuration has been used extensively to measure the conduction electron spin-polarization for a wide number of ferromagnetic materials. In contrast, the latter system has only been successfully grown in the past few years, but has undergone intensive research due to their potential for applications.

This thesis is organized as follows. Chapter 1 gives an overview of spin dependent tunneling (SDT), forming the theoretical basis for this work, while Chapter 2 discusses the

phenomenon of half-metallic ferromagnetism, both theoretical and experimental aspects. These two chapters reveal the challenges faced in fabricating spin dependent tunnel junctions, particularly in the case of this compound NiMnSb, and the materials requirements necessary to achieve success in this project. Chapter 3 gives the details of the NiMnSb film growth and characterization, with particular attention paid to producing films suitable for making tunnel junction. Chapter 4 presents the process of tunnel junction fabrication as well as the spin-tunneling measurements. These measurements determine the spin-polarization of the NiMnSb and are the litmus test for half-metallic ferromagnetism in the films. Chapter 5 provides the conclusions and ideas for further study to build on this work.

Chapter 1: Spin dependent tunneling

Electron tunneling is one of the most fundamental of quantum mechanical phenomena and has been used to investigate various properties of semiconductors, superconductors and magnetic materials. Particularly interesting is the electron spin dependent transport in the latter two classes of materials. Much of the progress in spin dependent tunneling has taken place at the M.I.T. Francis Bitter Magnet Lab, starting from the 1970s to the present.

The basic picture of a planar metal/insulator/metal (M/I/M) tunnel junction can be modeled as shown in Figure 1.1. Brinkman et al [2] formulated the theoretical tunnel current for such a trapezoidal barrier, a theory which has proven useful in evaluating the quality of tunnel barriers. The tunneling probability (P) can be estimated by the Wentzel-Kramers-Brillouin (WKB) approximation [3]

$$P(E) = \exp\left(-2 \cdot \int_0^d \left[\frac{2 \cdot m \cdot (U(x) - E)}{\hbar^2} \right]^{1/2} dx \right), \qquad (1.1)$$

where d is the barrier width, m is the mass of the electron and U(x) is the energy of the tunnel barrier conduction band above the Fermi energy (E_F). The current is then given by [2]

$$I(V) = \frac{4\pi e A}{\hbar} \sum_{k_t} \int_{-\infty}^{\infty} dE \cdot P(E) \cdot [(f(E) - f(E - eV)], \qquad (1.2)$$

where A is the junction area, k_t is the transverse momentum and f is the Fermi distribution function. For a trapezoidal barrier at moderate bias voltages with d > 10 Å [2],

$$J(V) = 3.16 \times 10^{10} \left(\frac{\phi^{1/2}}{d} \right) \exp\left(-1.025 \phi^{1/2} d \right) \times \left[V - \frac{0.0427}{2} \left(\frac{d\Delta\phi}{\phi^{3/2}} \right) V^2 + \frac{0.0328}{3} \left(\frac{d^2}{\phi} \right) V^3 \right], \qquad (1.3)$$

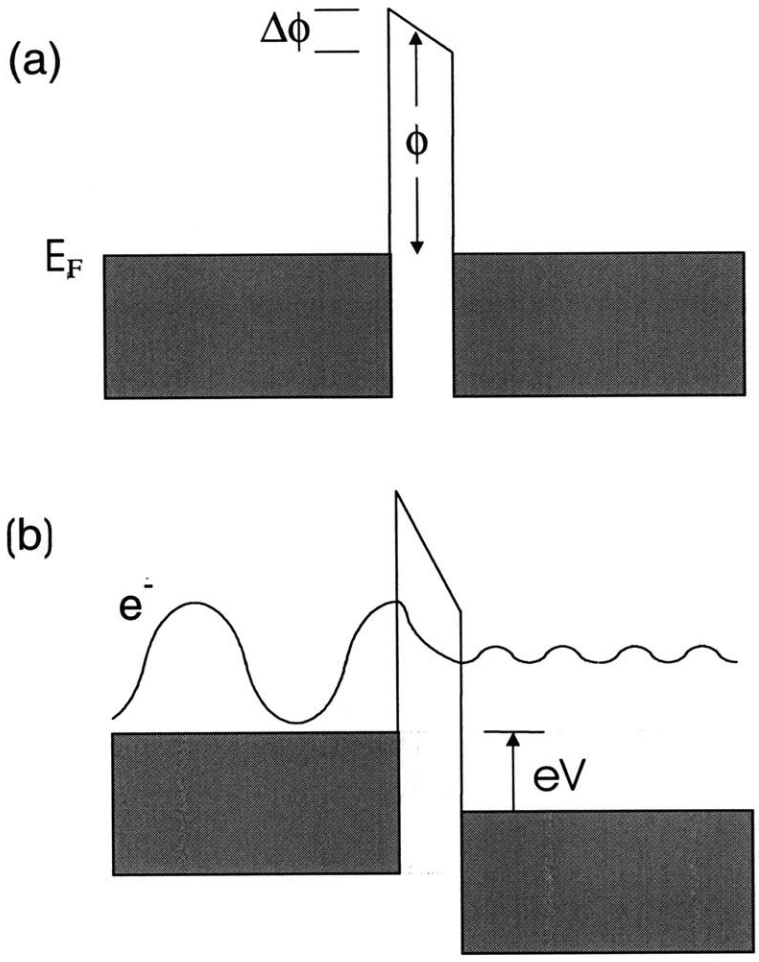

Figure 1.1: Band diagram for Metal/Insulator/Metal tunnel junction. a) at equilibrium. b) under applied voltage

where ϕ and $\Delta\phi$ are the average barrier height and the barrier asymmetry (ϕ_{left}-ϕ_{right}), respectively, in eV, d the barrier thickness in Å, and J the current density in A cm^{-2}.

The above expression for the current density shows no dependence on the density of states of the electrodes. However, intuitively one expects such dependence to exist. This dependence is stated by Fermi's golden rule – the number of tunneling electrons at a given energy is proportional to the product of the density of occupied states in one electrode and the density of empty states in the other. For a junction consisting of two normal metal electrodes, as shown in Fig. 1.2, the number of occupied states able to tunnel to empty states is simply linear with the voltage, yielding ohmic behavior [4]. One of the most beautiful manifestations of the density of states in tunneling is when one of the electrodes is a superconductor, an experiment first done by Giaver [5]. The density of states of a superconductor (N_S), as formulated by Bardeen, Cooper and Schriefer, was predicted to have an energy gap at the Fermi energy (E_F).[6] Formally, N_S at T=0 is expressed as

$$N_S(E) = \begin{cases} N_N(E) \cdot \left[E / (E^2 - \Delta^2)^{1/2} \right] & |E| \geq \Delta \\ 0 & |E| \leq \Delta \end{cases}, \qquad (1.4)$$

where N_N is the normal metal density of states and 2Δ is the gap energy. Consider a normal metal/insulator/superconductor tunnel junction. Both the normal metal density of states and the tunneling probability can be assumed to be constant over the range of interest since Δ is on the order of millivolts. The current is then given by [4]

$$I = B \cdot \sum_{k_t} \int_{-\infty}^{\infty} dE \cdot N_S(E) \cdot \left[f(E + eV) - f(E) \right], \qquad (1.5)$$

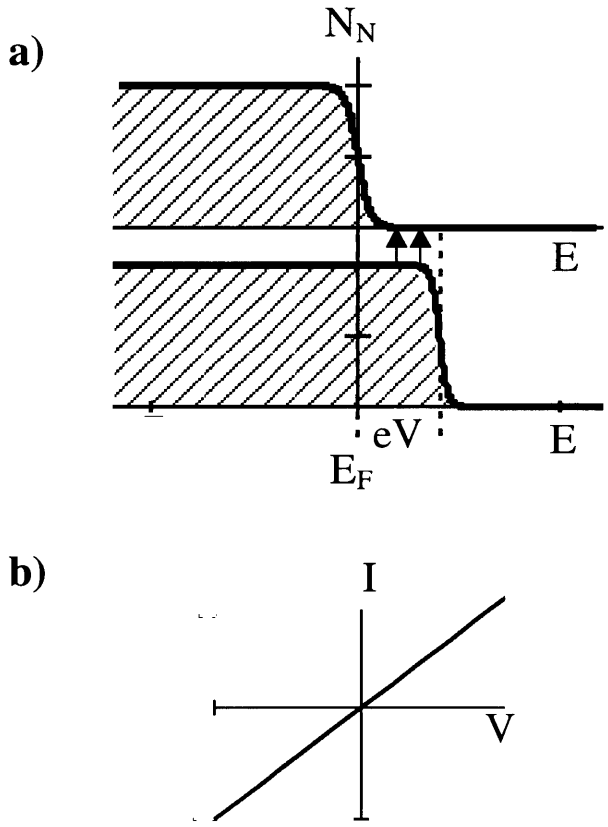

Figure 1.2: Metal/Insulator/Metal Junction a) Densities of states under applied voltage b) Resulting linear I-V curve at low bias

where B is the constant term in Eqn.(1.2). At voltages (V) below (Δ/e), there is little current flow due to the absence of available states in the superconductor. When the voltage is just above Δ, the current rapidly increases due to the divergence of N_S at $\pm\Delta$. Further increase in voltage eventually reaches a linear dependence of current on V. This behavior becomes clearer when considering the dynamic conductance (dI/dV) [4]

$$\frac{dI}{dV} = B \cdot \int_{-\infty}^{\infty} dE \cdot N_S(E) K(E + eV), \tag{1.6}$$

$$K = \frac{\beta \cdot \exp[\beta \cdot (E + eV)]}{\left\{1 + \exp[\beta \cdot (E + eV)]\right\}^2}, \tag{1.7}$$

where β=1/kT. The dynamic conductance can then be considered as a convolution of the superconductor density of states and a temperature dependent kernel K. This is illustrated in Figure 1.3. Graphically, as K is shifted by the applied voltage, dI/dV is given by the overlap of K with N_S.

Before considering the phenomenon of spin dependent tunneling, a few words should be said regarding superconductors and, in particular, the influence of an applied field on them. Meservey and Tedrow in their review (Ref. 4) present an excellent survey of superconductivity as it relates to spin-polarized tunneling. We restrict the discussion here to type I superconductors, with long coherence lengths compared to their penetration depth, *i.e.* pure element superconductors with low critical temperatures (T_c) and long electron mean free paths, as opposed to the high T_c type II variety, which have shorter coherence lengths. The reason for this is that the former has proven more successful in observing spin effects in tunnel junctions, as discussed in Ref. 4.

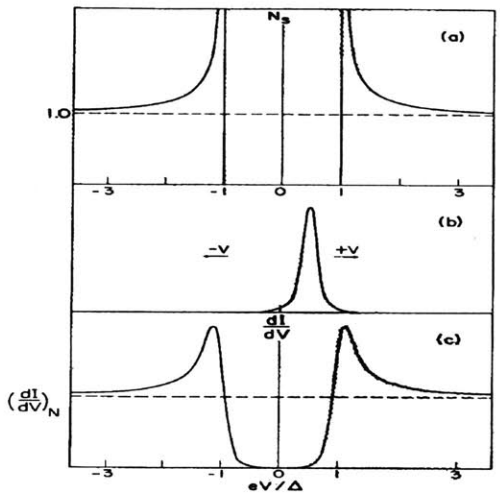

Figure 1.3. Superconductor/normal metal tunneling. (a) BCS density of states of superconductor. (b) Temperature-dependent kernel in the integral expression for dI/dV. (c) Theoretical normalized conductance dI/dV. Voltage is measured from the Fermi energy of the superconductor. After [4].

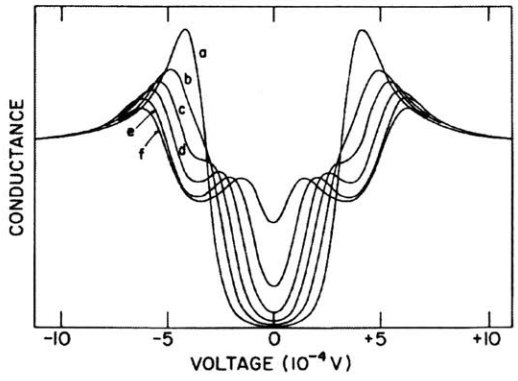

Figure 1.4: Zeeman splitting in superconductor/normal metal tunneling. Conductance versus voltage for an $Al/Al_2O_3/Ag$ tunnel junction in magnetic field H applied parallel to the film plane. Symbols on curves correspond to H in tesla: a=0, b=1.5, c=2.24, d=2.99, e=3.72, and f=4.31 [4].

It is in reality rather surprising that spin effects can be observed in these superconductors at all. The reason for this is that a bulk superconductor under a magnetic field exhibits perfect diamagnetism, resulting from surface currents induced by the magnetic field. This is the well known Meissner effect, in which the applied field is exactly cancelled in the superconductor by these surface currents, which extend into the superconductor to a penetration depth λ, typically $\sim 10^{-6}$ cm. At the critical field $H_C(T)$, the energy of the surface currents exceeds the condensation energy of the superconducting state. The surface currents then disappear, and the superconductor undergoes a first order phase transition to the normal state.

The situation changes drastically for a superconducting thin film with thickness much less than λ. In this case, the screening currents are greatly reduced, and a magnetic field applied in the plane of the film is able to fully penetrate the superconductor. As a result, the critical field is considerably larger in the thin film compared to the bulk, and at high magnetic fields, the interaction of the electron spins in the superconductor with the field can be observed [4]. This effect was seen by Meservey and Tedrow, who observed the Zeeman splitting of the superconductor in $Al/Al_2O_3/Ag$ tunnel junctions [7]. With a field applied precisely in the film plane, the dI/dV vs. V of the junction shows that each of the two zero field peaks in the dI/dV are spin split by the field, giving a total of four peaks, as shown in Fig. 1.4. The amount of the splitting between the spin up and spin down electrons was found to be simply the Zeeman energy $2\mu H$. It should be noted that in addition to this important discovery, this experiment and other series of experiments by then proved another key feature of tunneling, *i.e.*, the spin conservation in the tunneling process.

Subsequently, the Zeeman splitting has been observed in a variety of superconductors including Al [7], Be [8], Ga [9], V and VTi [10]. The important material parameter governing the suitability of the superconductor for observing spin effects is the spin-orbit scattering rate. Qualitatively, the spin-orbit scattering results from distortions in the periodic electric field in the superconductor lattice. This distortion acts as a time-varying magnetic field which flips the electron spins [4]. The scattering rate was estimated as $\tau_{so}^{-1} \sim (e^2Z/\hbar c)^4\tau^{-1}$, where Z is the atomic number of the superconductor and τ is the momentum scattering time [11]. The strong Z dependence of the scattering illustrates one of the reasons why Al is an ideal element for spin-polarized tunneling. In fact, a number of factors taken together made Al the superconductor of choice in this endeavor [4]. For example, crucial to the early success in spin-polarized tunneling was the ease in forming good Al_2O_3 native oxide tunnel barriers. In addition, continuous films as thin as 40 Å can be grown readily with critical fields of several tesla and critical temperature of about 2.5 K, making it relatively easy to reach low reduced temperatures (T/T_c).

Clearly, one would expect interesting effects using spin-polarized electrons to tunnel into the superconductor, due to the ability to separate the current into separate spin up and spin down components. The most obvious source of spin-polarized electrons is a simple ferromagnet. The earliest spin-polarized tunneling experiments were performed by Tedrow and Meservey on Ni because of the unusual features expected in its band structure. For example, at the Fermi energy (E_F) of Ni, the minority spin band is partially filled with a large density of states, while the majority spin band was filled and located primarily below E_F [12]. Thus, one would expect a spin polarization (P) of nearly –100%. In the spin-polarized tunneling experiment of Tedrow and Meservey, the differential conductance for an $Al/Al_2O_3/Ni$ tunnel junction, shown in Figure

1.5, revealed marked asymmetry, reflecting the difference in proportion between spin up and spin down tunneling electrons [13]. In fact, the spin up peaks in Fig. 1.5 are larger than the spin down peaks, indicating a *positive* P. The actual value for P was found to be +11% for Ni in these early results, in contradiction to the large negative value expected from the band structure. The theoretical curve in Figure 1.6 better illustrates the asymmetry due to the spin-polarized electrons of a FM. The P can be calculated from the peaks in conductance at the σ_i's in Fig. 1.6 using the following equation [4]

$$P = \frac{(\sigma_4 - \sigma_2) - (\sigma_1 - \sigma_3)}{(\sigma_4 - \sigma_2) + (\sigma_1 - \sigma_3)}. \qquad (1.8)$$

To get a rigorously correct value for P, a correction for the spin-orbit scattering in the superconductor must also be included. For example, when the spin-orbit scattering is small as expected for Al, the actual polarization is given by $P=P^*(1-1.67b)$, where P^* is the polarization given by Eqn. (1.8) and b is the spin-orbit scattering parameter [4]. For thin Al films, b=0.05, and the value of P is reduced by about 8% from Eqn. (1.8).

A wide variety of transition metal ferromagnets have been studied using this technique, and it is interesting to note that the spin-polarization measured, shown in Table 1.1 [4, 14], is invariably positive, which disagrees with the elementary d-band density of states calculations for a ferromagnet [3]. Theories have been developed subsequently which are able to explain this discrepancy. The main crux of the theories is that the large density of localized d states in these ferromagnets do not contribute to the tunnel current. Instead, the nearly free electrons are primarily responsible for the tunnel current [15]. It was argued that these electrons are

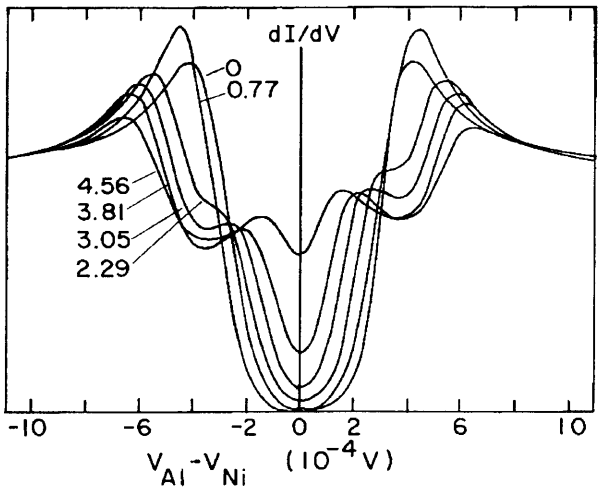

Figure 1.5: Spin-polarized tunneling. Conductance versus voltage for $Al/Al_2O_3/Ni$ junction in several magnetic field values in tesla. From [4]

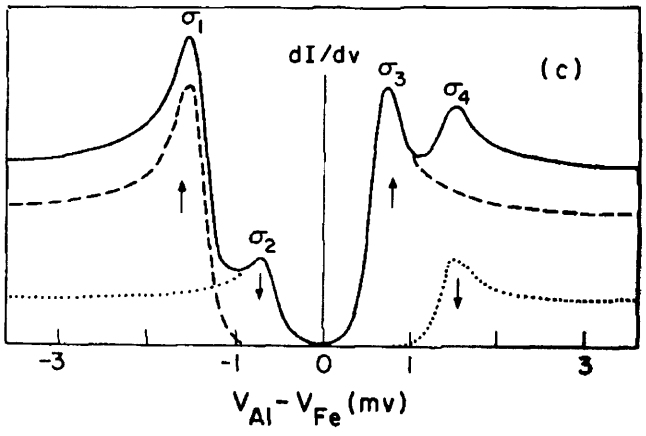

Figure 1.6: Superconductor/ferromagnet tunneling. Normalized conductance for each spin direction (dotted and dashed curves) and total conductance (solid curve). From [4]

Table 1.1: Spin-polarization of ferromagnets measured by spin-polarized tunneling [4, 14].

Ferromagnet	Polarization	Ferromagnet	Polarization
Ni	27%	Fe	41%
$Ni_{86}Fe_{14}$	33%	$Co_{50}Fe_{50}$	51%
$Ni_{78}Fe_{22}$	45%	$Co_{84}Fe_{16}$	49%
$Ni_{74}Fe_{26}$	46%	Co	45%
$Ni_{59}Fe_{41}$	48%	Gd	14%
$Ni_{47}Fe_{53}$	52%	Ho	7.5%
$Ni_{30}Fe_{70}$	51%	Tb	6.5%
$Ni_{25}Fe_{75}$	40%	Er	5.5%
$Ni_{17}Fe_{83}$	49%	Dy	7.0%
$Ni_{12}Fe_{88}$	50%	Tm	2.7%
Ni_4Fe_{96}	45%		

hybridized s-d electrons, and that by virtue of this hybridization, they were positively polarized [16]. Using these assumptions, theoretical values for the polarization were calculated that agreed reasonably well with the tunneling results [17, 18]. Spin-polarized tunneling experiments involving the rare earth ferromagnets presented further evidence that the itinerant electrons were responsible for the tunnel current. In the rare earth ferromagnets, the magnetic moment is carried primarily by the highly localized 4f electrons, which do not contribute to the current. However, the indirect interaction between these 4f electrons and the 6s and 5d conduction electrons results in the latter electrons becoming positively polarized. Measurements on tunnel junctions with a variety of rare earth FMs showed that the spin-polarization of the tunnel current was proportional to the magnetic moment of these conduction electrons [19]. Thus, it has become apparent that spin-polarized tunneling is sensitive to the *conduction* electrons in the electrodes, making it a measurement tool of direct relevance to magnetoelectronics.

Shortly after these early spin polarized experiments, the potential for tunneling between ferromagnets as practical spin dependent transport devices was recognized. However, realization of this has taken over 20 years. Early results were reported in 1975 by Julliere, who observed 14% junction magnetoresistance (JMR) in Fe/Ge/Co tunnel junctions at 4.2 K, where JMR is given by $(R_{max}-R_{min})/R_{max}$, with R_{max} and R_{min} being the maximum and minimum resistances, respectively [20]. In this paper, the often cited Julliere model of ferromagnetic tunneling was presented. This model relates the JMR to the polarizations of the FM electrodes using two key assumptions. The first is spin conservation of the electron spins during tunneling. The second is that the tunnel current for a spin direction is proportional to the density of states of that spin in each ferromagnet. Consequently, minimum resistance is observed when the ferromagnets' magnetizations are aligned parallel to each other, maximum resistance when the magnetizations are antiparallel, as illustrated in Fig. 1.7. The JMR is then given by

$$JMR \equiv \frac{\Delta R}{R_{AP}} = \frac{2P_1P_2}{1+P_1P_2}, \qquad (1.9)$$

where ΔR is the change in resistance between the antiparallel and parallel states, R_{AP} is the resistance of the antiparallel state, and P_1 and P_2 are the spin-polarizations measured in superconductor/ferromagnet tunneling. In actuality, it is unclear whether the JMR observed by Julliere can really be attributed to tunneling, as the effect was present only at low temperatures and persisted only at voltages less than a few millivolts. Later experiments showed that significant spin scattering occurs in amorphous Si and Ge barriers [21], and in fact, the effect seen by Julliere seems to be a zero bias anomaly, whose exact origin is unknown. Despite these questions, the simple model proposed by Julliere has given quite good predictions for the JMR.

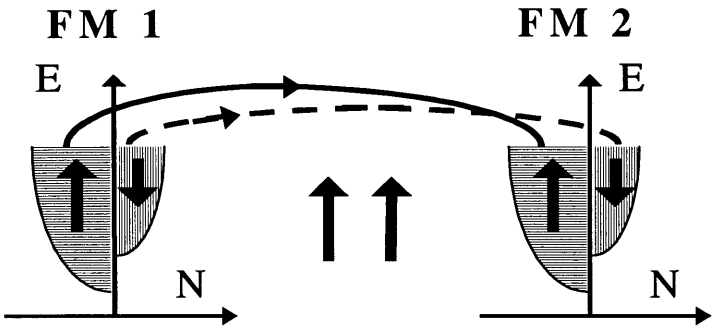

$$I_{\uparrow\uparrow} = N_{\uparrow}^{1} N_{\uparrow}^{2} + N_{\downarrow}^{1} N_{\downarrow}^{2}$$

Parallel **M** – Low R

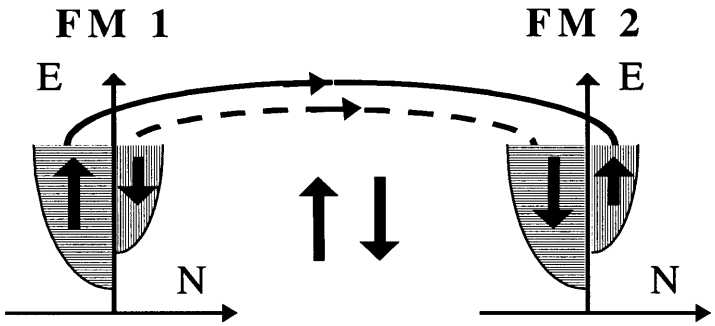

$$I_{\uparrow\downarrow} = N_{\uparrow}^{1} N_{\downarrow}^{2} + N_{\downarrow}^{1} N_{\uparrow}^{2}$$

Antiparallel **M** – High R

Figure 1.7: Ferromagnet/Ferromagnet Tunneling. Spin density of states (DOS) of the ferromagnets for a magnetic tunnel junction in the parallel and antiparallel states. Minimum resistance occurs in the parallel state when electrons tunnel between the large majority bands; maximum resistance occurs in the antiparallel state when the electrons tunnel from majority to minority bands.

Subsequent years saw a number of efforts in fabricating ferromagnet/insulator/ ferromagnetic (FM/I/FM) tunnel junctions, also called magnetic tunnel junctions (MTJs), with limited success. In general, JMR of only a few percent was observed and only at low temperatures [22-25]. One of the major problems encountered was the formation of good tunnel barriers in these junctions. In the superconductor/insulator/ferromagnet tunnel junctions, the process was much simplified since the self-limiting Al_2O_3 was grown from the Al electrode itself, followed by the top FM layer. In contrast, in FM/I/FM junctions, the tunnel barrier must be grown from an ultrathin (~10-20 Å) Al layer deposited on the lower FM. The oxidation process must then ideally oxidize all of the Al without oxidizing the bottom FM. Numerous experiments have shown that spin dependent tunneling is sensitive to the first few monolayers of the electrode at the metal-insulator interface [4, 26, 27]. Therefore, any unoxidized Al will result in tunneling from the normal Al metal rather than the FM, sharply reducing the spin polarization of the tunnel current. Over oxidation of the Al is equally detrimental, since this leads to oxidation of the FM and these oxides typically lead to severe spin scattering. Indeed, some of the early efforts attempted to grow the tunnel barrier from the FM itself, which invariably led to poor spin dependent tunnel junctions [22].

The work of Moodera *et al.* [28] overcame these difficulties by improving the control over the growth of the Al_2O_3 tunnel barrier. This was accomplished by growing the bottom FM electrode and the Al layer by evaporation onto liquid N_2 cooled glass substrates. The low substrate temperature inhibited surface mobility of the deposited atoms, thus reducing island formation in these layers. As a result a smooth FM/I interface was formed. The subsequent O_2 plasma oxidation resulted in very uniform Al_2O_3 tunnel barriers with minimal spin scattering or

other undesirable current paths. The resulting JMR for a tunnel junction prepared in this manner is shown in Fig 1.8. Since this work, numerous studies have been performed on FM/I/FM tunnel junctions, including many geared toward producing useful device applications. A number of fundamental properties of these magnetic tunnel junctions (MTJs) have become evident, and theories have been proposed to explain some of this behavior.

One common observation of MTJ's is the temperature dependence of the tunnel junction resistance (R_J) and JMR. Typically, R_J and JMR both increase with decreasing temperature, with the amount of the increase in each reflecting the quality of the tunnel junction; superior tunnel junctions show smaller increases in both R_J and JMR. High quality $Co/Al_2O_3/Ni_{80}Fe_{20}$ tunnel junctions show R_J increasing by 15-20% upon cooling from 295 K to 4.2 K, while JMR increases from 20% at 295 K to 27% at 4.2 K [29]. In contrast, poor MTJs can show R_J increases of several orders of magnitude, and JMR increases from negligible at 295 K to over 20% at low temperatures.

Shang *et al.* [30] performed careful studies of the temperature dependence of nearly ideal MTJs and developed a model which helped explain some of the mechanisms involved. One of the significant questions was the increase of R_J in even the best junctions at low temperatures, since elastic tunneling theory predicts an increase of only a few percent between 295 K and 0 K. Furthermore, the increase of JMR at low temperatures indicates a change in spin polarization of the FM. These behavior were explained by modeling the tunnel current as consisting of two parts, a spin dependent elastic component described by Julliere's model and a spin independent part resulting from inelastic tunneling processes. The polarization of the FMs responsible for the spin dependent part was found to follow the relation $P = P_0(1-\alpha T^{3/2})$, which results from

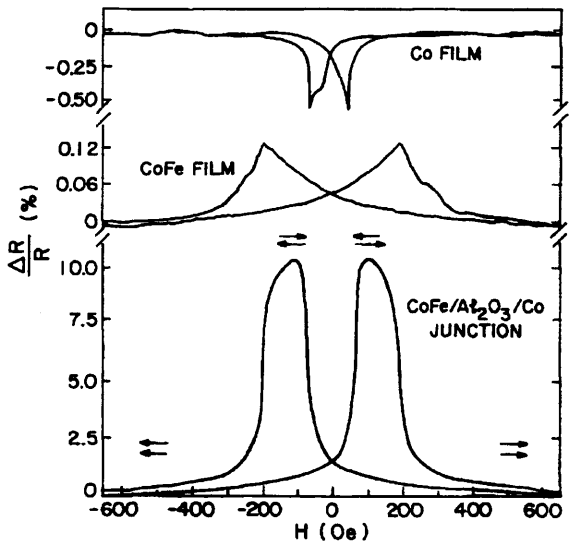

Figure 1.8: Magnetoresistance in $CoFe/Al_2O_3/Co$ junction at 295 K. Also shown is the variation in the CoFe and Co resistance. Arrows indicate the direction of magnetization in the two films. After [28].

thermally excited spin waves that reduces the magnetization at the FM surface. This relation has been found to hold for bulk samples, ultrathin films and surface magnetization well below the Curie temperature [31-33]. The spin independent conductance (G_{SI}) followed a power law dependence, $G \sim T^{\gamma}$, with γ approximately 4/3, which is in agreement with a two-step hopping model whereby electrons can hop to states within the Al_2O_3 tunnel barrier. Other possible conduction mechanisms are possible as well, including conduction through pinholes, oxides of the FM electrode, and magnon or phonon assisted tunneling in which these excitations are emitted or absorbed by the electron while tunneling [29, 30].

An additional feature of MTJs is the bias voltage dependence of the JMR. Elastic tunneling theory predicts a parabolic dependence of the JMR on the applied voltage. However, the JMR invariably falls much faster with voltage, exhibiting a pronounced cusp at zero bias. Bratkovsky [34] developed a theory which seems to explain this behavior by including inelastic magnon and phonon assisted tunneling processes together with elastic tunneling. The comparison of the theory to experimental data is shown in Figure 1.9 [34]. Sharp features are expected in the current vs. voltage (I-V) curves in the 30-100 mV range, precisely where the cusp-like features appear in both the JMR vs. V and the conductance (G) vs. V. Experimentally, Moodera *et al.* [29] observed a sharp peak in the d^2I/dV^2 inelastic tunneling spectra of MTJs at about 17 mV and a second smaller peak at 100 mV, which were interpreted as resulting from magnon excitations in the FM electrodes. These features were noticeably absent in tunnel junctions with normal metal electrodes, as expected. The sharper reduction in JMR with voltage is then explained; magnons, being spin excitations, are expected to result in spin flip of the tunneling electrons and would therefore result in a steeper decrease in JMR compared to elastic tunneling.

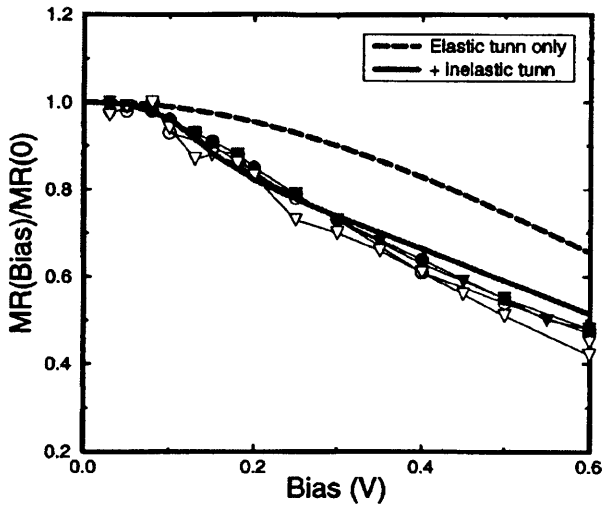

Figure 1.9: Bias voltage dependence of magnetoresistance in CoFe/ Al_2O_3/NiFe tunnel junctions. Fits for elastic tunneling with and without inelastic (magnon and phonon) processes shown, along with experimental data points.

A final matter still open for debate is the role of the density of states (DOS) of the electrodes on both the tunnel conductance and magnetoresistance of MTJs. The model of metal/insulator /metal tunneling presented above predicts that the DOS of the minority and majority spins should play a role in the voltage dependence of the transport properties in MTJs. However, extracting DOS features from transport data, *e.g.*, I-V, G-V or JMR vs. V, has proven difficult, since these all can show effects from the aforementioned elastic and inelastic tunneling processes, which obscure the DOS of the electrodes. Recent measurements in MTJs with Ni as one or both electrodes show a pronounced dip in the G-V curve [35], which may reflect the peak in the minority spin band in Ni 100 mV from the Fermi energy. In fact, the dip can be large enough that the minimum conductance is well away from zero voltage, although whether this reflects the Ni DOS is not entirely clear. Nevertheless, as is seen in metal/insulator/ superconductor junctions, gross features such as energy gaps are easily resolved in tunneling spectroscopy.

Chapter 2 Half-Metallic Ferromagnetism

It is clear from Julliere's model, Eqn. (1.9), that the JMR of a MTJ is strongly dependent on the spin-polarization of the two FM layers. It is therefore of great interest from an application point of view to find materials with higher spin-polarization than conventional FMs, which are limited to about P=50% or less. In 1982, such materials were discovered, at least in theory, when band structure calculations by de Groot *et al.* [1] on the Heusler alloys NiMnSb and PtMnSb predicted 100% spin-polarized conduction electrons in these materials. The NiMnSb band structure, shown in Fig. 2.1, exhibits a band gap at E_F in the minority spin band, in contrast to the majority spin band which is metallic. This phenomenon was termed half-metallic ferromagnetism (HMF), as only one spin direction showed metallic behavior. Subsequently, a number of other half-metallic systems have been identified as well, including CrO_2 [36], Fe_3O_4, and $La_{0.67}Sr_{0.33}MnO_3$ (LSMO) [37].

There are a number of important implications for spin dependent tunneling using half-metallic electrodes. The most obvious is of course the 100% spin polarization, which leads to a large junction magnetoresistance in magnetic tunnel junctions. However, there are other important advantages of using HMFs. As mentioned earlier, magnon excitations are expected to be suppressed in the HMF electrodes. As a result, magnon-assisted tunneling processes should be absent in tunnel junctions with HMF electrodes, which leads to a weaker drop in the JMR with bias voltage for HMF tunnel junctions in comparison to normal MTJs. Furthermore, due to the energy gap in the minority spin band, the JMR should be basically flat until the applied voltage goes beyond the gap [38]. As discussed earlier, although observing band structure features of ferromagnets in planar tunnel junctions has not been conclusively shown, there

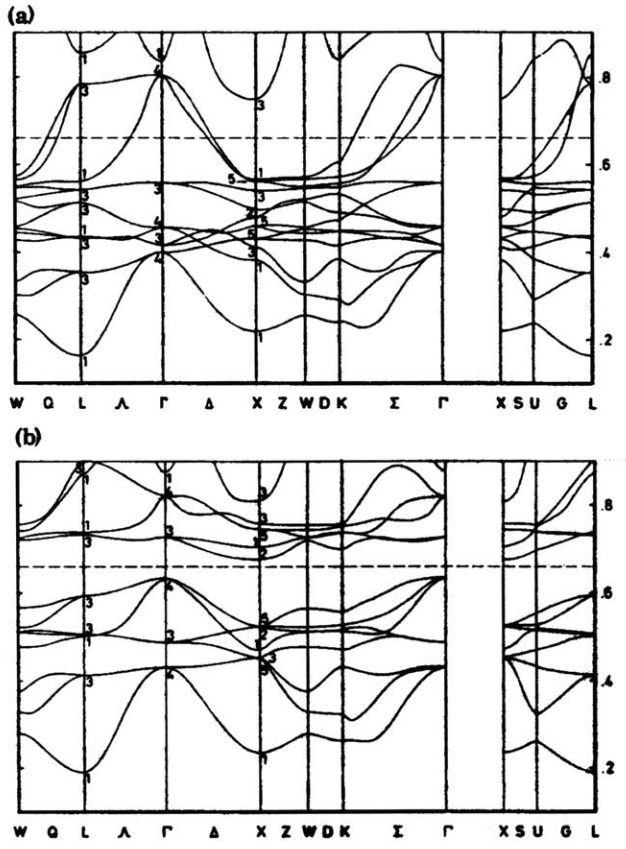

Figure 2.1: Band structure of NiMnSb for (a) the majority-spin direction and (b) the minority-spin direction. Energy in Ry. From [1].

should not be any difficulty in observing a feature as pronounced as an energy gap. This should also hold true for the spin sensitive gap expected for HMFs.

Experimental confirmation for half-metallic ferromagnetism has been rather sparse, however. In fact, the only material in which 100% spin-polarized electrons has been directly observed is in the colossal magnetoresistive (CMR) material, LSMO. Spin-polarized photoemission on this material showed the absence of spin down electrons at the Fermi level (E_F), and magnetic tunnel junctions with LSMO showed large magnetoresistance, indicating a large spin polarization [37, 39]. Both of these techniques are extremely surface sensitive, which might make LSMO promising for device applications in which surfaces and interfaces play a major role. However, the enhanced polarization persisted only at low temperatures, and the Curie temperature for LSMO is near room temperature, which limits its possibilities for useful technology. Similar photoemission experiments on CrO_2 show an energy gap in the minority spin band, but 2 eV below E_F [40] Furthermore, in these latter results, the spectral weight at E_F almost vanishes, suggesting insulating behavior at the surface.

In the case of NiMnSb, some indirect evidence indicates that it is indeed half-metallic. For example, transport measurements by Moodera and Mootoo [41] on NiMnSb thin films show that the resistivity shows linear dependence on temperature around 1-15 K, which is in contrast to normal ferromagnets which show T^2 dependence arising from magnon spin flip scattering. These processes are forbidden in half-metallic ferromagnets due to the absence of minority spin states. Secondly, examination of the Fermi surface of bulk NiMnSb performed by Hanssen *et al.* [42] using spin-polarized positron annihilation confirms the presence of a minority spin bandgap. A final piece of evidence is that the integer magnetic moment of NiMnSb, which is 4 μ_B per

formula unit. It has been argued that a necessary condition for half-metallicity is an integer number of μ_B per formula unit. This is because the minority spin band must be full, *i.e.* have an integer number of electrons. Then the majority electrons, as well as the difference between the two, must also be integer.

Unfortunately, efforts to directly measure the spin polarization of NiMnSb have been less successful. In spin-polarized photoemission experiments, Bona *et al.* [43] measured a P of only 50% for electrons photoemitted from single crystal NiMnSb. Measurements on NiMnSb-based giant magnetoresistive (GMR) multilayers indicated an even more modest value of P, showing GMR ratios of only a few percent at low temperatures [44]. Furthermore, attempts by Kabani [45] to use the spin-polarized tunneling technique in NiMnSb/Al_2O_3/Al tunnel junctions were unsuccessful in measuring the P of NiMnSb. A major problem encountered was the absence of spin-splitting in the Al superconductor, which was attributed to severe orbital depairing effects in the superconductor caused by the roughness of the NiMnSb films. This made measuring the polarization impossible. In similar experiments, efforts by the author to fabricate magnetic tunnel junctions with polycrystalline NiMnSb thin films indicated a polarization of only about 10% (Appendix A) [46].

The focus of this body of work is the Heusler alloy NiMnSb, and some fundamental characteristics of this material are worth noting. Structurally, NiMnSb exhibits the $C1_b$ crystal structure with unit cell of 5.903 Å, as shown in Fig. 2.2, which consists of three interpenetrating fcc lattices, each formed by of one of the component elements; Ni at {0,0,0} sites; Mn at {¼, ¼, ¼} and Sb at {¾, ¾, ¾}. A fourth site in this lattice at {½, ½, ½} is empty. This site occupancy of the atoms in the unit cell is critical to the half-metallic properties. Indeed, after the

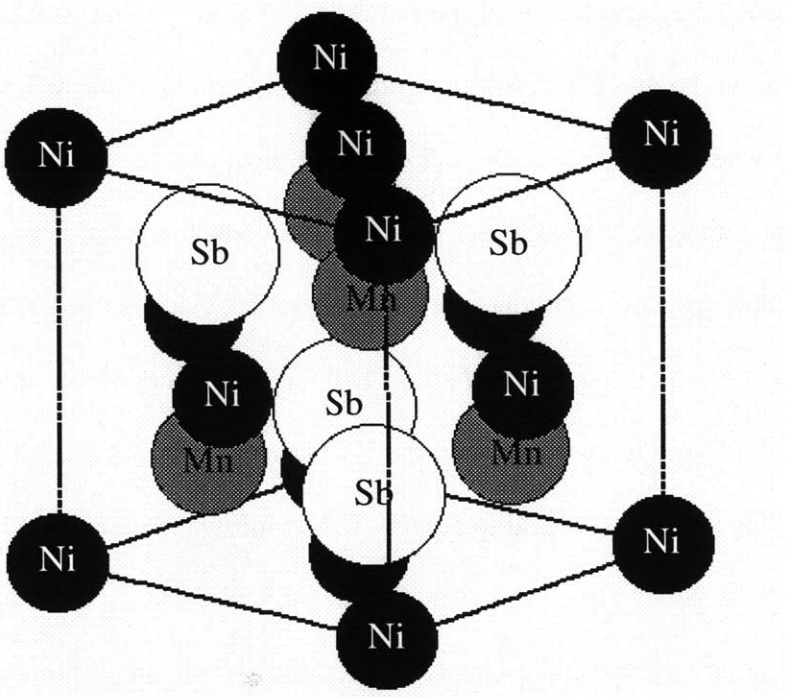

Figure 2:2 $C1_b$ crystal structure of NiMnSb

calculations of de Groot, concern was raised about the correct site occupancy, since earlier measurements using neutron and x-ray diffraction on this compound indicated that the Mn sits at the {½, ½, ½} site [47]. However, later measurements confirmed that the Mn did indeed lie at {¼ , ¼, ¼} sites 48].

De Groot explained the details of the bonding that lead to HMF in NiMnSb [1]. It is readily evident that the Ni and Sb atoms are structurally identical to the well known zincblende structure, as in the semiconductors GaAs and GaSb. It turns out that the Ni *d* electrons play little role in the bonding, and the Sb *p*-states are primarily covalently bonded in NiMnSb, as in the semiconductors. The metallic-semiconductor spin asymmetry arises due to the interaction between the strongly exchange split Mn *d*-states and the Sb *p*-states. Note that the loss of inversion symmetry around the Mn between the $C1_b$ structure and the $L2_1$ structure, which has the (½, ½, ½) sites occupied, is critical to HMF. This resulting loss of conjugation or spin flip symmetry in $C1_b$ NiMnSb changes the interaction between the Mn t_{2g} states and the Sb *p*-states, causing mutual repulsion between these states. Then the Mn majority spin up states, which lie below E_F due to the Mn exchange splitting, push the Sb spin up *p*-states above E_F. These connect with lower states, resulting in metallic behavior for the majority spin band. In contrast, the Mn minority spin down states, which lie above E_F, push the Sb spin down *p*-states below E_F, thus opening up the energy gap in the minority spin band.

In terms of its magnetic properties, the bulk saturation magnetic moment per formula unit of NiMnSb was found to be 4 μ_B, as stated earlier, while the Curie temperature is relatively high, 730 K [49]. This makes it potentially promising for practical spin transport devices. The magnetic moment is almost entirely carried by the Mn atoms from the neutron diffraction

measurements [47, 48]. Subsequent measurements using magnetic circular dichroism, confirmed this, but also found small induced moments on the Ni and Sb sites, aligned parallel and antiparallel to the Mn moment, respectively [50].

Preparation of NiMnSb samples typically require high temperatures in order to crystallize the desired $C1_b$ structure. For instance, bulk samples have been made by melting the componentelements in a sealed tube, followed by an extended period of annealing at high temperatures[47, 51]. Thin film samples were grown by Kabani *et al.* [45, 52], who used co-evaporation of the three component elements onto heated glass substrates to obtain $C1_b$ NiMnSb. These latter experiments also showed that the magnetic properties in NiMnSb were strongly tied to its crystal structure. This correlation became evident when it was observed that NiMnSb films with poor $C1_b$ compound formation, as measured by x-ray diffraction, also had significantly reduced magnetic moments. In fact, the full magnetic moment of 4 μ_B was found in films with good $C1_b$ NiMnSb formation, which required substrate temperatures of 400°C or higher. Subsequently, NiMnSb films were successfully grown by sputtering, both from a single target [53], and from three separate targets [54].

The primary difficulty in incorporating NiMnSb into spin dependent tunnel junctions is the high T required to form the desired $C1_b$ crystal structure [45, 53, 54]. Magnetic tunnel junctions typically do not survive temperatures greater than 300°C, undergoing irreversible degradation of the tunneling properties. As a result, the NiMnSb must be grown as the first electrode before growth of the Al_2O_3 tunnel barrier. At these elevated temperatures, one must be concerned with degradation of the NiMnSb surface, for example surface segregation of one of the component elements or surface oxidation. As in the earlier Kabani work, surface roughness

also presents a major problem, since it is difficult to grow a uniform 10-20 Å tunnel barrier on a rough bottom electrode. The challenge then is to grow smooth layers of NiMnSb with good $C1_b$ compound formation and clean surfaces, and then grow a good Al_2O_3 tunnel barrier on top.

Chapter 3: NiMnSb Growth and Characterization

In order to address the difficulties in fabricating NiMnSb spin dependent tunnel junctions, it is necessary to first be able to grow good $C1_b$ NiMnSb films. This chapter details the optimum growth conditions for epitaxial NiMnSb films which can be incorporated into such multilayer structures. The surface composition was characterized *in situ* by Auger electron spectroscopy, to insure that the NiMnSb surface was free of contamination. In addition, the $C1_b$ compound formation in the films was insured by x-ray diffraction and magnetization measurements. Furthermore, surface morphology was studied by atomic force microscopy, since the surface smoothness is crucial to the formation of a good, pin-hole free insulation barrier on the NiMnSb.

3.1 Molecular Beam Epitaxy System

NiMnSb samples were grown in a custom built molecular beam epitaxy (MBE) system shown in Figure 3.1, specially designed for this project. This system offers a number of key advantages over prior efforts in fabricating NiMnSb multilayers. For instance, the system has a base pressure of 10^{-10} torr, allowing the films to be grown in extremely clean conditions. It also offers improved control over the composition, as well as analytical tools (Auger electron spectroscopy and x-ray photoelectron spectroscopy) to characterize the surface composition of the critical layers. In addition, a shadow mask system is installed which allows the multilayer structures to be grown entirely *in situ*. These factors allow for improved interfaces, which are crucial for the performance of the trilayer tunnel junctions for this study.

The main chamber of the MBE system, where all film deposition takes place, is pumped

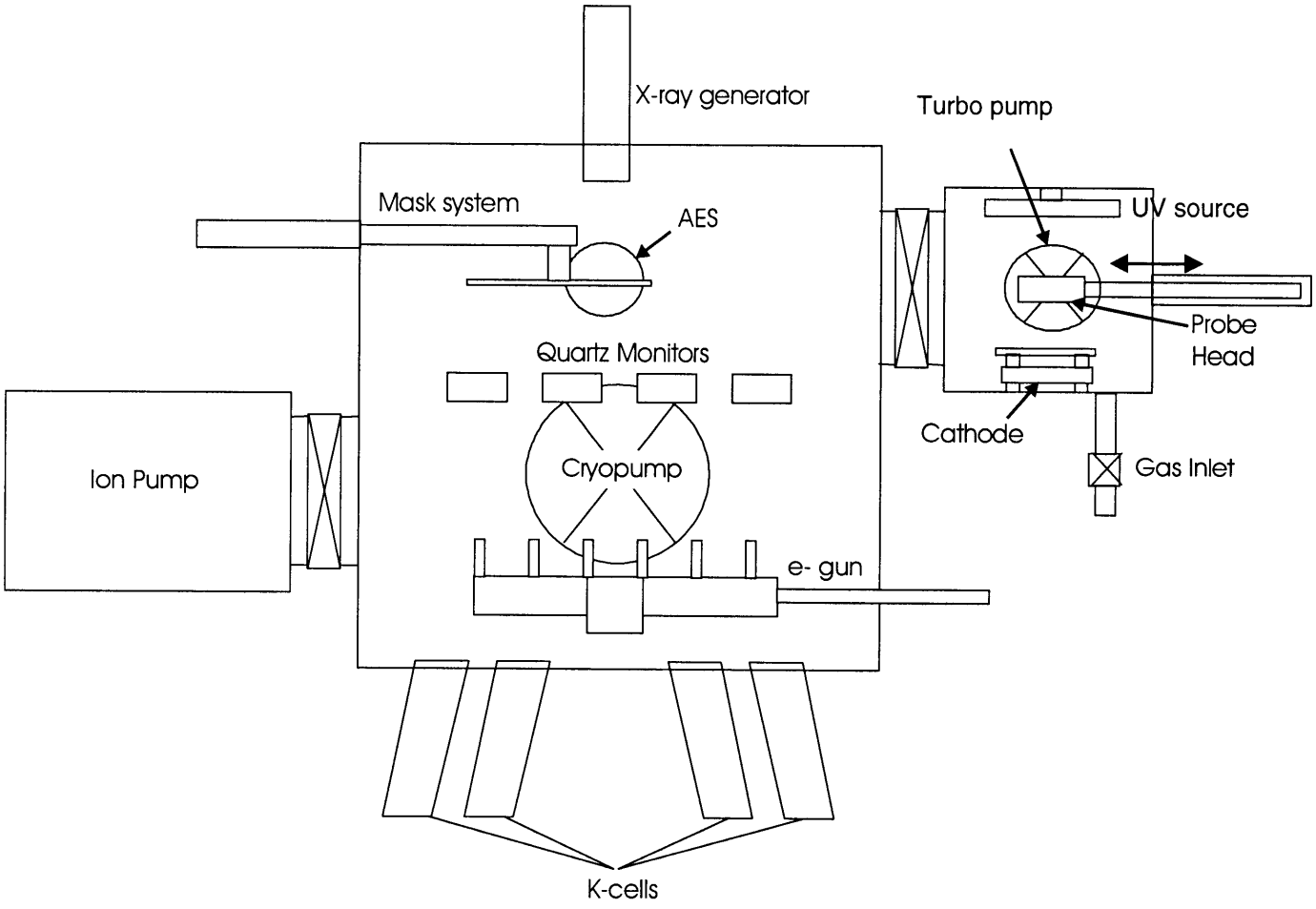

Figure 3.1: The Molecular Beam Epitaxy System

by an ion pump, cryopump, titanium sublimation pump and a liquid nitrogen cooled cryoshroud. Six deposition sources are available, four Knudsen effusion cells (K cells) and two electron guns. Each electron gun has five different hearths mounted on a linear feedthrough, giving a total of fourteen different materials that can be deposited. Film deposition was monitored using five separate quartz crystal microbalances (QCM), one for each K cell and one that can be positioned at the substrate position for calibration of the QCM tooling factors. Two of the microbalances are shared with the electron guns, allowing up to four sources to be deposited simultaneously, in the appropriate combinations (e.g. four K cells or two K cells and two electron guns, etc.).

The system has an additional load-lock chamber pumped with a turbo pump and rotary pump, by which samples are changed and where the oxidation for the Al_2O_3 tunnel barriers is performed. The load lock has a gas inlet system which allows a variety of process gases to be introduced in a controlled manner. A sorption pump is included in this system which is used to evacuate the gas lines, ensuring the purity of the input gases. A key component of the load lock is the glow discharge unit, shown in Fig. 3.2. The unit consists of a donut-shaped Al cathode which generates a plasma upon application of a negative voltage of 500-1500 V. A floating Al disc with a hole in the center above the cathode shields the substrate from a direct pathway to the cathode. This serves to lessen the energy of the ions that may bombard the surface of the substrates. A low-pressure mercury ultraviolet (UV) lamp is also mounted in the load-lock, which was used for UV-assisted oxidation for the Al_2O_3 tunnel barriers.

Substrates are held by two 2.5 cm substrate holders which were clamped to each side of a linear, motor-driven probe. The probe allowed the substrates to be transferred from the load-lock

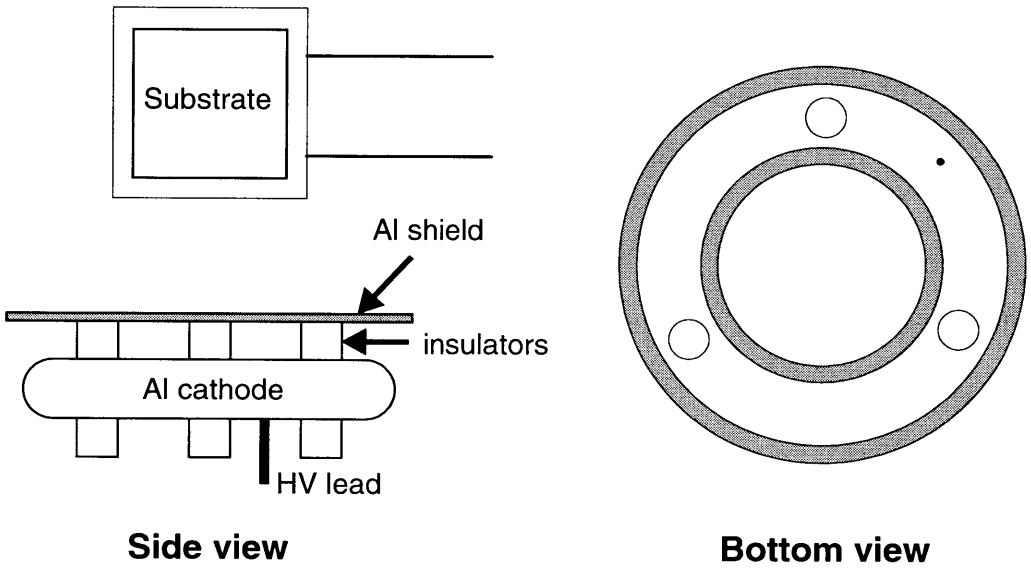

Figure 3.2: Glow discharge unit.

to the main chamber and back. Substrate temperature (T_s) could be adjusted anywhere from 100 K to 773 K using liquid N_2 cooling lines on the probe or a wound Kanthal (FeCrAl alloy) wire heater within the probe head. T_s was measured by chromel-alumel thermocouples fixed to the clamps holding the substrate holders.

3.2 NiMnSb Growth

To improve on prior spin dependent tunneling experiments on polycrystalline NiMnSb [45, 46], epitaxial films of NiMnSb are highly desirable. Epitaxial (001) films of the Heusler alloy PtMnSb, which has the identical $C1_b$ crystal structure, have already been successfully grown using seed layers of W on MgO (001) substrates [55]. The body-centered cubic (bcc) W layer (unit cell, a=3.165 Å) grows epitaxially in the (001) orientation on the face-centered cubic (fcc) MgO (a=4.216 Å). The in-plane orientation of the W unit cell is, however, rotated by 45° from that of the MgO, *i.e.*, the ratio of the unit cells is approximately $1:\sqrt{2}$. Then the roughly 2:1 correspondence of the PtMnSb (a=6.20 Å) with the W layer results in cube-on-cube growth of the PtMnSb. In fact, a wide variety of bcc transition metals can be grown epitaxially on MgO with this 45° rotation [56], allowing for different seed layer materials to be used to optimize the Heusler alloy growth. One promising seed layer material for NiMnSb is vanadium, as its lattice parameter is 3.030 Å, giving a lattice mismatch of only 0.023 between V and NiMnSb (a=5.920 Å). In addition, epitaxial V films have been grown at temperatures as low as 50 °C [57], suggesting the possibility of reduced growth temperatures, which would be advantageous in the fabrication of spin dependent tunnel junctions. Furthermore, coherent growth of V on MgO(001) has been observed for V thicknesses less than 50 Å [58].

Polished single crystal MgO substrates were prepared for deposition by degassing them in the load lock chamber at 450 °C for several hours. The substrate temperature was then brought to the desired growth temperature before being transferred from the load lock to the main chamber.

The V seed layer was deposited at a rate of 7 Å per minute from a 99.999% pure V source using one of the electron guns. Two different seed layer thicknesses (d_V) were tried, 30 Å and 100 Å. Subsequently, NiMnSb films were grown at about 8 Å per minute on the seed layers by co-evaporation of the three component elements; Ni (99.995% purity) from one electron gun, Mn (99.99%) and Sb (99.999%) from separate K cells. Control over the instantaneous rate of each source was maintained within approximately 10% of the desired rate, while the composition of the entire film was within about 1% of the desired stoichiometric NiMnSb compound, representing the uncertainty in the calibration of the quartz microbalances. Care was taken to insure that the deposition rate of the sources was maintained equal for the top 20-30 Å of the film, since these are the crucial layers for spin dependent tunneling. In some instances additional layers of NiMnSb were deposited until a satisfactory surface composition is achieved. After the *in situ* Auger electron spectroscopy discussed in the following section, the films were cooled to room temperature and capped with 30 Å Al to protect the films from oxidation.

3.3 Auger Electron Spectroscopy

Since the surface plays a crucial role in spin-polarized tunneling, it is important to check the surface layers for contamination as well as for the composition of the NiMnSb. The behavior of Sb is of particular concern since it has a low surface energy, as well as a relatively low

evaporation temperature. Surface segregation or desorption of Sb is thus possible. Consequently, the films were characterized within minutes of the film deposition, *in situ* by Auger electron spectroscopy (AES), which is sensitive to the top ~20-30 Å of the films. A Physical Elecronics PHI 548 AES/XPS system was used with an incident beam of 3 keV electrons at a current less than 0.1 mA to minimize contamination of the sample from the electron source. The Auger spectra for V/NiMnSb films grown on MgO (001) substrates at T_S = 400 to 100°C are shown in Figs. 3.3 to 3.6.

All of the Auger spectra show the expected Ni and Mn LMM peaks and the Sb MNN peaks, indicated by the brackets in Figs. 3.3 to 3.6. However, the spectra of the 400°C samples in Fig. 3.3 show some surprising features in addition. First, carbon and oxygen KLL peaks are evident suggesting some contamination at the surface of the film. Furthermore, substantial vanadium LMM peaks are present. In contrast to these films, the Auger spectra on the films grown at 100-300°C show clean NiMnSb surfaces, free of C, O and V. Initially, it was thought that V was diffusing to the surface at the elevated temperatures. Since V acts as a strong getterer of residual gases, it could then be rapidly contaminated. However, from the standpoint of surface energy, this did not seem reasonable since V has a moderately high surface energy. In comparison, Sb in particular has a much lower surface energy, and can act as a surfactant in epitaxial film growth [59]. The source of the C and O, as well as the V, became clear after observing the surface morphology of the 400°C NiMnSb films. These showed deep trenches extending nearly to the substrate, as will be discussed in the section on atomic force microscope examinations.

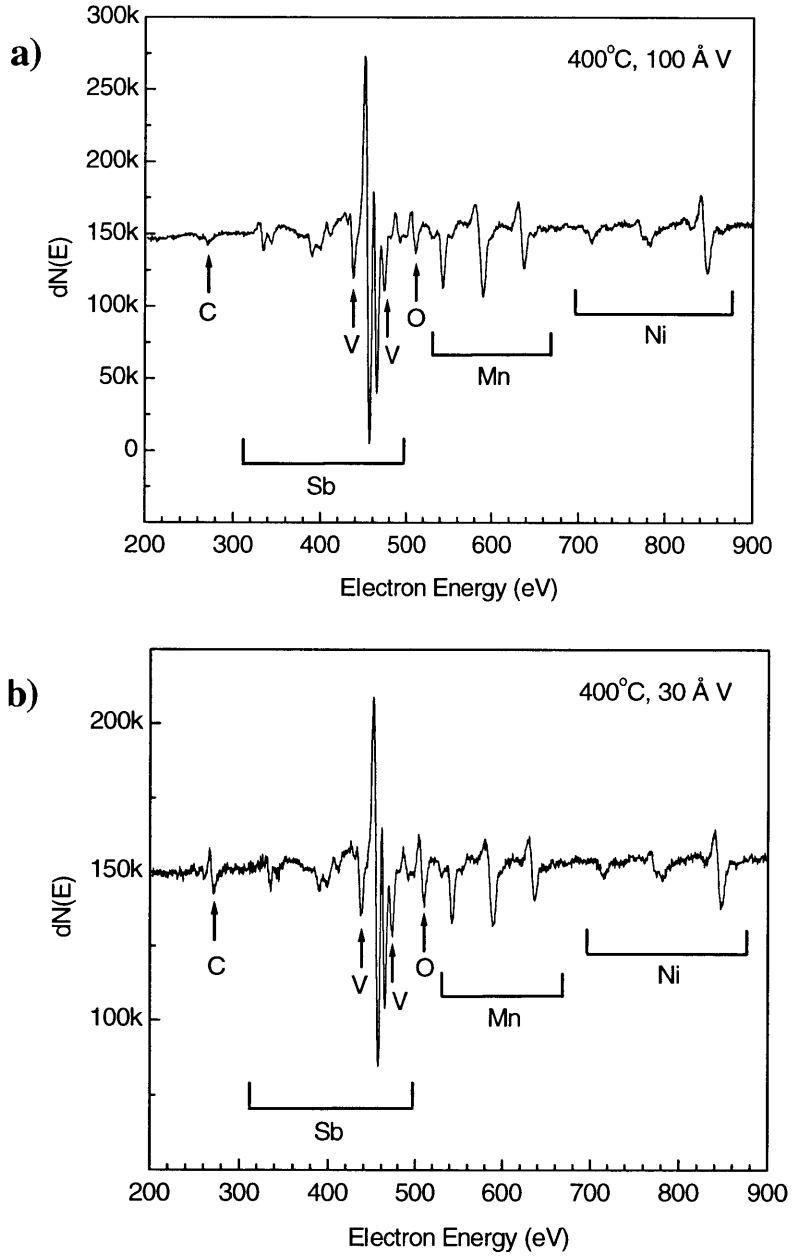

Figure 3.3: Auger electron spectra for NiMnSb films grown at 400°C. a) 100 Å V seed layer b) 30 Å V seed layer. Films show C and O contamination, as well as V. Later AFM studies showed that these reflected the formation of deep trenches in the film extending to the substrate.

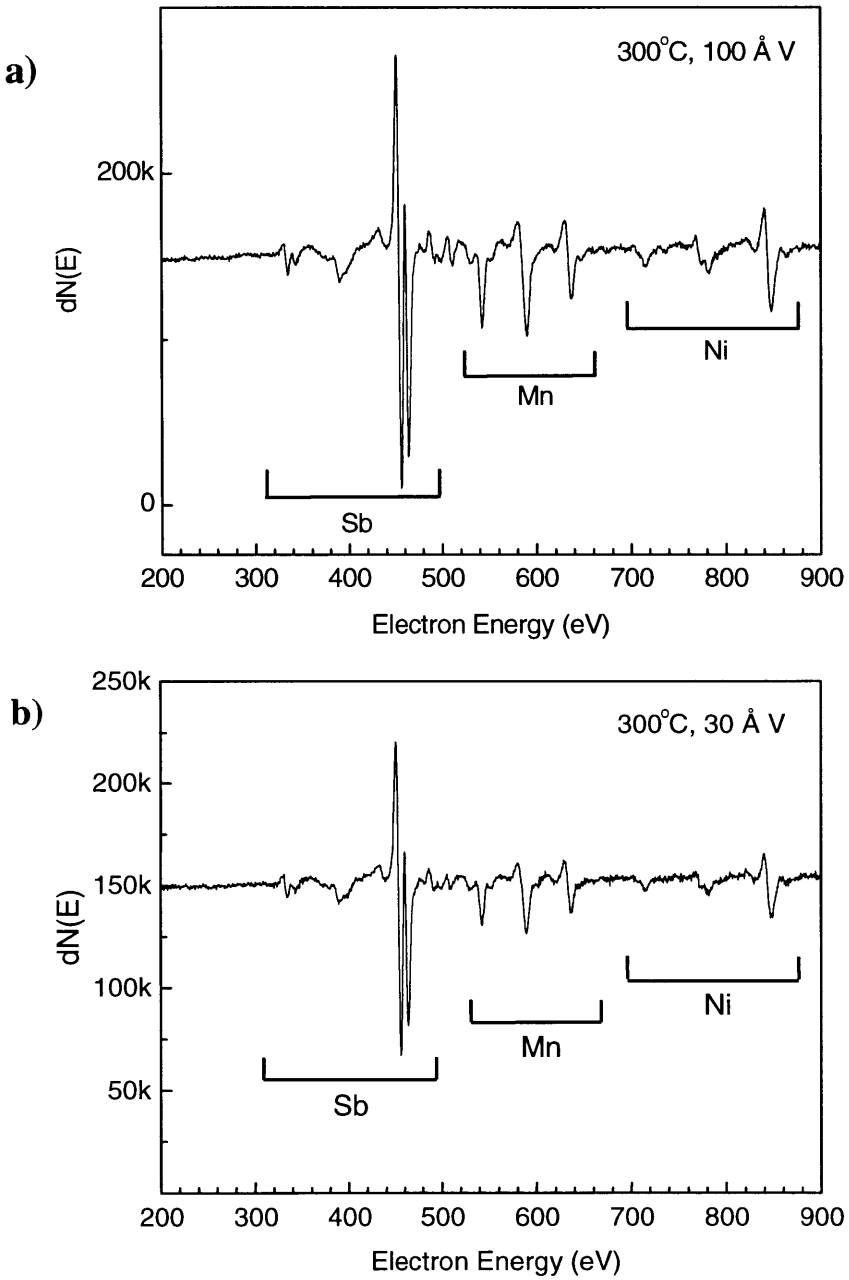

Figure 3.4: Auger electron spectra for NiMnSb films grown at 300°C. a) 100 Å V seed layer b) 30 Å V seed layer. Films are both free of contamination.

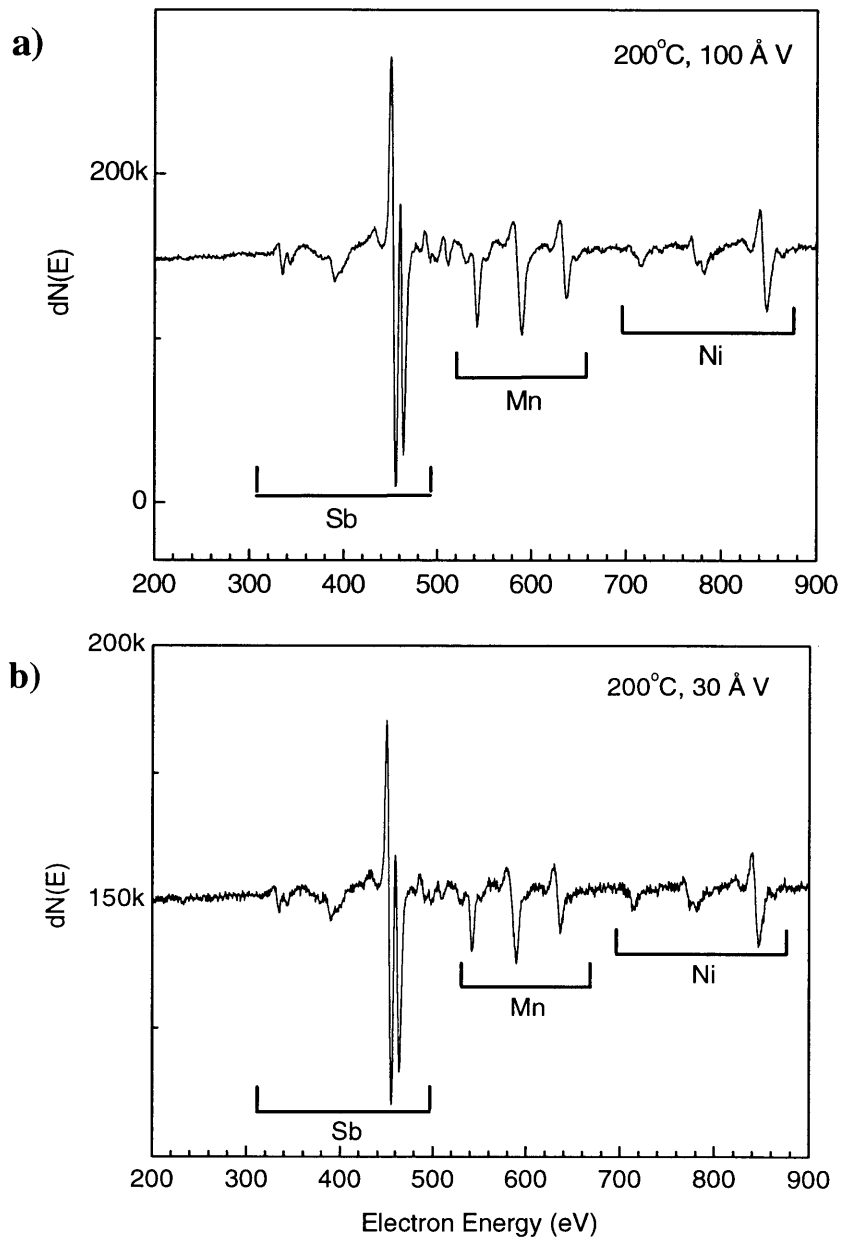

Figure 3.5: Auger electron spectra for NiMnSb films grown at 200°C. a) 100 Å V seed layer b) 30 Å V seed layer. Films are both free of contamination.

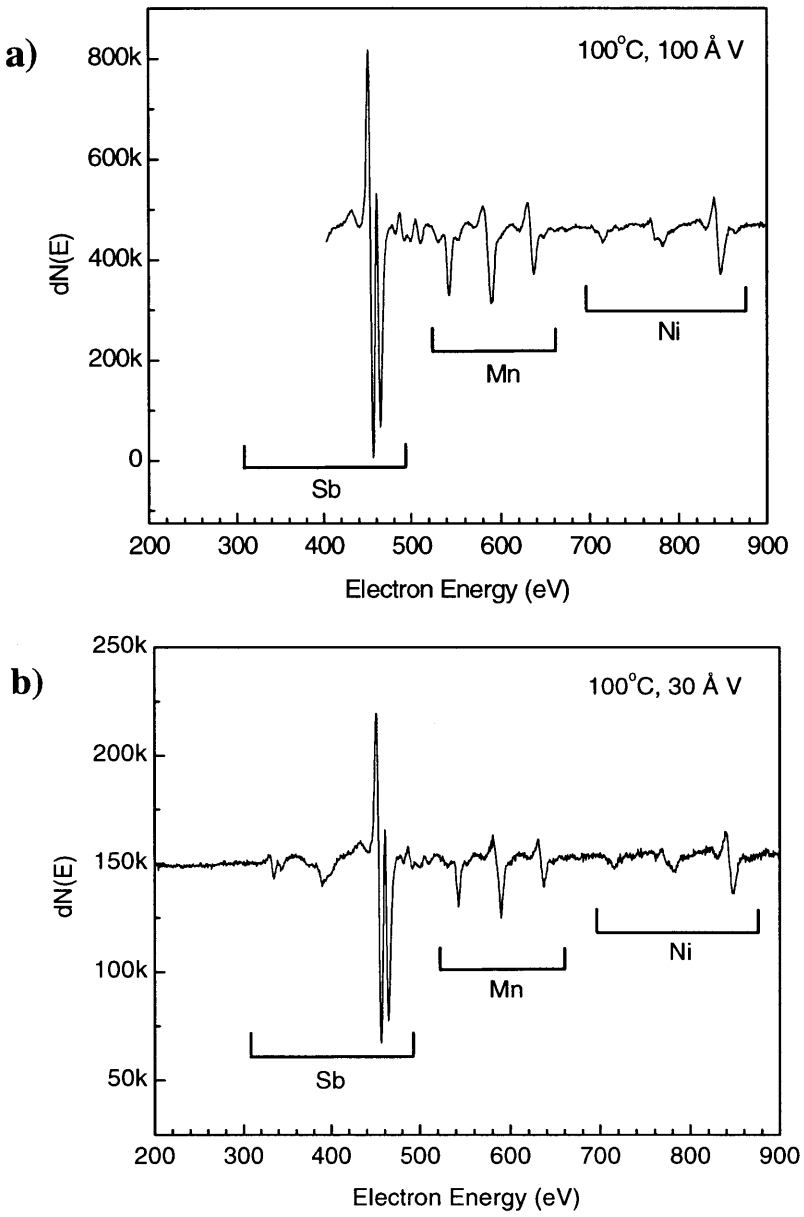

Figure 3.6: Auger electron spectra for NiMnSb films grown at 100°C. a) 100 Å V seed layer b) 30 Å V seed layer. Lower curve is free of contamination. Data below 400 eV not available for a).

We now consider chemical composition of the component elements in the NiMnSb films. It is important to note that it is in fact difficult to get accurate quantitative information on the absolute composition of a film via AES. Nevertheless, it is still possible to compare the composition of the films grown at different temperatures to check, for example, for surface segregation or desorption of any of the elements at high temperatures. To this end, relative intensities of the dominant peak of each element was compared at different temperatures. Fig. 3.7 shows the variation of the intensities of the Mn and Ni Auger peaks scaled to the Sb peak. The data was averaged over a few scans for each point, and error bars were estimated from their standard deviation. An additional film was grown on a Si (001) wafer cooled to 110 K for comparison. At this low temperature, mobility of the surface adatoms will be greatly reduced, which should suppress the Sb surface segregation. There is some scatter in the data, reflecting the small instabilities of the instantaneous fluxes from the sources, but the data shows no systematic variation of the composition of the films with temperature.

In conclusion, these AES experiments show that NiMnSb films free of surface contamination can be grown at 300°C or less. Furthermore, the surface segregation or desorption of Sb does not appear to occur over the range of T_S used, as the composition of the Ni, Mn, and Sb does not appear to change with T_S.

3.4 X-ray diffraction

Structural information on the films is also necessary, since the half-metallic properties are predicted only for $C1_b$ NiMnSb. X-ray diffraction (XRD) of the NiMnSb films was performed to check whether the films exhibited the desired crystal structure. Measurements were taken with a

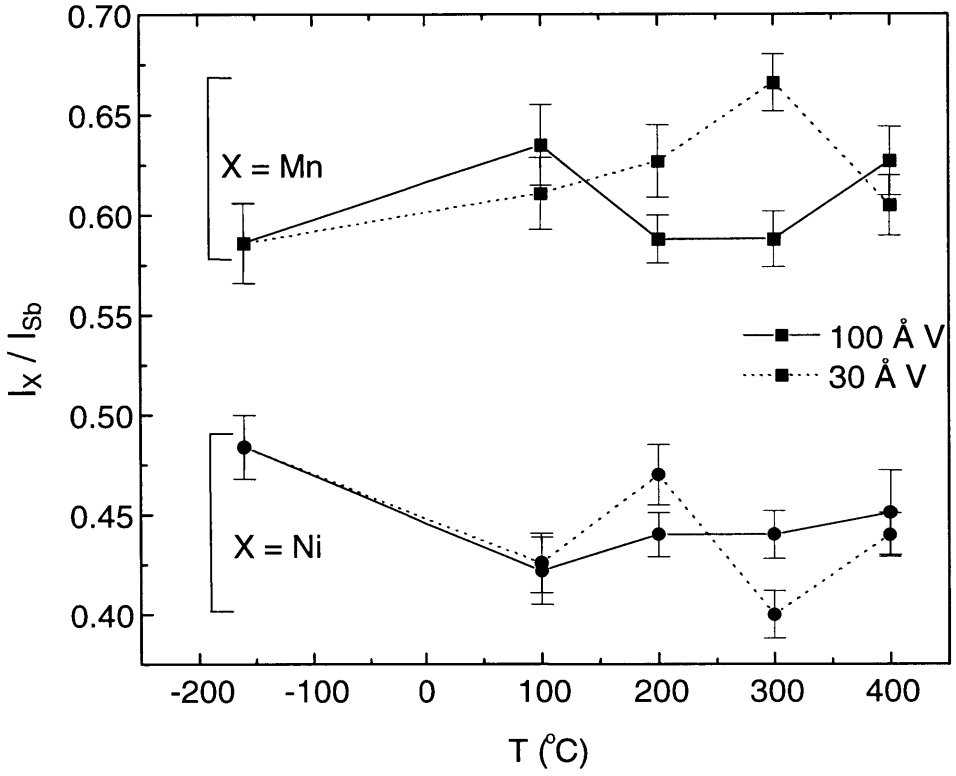

Figure 3.7: Auger peak intensities as a function of substrate temperature. The Ni and Mn LMM Auger peaks are scaled relative to the Sb MNN peak. Upper curve shows the Mn data; lower curve the Ni data.

Rigaku RU300 diffractometer for θ-2θ scans, which characterizes the structure normal to the film plane. Cu $K\alpha_1$ radiation (λ=1.54059 Å) from a rotating anode x-ray generator was used at 60 kV, 300 mA for all θ-2θ scans. The XRD data for films grown at substrate temperatures from 100 to 400 °C are shown in Figs. 3.8 to 3.11. Note that the shape as well as the intensity of the MgO (002) peaks are not accurate, as the detector is saturated by the enormous intensity of the peaks. The XRD patterns for the films grown between 200°C and 400°C are largely indistinguishable from each other, with all of them showing (001) growth of the $C1_b$ NiMnSb compound. In contrast, the films grown at 100 °C show NiMnSb (002) and (004) peaks that are two orders of magnitude lower intensity, indicating incomplete formation of the $C1_b$ structure. Thus, as in prior work [45, 46, 52], T_s plays a crucial role in the growth of NiMnSb. However, the seed layer thickness does not seem to influence the crystallization of the $C1_b$ structure, as there is no noticeable difference in the NiMnSb peaks. As for the V layer itself, the V (002) peak is not very prominent, being invisible for films with d_V = 30 Å V and only evident in the film with d_V = 100 Å grown at 200°C (Fig. 3.10a). This likely indicates significant interdiffusion at the V/NiMnSb interface above 200°C and poor crystallinity below 200°C. Comparison of the lattice parameters for the different NiMnSb films, shown in Table 3.1, shows relatively small variations, in the range (5.87– 6.09 Å) where half-metallicity persists from band structure calculations [60].

In order to determine the epitaxial relationship between the NiMnSb film, the V seed layer and the MgO substrate, it was necessary to determine the in-plane orientation of the films. This was accomplished using the pole figure attachment on a Rigaku RU200 diffractometer. This attachment allows the sample to be rotated in plane, as well as tilted at an angle (α) with

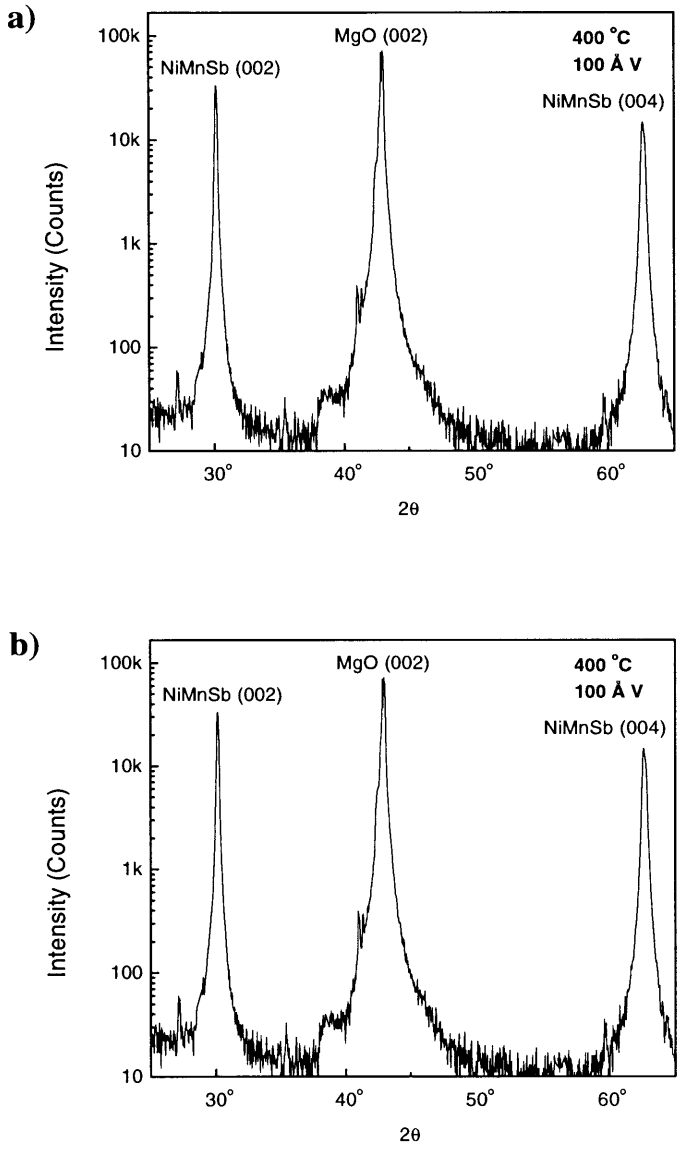

Figure 3.8: X-ray diffraction patterns for NiMnSb films grown at 400°C. a) 100Å V b) 30 Å V

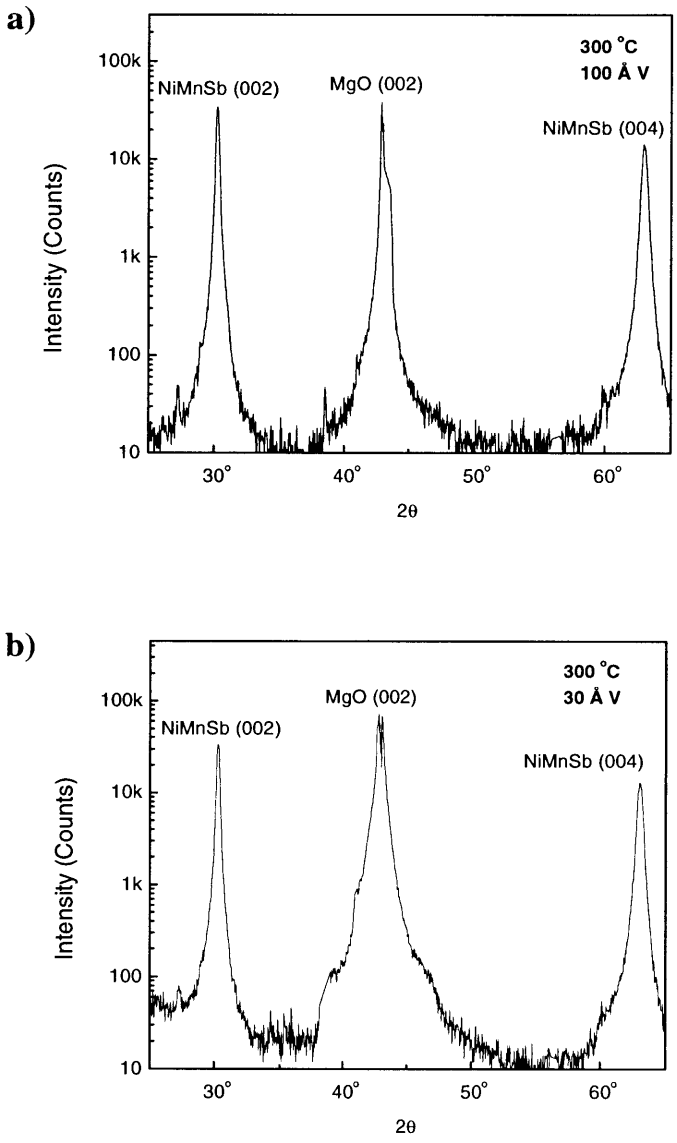

Figure 3.9: X-ray diffraction patterns for NiMnSb films grown at 300°C. a) 100Å V b) 30 Å V

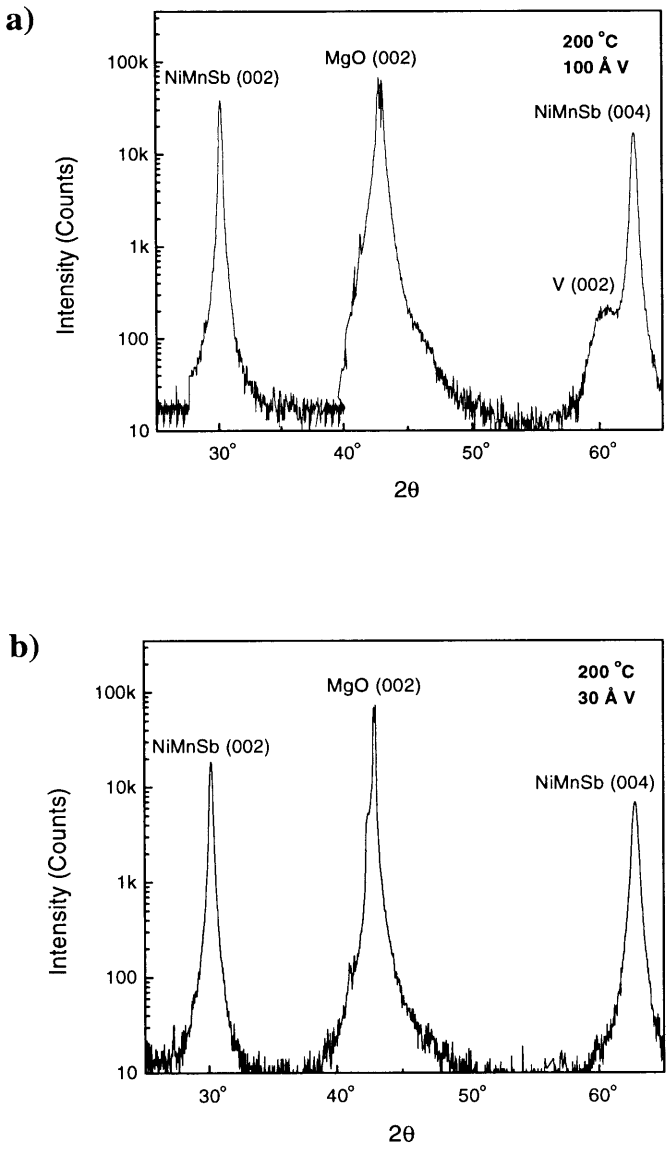

Figure 3.10: X-ray diffraction pattern for NiMnSb films grown at 200°C. a) 100 Å V b) 30 Å V

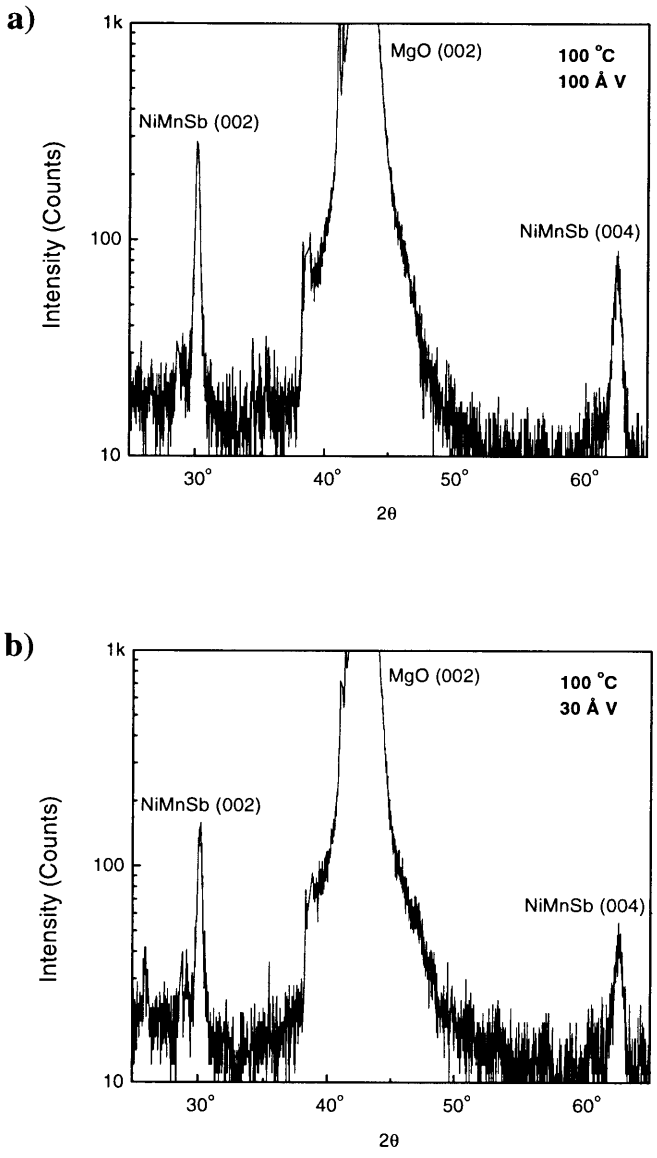

Figure 3.11: X-ray diffraction pattern for NiMnSb films grown at 100°C. a) 100Å V b) 30 Å V

Table 3.1: Lattice parameter (a) of the NiMnSb films.

T_S	d_V	a
400°C	100 Å	5.925 Å
400°C	30 Å	5.929 Å
300°C	100 Å	5.906
300°C	30 Å	5.899
200°C	100 Å	5.922
200°C	30 Å	5.918

respect to the plane of the incident beam and the detector, as shown in Fig. 3.12. The samples were tilted at $\alpha=35^{\circ}$, and θ and 2θ were fixed at 13.05° and 26.1° respectively to focus on the (111) peak of the NiMnSb. Rotation of the sample through the angle ϕ in plane then reveals the rotational symmetry of the NiMnSb film. The same was done at $\theta=18.455^{\circ}$ and $2\theta=36.910^{\circ}$ for the (111) peak of the MgO substrate. Fig 3.13, show the ϕ scans for the samples with 100 Å V seed layer grown at Ts = 200–400 °C. The ϕ scans for the 200°C and 300°C films show four peaks separated by 90° for both the NiMnSb and the MgO, which reflects the cubic symmetry of these materials. In fact, the peaks for the NiMnSb are 45° apart from MgO, which is the expected from the epitaxial relationship between the MgO, V and NiMnSb, *i.e.*, MgO [100] || V [110] || NiMnSb [110]. Interestingly, the 400 °C sample shows four additional peaks 45° from the main NiMnSb peaks, indicating twinned growth of the film.

In conclusion, the x-ray diffraction data shows good epitaxial growth of NiMnSb for the films grown at 200 to 400°C. The films grown at 100°C, however, shows much weaker diffraction peaks, indicating poor crystalline quality. Further studies thus focussed on the 200°C

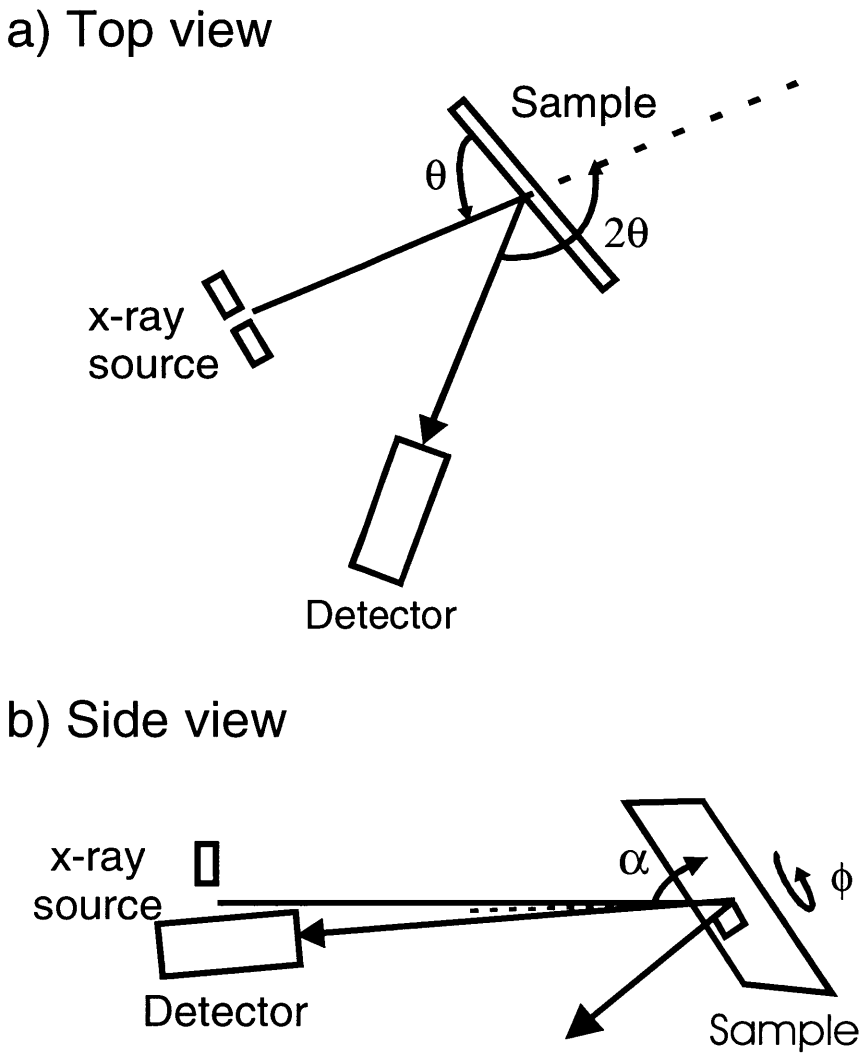

Figure 3.12: Schematic of in-plane ϕ scans.

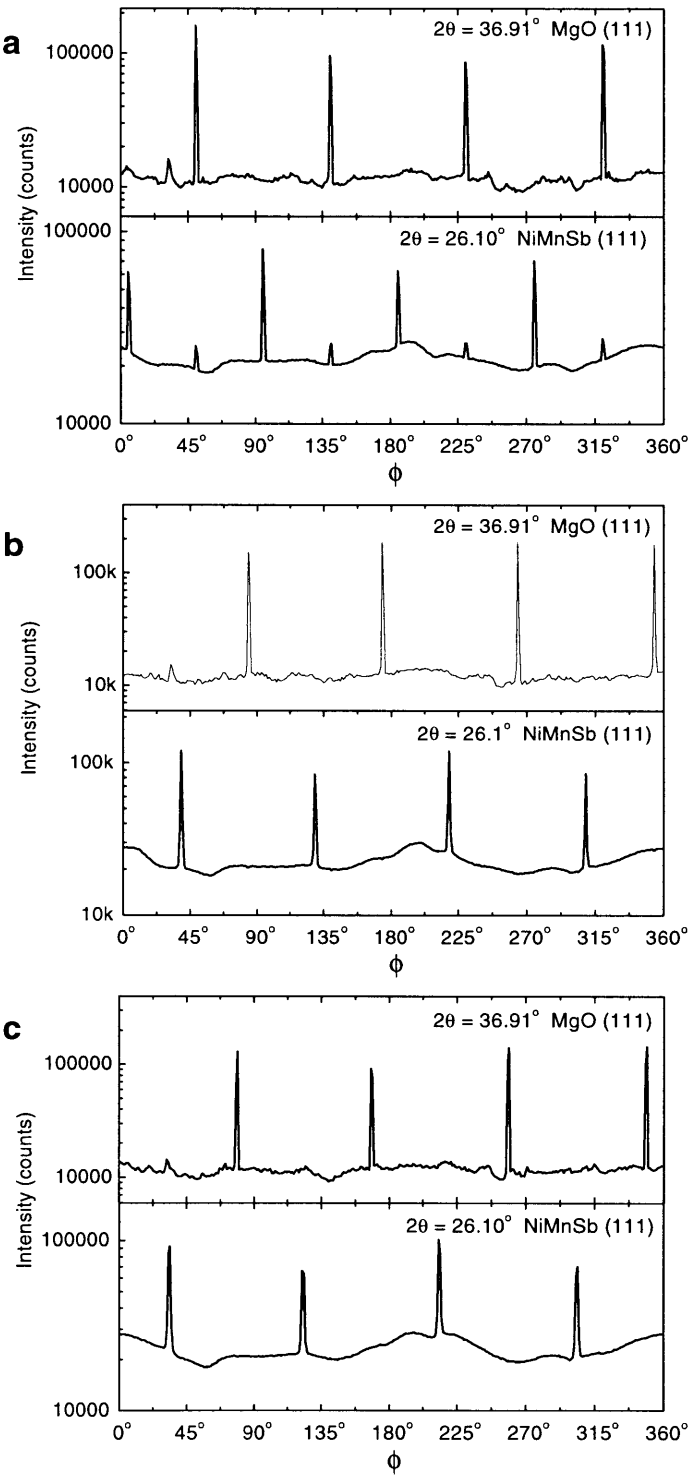

Figure 3.13: X-ray diffraction ϕ-scans for NiMnSb with d_V = 100 Å. The NiMnSb exhibits four-fold symmetry with unit cell 45° rotated from MgO(001) substrate. 400°C sample shows twinned growth. (a) 400°C (b) 300°C (c) 200°C

to 400°C samples.

3.5 Atomic Force Microscopy

As mentioned earlier, it is critical to grow a smooth NiMnSb layer in order to subsequently to grow a uniform Al_2O_3 tunnel barrier on top. To examine the surface roughness as a function of the growth parameters, we examined the films by atomic force microscopy (AFM) using a Burleigh Metris 2000 atomic force microscope. The AFM images are shown in Fig. 3.14a-f for the films grown at T_S = 400 to 200°C.

It is immediately obvious from the images that T_S has a major impact on the surface morphology of the films. The 400°C films, shown in Fig. 3.14a and 3.14b show an unusual microcrystalline topography, consisting of a number of isolated, square-faceted islands. The facets are rotated by 45° from the <100> directions of the MgO, which together with the x-ray diffraction data indicates that they are {100} planes. Comparing the film with d_V = 30 Å V to the one with d_V = 100 Å shows a slight difference between the two films, in that the former shows a more networked pattern of islands. The root mean square (RMS) roughness for the films are 340 Å and 410 Å, respectively, which makes them both unsuitable for making multilayer structures. Complete coverage of such a surface with ~15 Å is impossible. An interesting thing to note is that cross sectional views of the films reveal that the height of the islands is approximately 600-700 Å above the trenches in between them. In other words, the NiMnSb islands are slightly more than the nominal thickness (500 Å) above the trenches. The source of the C, O and V in the Auger spectra for these films is now revealed. The signal from these elements apparently comes from the trenches, which are largely or totally uncovered by the NiMnSb, exposing the V seed layer and substrate underneath. That the C and O comes from the substrate is confirmed by

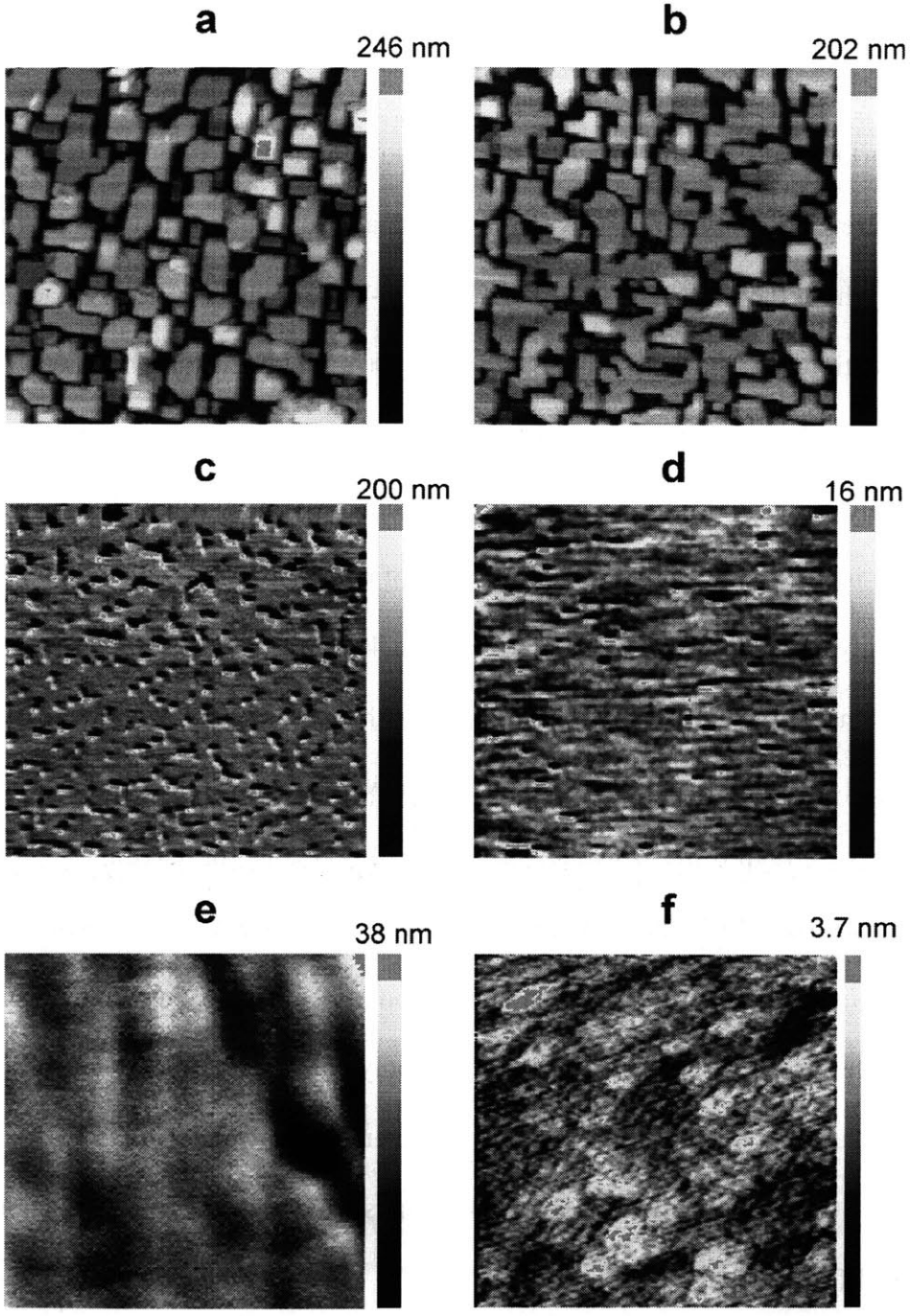

Figure 3.14: AFM images of NiMnSb films. Bar to the right of images sets the vertical scale. **a-d** are 7000 X 7000 nm. **e** and **f** are 700 X 700 nm. (a) $T_S = 400^oC$, $d_V = 100$ Å (b) $T_S = 400^oC$, $d_V = 30$ Å (c) $T_S = 300oC$, $d_V = 100$ Å (d) $T_S = 300^oC$, $d_V = 30$ Å (e) $T_S = 300^oC$, $d_V = 100$ Å (f) $T_S = 200^oC$, $d_V = 30$ Å

the fact that the C and O peaks in Fig. 3.3 are significantly smaller in the film with thicker V seed layer.

The surfaces of the films grown at 300°C, shown in Figs. 3.14c-d, look dramatically different and are marked by a number of craters with adjacent peaks. The depth of the craters as well as the height of the peaks are approximately 500-700 Å, which suggests that each of these sites is a nucleation site for the islands that form at 400°C. However, at the lower T_S, there is insufficient thermal energy for the nuclei to grow into the islands. This is supported by the comparison of the images for the different V layer thickness. The film with d_V=100 Å grown at 300°C, shown in Fig. 3.14c, shows a large number of nucleation sites when grown at 300°C. Correspondingly, the film with d_V = 100 Å grown at 400°C (Fig. 3.14a) shows more numerous, but smaller islands. In contrast, in the 300°C film with d_V = 30 Å V, fewer nucleation sites are present (Fig. 3.14d), and larger, networked islands develop in the 400°C film (Fig. 3.14b). The RMS roughness for both films grown at 300°C are still too large for making tunnel junctions; 27 Å for the film with d_V=30 Å and 330 Å for the film with d_V=100 Å. The presence of the nucleation sites would also make junction fabrication impossible, as these sites would likely result in pinholes in the Al_2O_3 tunnel barrier. It is only with a T_S of 200°C are suitable films observed with surfaces that are largely absent of craters, as shown in Fig. 3.14e-f. In fact, the film with d_V = 30 Å grown at 200°C (Fig 3.14f) shows RMS roughness of only about 6 Å, making it ideal for growing tunnel junctions.

Comparison of the images for different seed layers show that the films with larger d_V result in rougher films at a given temperature. This in qualitative agreement with the expectation of coherent growth for the 30 Å V layer and incoherent growth for 100 Å V, since the critical

thickness has been measured to be 50 Å [58]. To check this, V films of 30 Å and 100 Å were grown on MgO(001) substrates at 200°C and 400°C. The images are shown in Fig. 3.15. Examination of the 100 Å V samples (Fig. 3.15a-b) show virtually identical surface morphology, independent of the growth temperature. These films show grains of about 90 nm across, which is indicative of 3D island growth, rather than coherent 2D growth, as expected. The 30 Å V films are very difficult to image, but the 400°C sample (Fig 3.15c) does exhibit a granular structure, with grains ~25 nm across. The 30 Å V film grown at 200°C (Fig 3.15d) shows no real structure at all, and it is apparently beyond the capability of the instrument to image this surface. This is consistent with coherent growth, although further tests are needed to really prove this. These images at least show that it is possible to grow a very flat V seed layer which is important to subsequently grow a flat NiMnSb layer on top of it.

In conclusion, the AFM images show that the surface morphology shows strong dependence on both the growth temperature and the V seed layer thickness, with lower temperature and thinner V resulting in smoother films. The optimum growth conditions were found to be T_S = 200°C and d_V = 30 Å from the AFM images together with the x-ray diffraction data, as these result in very flat surfaces with good $C1_b$ NiMnSb formation

3.6 Magnetization data

As mentioned earlier, one of the fundamental requirements for a half-metallic ferromagnet is an integer moment (in μ_B) per formula unit, and this provides a test for HMF in these films. The films were characterized at room temperature using a Quantum MPMS SQUID magnetometer, with the magnetic field applied in the [110] direction in the plane of the NiMnSb

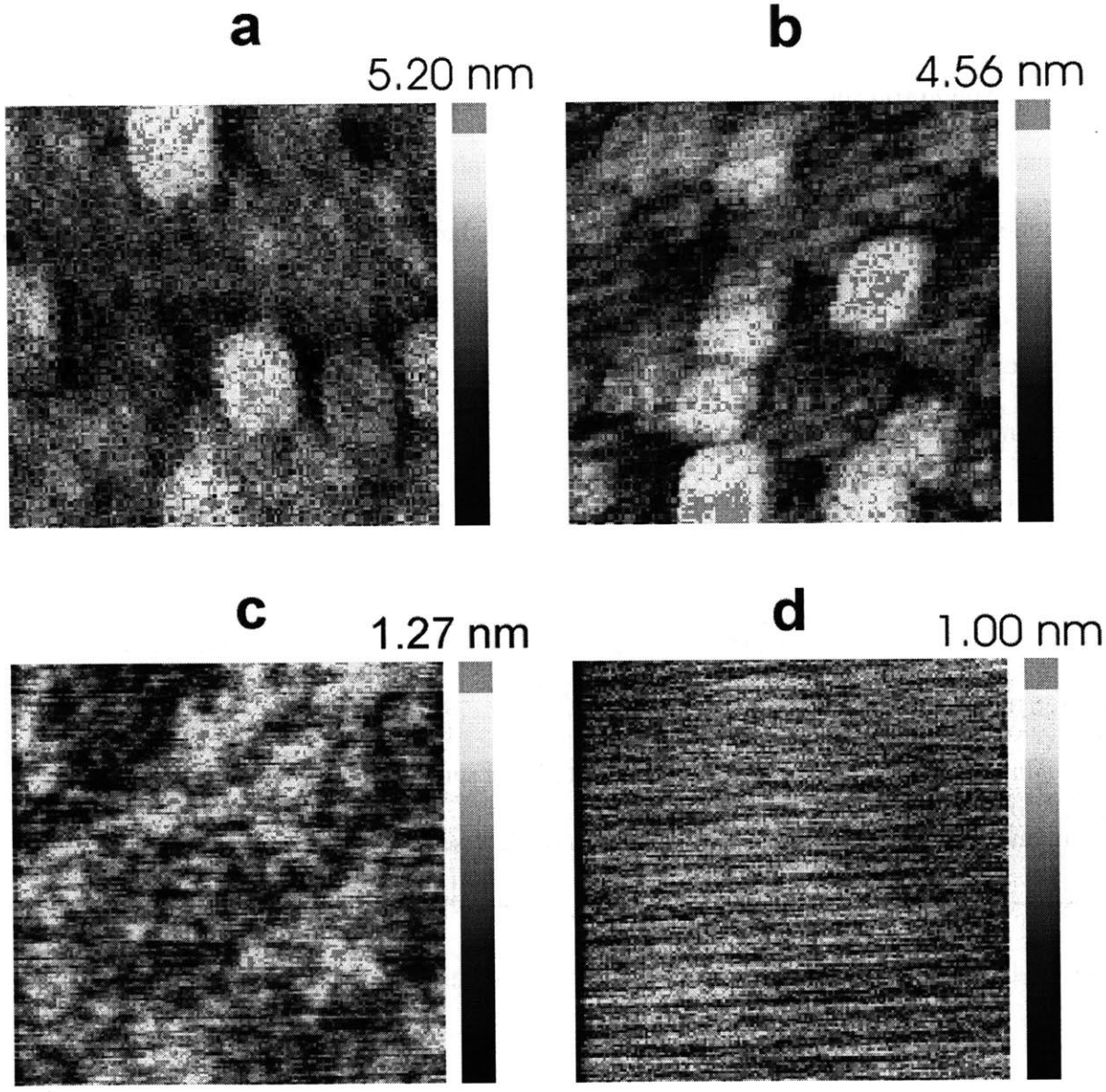

Figure 3.15: AFM images of V layers on MgO(001). Bars to the right indicate the vertical scale. Images are 350 X 350 nm. (a) 400°C, 100 Å V (b) 200°C, 100 Å (c) 400°C 30 Å (d) 200°C, 30 Å

film. The data is shown in Fig. 3.16 for the samples grown at T_S=200-400°C with d_V=100 Å. The saturation moment (M_S) for all three films is 3.8 ± 0.1 μ_B, per formula unit, which is in good agreement with the expected 3.9 μ_B at for bulk NiMnSb at room temperature [61]. The 200°C and 300°C films show very low coercivity, less than 20 Oe and relatively good remanence of about 0.8 M_S. In contrast, the 400°C sample shows very low remanence of about 0.05 M_S and require about 2000 Oe to saturate. This clearly reflects the microcrystalline topography of this film, in which the individual islands are for the most part, magnetically decoupled. As a result, the islands are demagnetized, since the demagnetizing factor for such roughly cubic islands is large. The islands themselves may also be close to the limit of thermal stability, since the magnetization curve looks very much like that corresponding to a superparamagnetic material. This is certainly possible, since the anisotropy energy for the islands is probably quite small; they are roughly cubes, and hence have no shape anisotropy.

Subsequent data on the tunnel junctions showed that the magnetocrystalline anisotropy in the NiMnSb films affected the shape of the magnetoresistance curves, and it is thus useful to measure the strength of this anisotropy. Hysteresis loops, shown in Fig. 3.17 were measured using a vibrating sample magnetometer along the [100] and [110] axes of the NiMnSb. This particular film was grown at T_S=200°C with d_V=30 Å. The saturation moment of 3.94 ± 0.1 μ_B per formula unit was found to be in good agreement with the expected 4 μ_B. The crystalline anisotropy is reflected in the coherent rotation of the magnetization from saturation to zero field. For a cubic crystal, the anisotropy energy is expressed as [62]

$$E_a = K_1(\alpha_1^2\alpha_2^2 + \alpha_2^2\alpha_3^2 + \alpha_3^2\alpha_1^2) + K_2(\alpha_1^2\alpha_2^2\alpha_3^2) + \cdots \qquad (3.1)$$

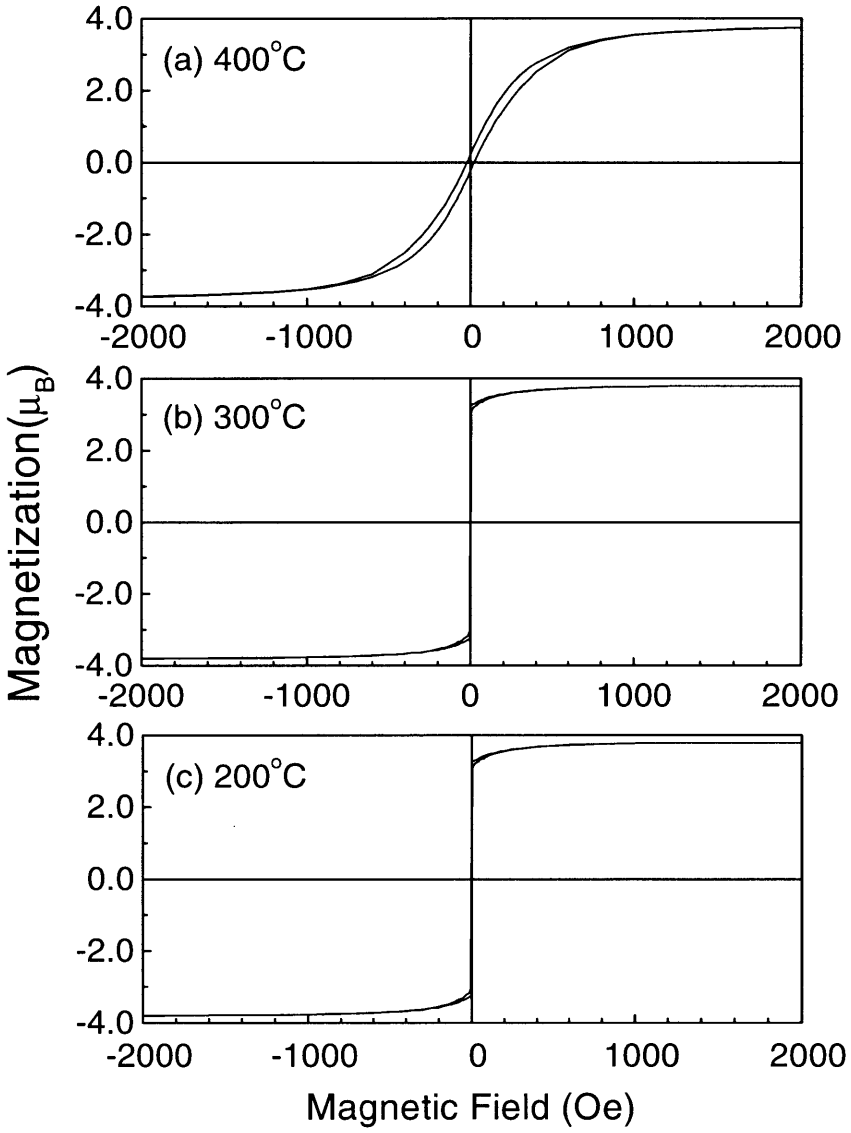

Figure 3.16: SQUID Magnetometer data for NiMnSb films with d_V=100 Å. (a) 400°C (b) 300°C and (c) 200°C. Data taken at 295 K with field applied along the NiMnSb [110] axis.

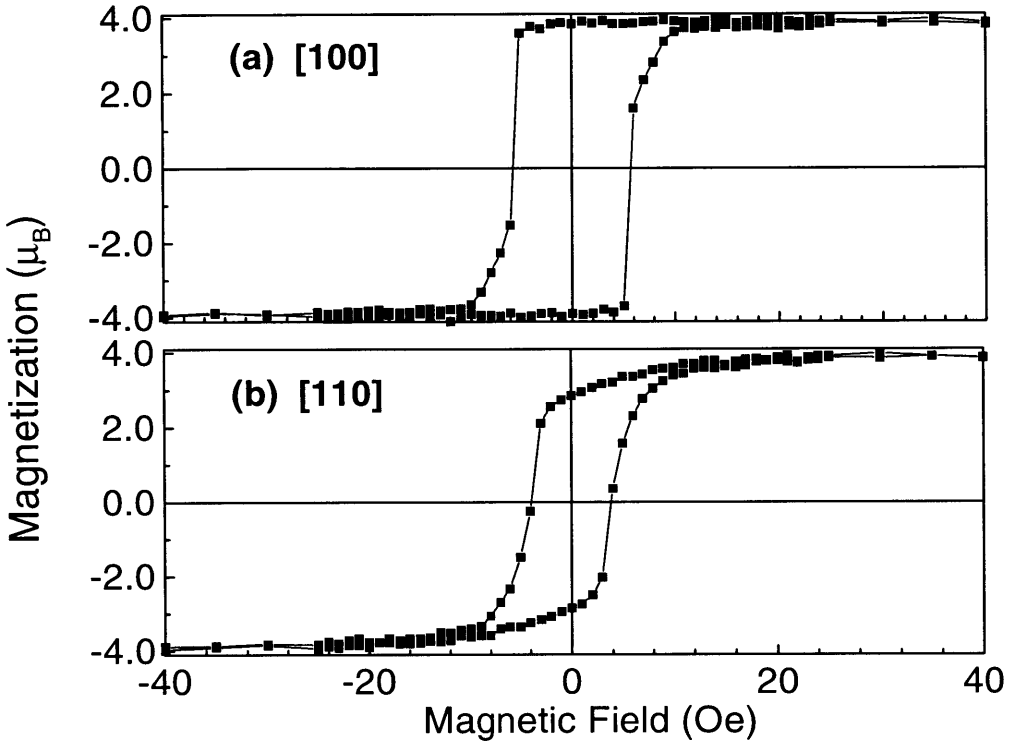

Figure 3.17: Magnetocrystalline anisotropy in NiMnSb film. Film grown at T_S=200°C with d_V=30 Å, measured by VSM at 295 K. (a) Field in [100] direction. (b) Field in [110] direction.

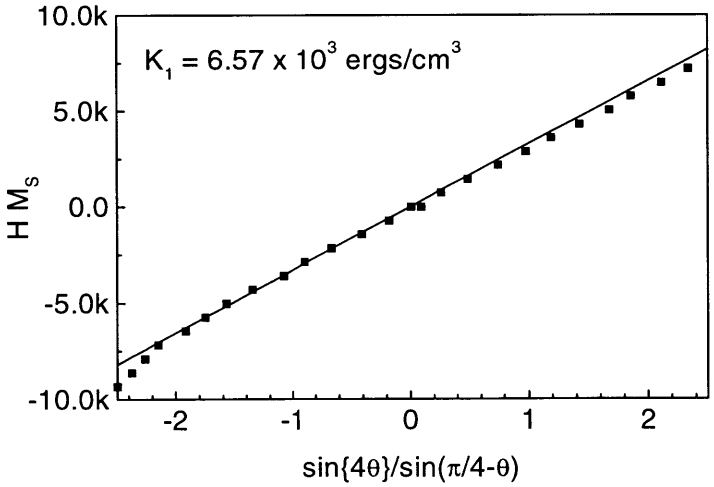

Figure 3.18: Fit for determination of anisotropy constant K_1. Data plotted is for the range from saturation to zero field in both directions. θ is determined from $M=M_S \cos(\pi/4-\theta)$.

where the α's are the direction cosines of the magnetization, and the K's are material constants. With the magnetization confined to the plane of the film and neglecting higher order terms, the expression reduces to

$$E_a = (K_1 / 4)\sin^2 2\theta \qquad (3.2)$$

where θ is the angle between the [100] axis and the magnetization direction. In applied field, H, applied along the [110] direction, the total energy is

$$E = (K_1 / 4)\sin^2 2\theta - M_S H \cos(\pi / 4 - \theta)\,. \qquad (3.3)$$

Energy minimization requires $dE/d\theta=0$, or

$$\frac{dE}{d\theta} = K_1 \sin 2\theta \cos 2\theta - M_S H \sin(\pi/4 - \theta) = 0\,. \qquad (3.4)$$

Since the measured magnetization, M, is given by $M_S \cos(\pi/4-\theta)$, we can determine the anisotropy constant K_1 by plotting M_SH vs. $\sin(4\theta)/\sin(\pi/4-\theta)$. The slope of this gives $K_1/2$. The fit is shown in Fig. 3.18. The straight line fit is very good and gives a value of 6.57×10^3 ergs/cm^3. The anisotropy is thus very small, which is reflected in the low saturation field of 20 Oe in the hard direction. In comparison, for example, Fe has K_1 of 4.8×10^5 ergs/cm^3.

In conclusion, the magnetic properties of the NiMnSb films are in good agreement with those expected for the HMF $C1_b$ compound, having virtually the full saturation magnetization of 4 μ_B per formula unit. Furthermore, the films grown at 200°C and 300°C show very sharp magnetization reversal and low coercivities, indicating minimal pinning due to defects or inclusions in the films. Also, weak magnetocrystalline anisotropy was observed for the film grown under optimum conditions for making tunnel junctions, which has implications for the behavior of the NiMnSb magnetic tunnel junctions.

Chapter 4: NiMnSb Spin Dependent Tunnel Junctions

Having established the optimum growth conditions for the NiMnSb thin films in the previous chapter, the next step is to investigate spin dependent tunnel junctions with these films to measure directly the NiMnSb conduction electron spin-polarization. This chapter outlines the fabrication of NiMnSb tunnel junctions, including the optimization of the tunnel barrier formation by plasma oxidation and ultraviolet assisted oxidation. Subsequently, the results using the spin-polarized tunneling technique of Tedrow and Meservey, as well as NiMnSb magnetic tunnel junction data, are discussed. Also presented is data on junctions with different NiMnSb film thickness, as this was found to have a significant influence on the properties of the NiMnSb. Finally, spin-polarization measurements using Andreev reflection in ferromagnet-superconductor point contacts are included.

4.1 Tunnel Junction Fabrication

The process of tunnel junction fabrication using standard ferromagnetic materials has become fairly well established over the last few years [63, 64]. The process flowchart for growing NiMnSb tunnel junctions is shown in Fig. 4.1. One notable change in the growth of the NiMnSb layer is the substrate cleaning procedure. The Auger data in Chapter 3 indicated that carbon contamination was present on the MgO substrates. Although it did not have any significant detrimental effects on the epitaxy of the deposited layers, its presence is nonetheless undesirable. For example, studies have shown that removal of carbon from sapphire substrates via ion beam bombardment resulted in improved V superconducting layers with greater stability

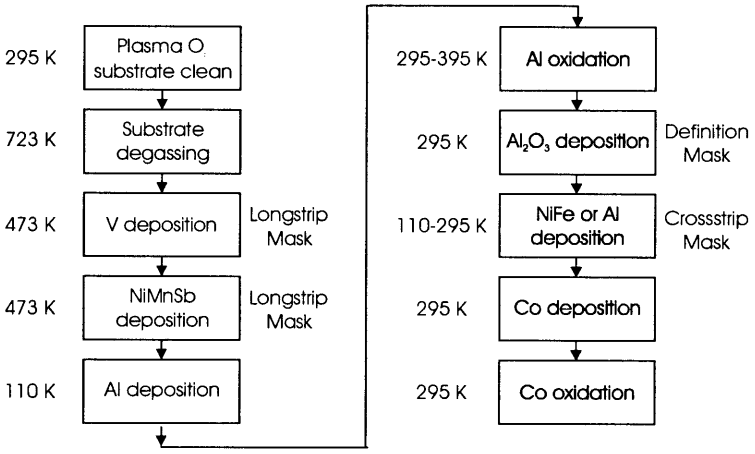

Figure 4.1: Process flow chart for NiMnSb tunnel junctions

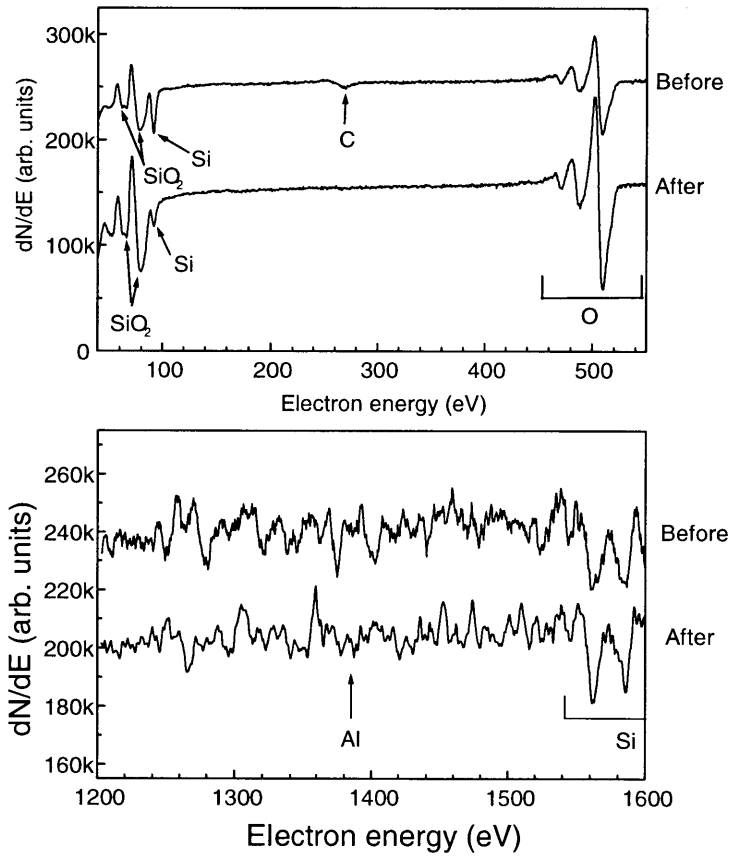

Figure 4.2: Auger spectra on Si wafer before and after plasma O_2 cleaning. Wafer shows no sign of carbon or sputtered Al after cleaning.

against thermal cycling [65]. The MgO substrates were thus cleaned in the load lock for one minute using an O_2 plasma at a pressure of 60 mtorr, a voltage of 1 kV and a current of ~100mA measured between cathode and ground. This procedure serves an additional purpose as well, the removal of the adsorbed gases, especially H_2O, from the glow discharge cathode and the surrounding areas. It is unacceptable for these gases to be released during the formation of the tunnel barrier itself since these gases would likely get incorporated into the Al_2O_3 and reduce the quality of the barrier. In fact the amount of gases removed from the surfaces around the glow discharge unit during this cleaning step was found to be substantial, sometime resulting in a twofold increase in pressure, from 60 mtorr to 120 mtorr. The effectiveness of this substrate cleaning was checked by examining a Si wafer by Auger spectroscopy before and after the procedure. The wafer had not undergone any cleaning procedure prior to loading into the system. The spectra, shown in Fig. 4.2, reveal total removal of the carbon KLL Auger peak after the plasma cleaning, as well as the absence of any Al, which could have been sputter deposited from the cathode.

The tunnel junctions were patterned into a cross geometry, shown in Fig. 4.3, by means of simple shadow masking during deposition using the available mask system. A broad strip of NiMnSb was deposited at T_S=200°C with d_V=30 Å V, as prescribed in Chapter 3. The subsequent 12-18 Å Al layer was deposited over the entire substrate at low temperature, ~110 K, to promote uniform coverage of the Al, as well as reduce any intermixing between the Al and NiMnSb. The cooling time to reach this temperature was about 1 hour, during which no significant amount of contamination should occur due to the level of vacuum (10^{-10} torr). This was confirmed by AES. After the Al deposition, the substrate was warmed to room temperature

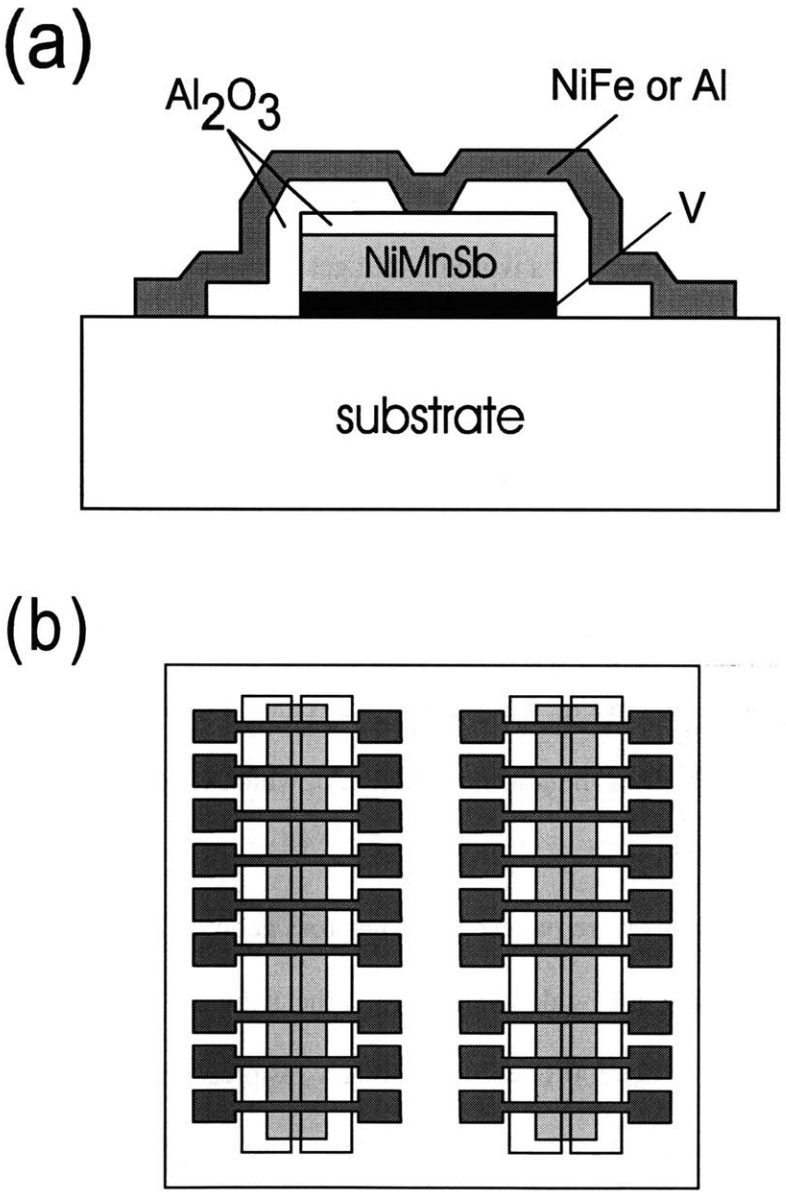

Figure 4.3: Cross geometry of NiMnSb tunnel junction. (a) Cross section of tunnel junction (b) Top view of a set of junctions.

and retracted to the load lock. The formation of the Al_2O_3 barrier was accomplished either by the more standard plasma oxidation method or by UV assisted oxidation, which will be described later. The plasma oxidation was performed in pure oxygen at 60-70 mtorr using a voltage of 1.2 kV. The current between the cathode and ground under these conditions was typically 100-150 mA. The substrate was rotated at a 90° angle, as shown in Fig. 3.2, rather than directly facing the glow discharge unit. This presumably leads to a gentler oxidation process, which in general gives more robust and stable tunnel barriers. Following the oxidation,a narrow tunnel junction area was defined using an Al_2O_3 masking layer deposited by e^- beam evaporation, which eliminated any tunneling contribution from the nonstoichiometric shadowed edges of the NiMnSb. Cross electrodes of either 40 Å Al (subsequently plasma oxidized to reduce the Al thickness to about 30 Å) at 110 K or 120 Å $Ni_{80}Fe_{20}$ (henceforth referred to as NiFe) at 295 K were used to form the ferromagnet/insulator/superconductor and ferromagnet/insulator/ ferromagnet tunnel junctions. The area of the completed junctions was approximately $5x10^{-4}$ cm^2. For the latter junctions, a thin layer of CoO was deposited on the NiFe as well. The antiferromagnetic (AF) CoO, grown by plasma oxidation of a 12 Å Co layer, allowed the NiFe to be exchange biased at low temperatures. Although a number of superior AF materials exist, the advantage of CoO is that strong exchange biasing can be achieved with films as thin as several Å, and, being an insulator, no shunting of the current occurs around the tunnel junction area by the AF layer. The latter eliminates the need for further patterning of the junctions, *e.g.*, by lithography.

4.2 Plasma oxidation of Al_2O_3 Tunnel Barriers

As mentioned previously, the FM/I interfaces of the tunnel junction are key to the quality of the tunnel junction, in terms of the FM spin-polarization well as the junction stability. It is thus critical to get a handle on the growth of the Al_2O_3 tunnel barriers. The FM/I/FM variety of tunnel junctions were used to characterize the quality of the tunnel barriers as a function of the Al_2O_3 growth parameters. This was primarily because useful information can be measured at room temperature or at 77 K, making the measurement far more convenient than for the FM/I/SC junctions.

Tunnel junctions were grown with Al thicknesses ranging from 12 Å to 18 Å, as well as for different oxidation times. Voltage and O_2 pressure were kept fixed at 1.2 kV and about 60-65 mtorr. In terms of the Al thicknesses, the optimization turned out to be not difficult, simply because only a very narrow range of Al thickness around 14 Å worked well, and, fortunately, this range was found quickly. For example, just below this range, with 12 Å Al the junctions were invariably less than 100 Ω and showed no significant JMR. This suggests that this amount of Al is insufficient to get total coverage of the NiMnSb, and, consequently, the tunnel barrier has pinhole shorts between the electrodes. In contrast, junctions with 16 Å or more Al were usually quite resistive (approximately tens of kΩ), but tended to be extremely noisy and unstable, with poor JMR. This behavior is in stark contrast to tunnel junctions with, for example, Co as the bottom electrode. It has been found that anywhere from 4 Å to 18 Å Al can be used to successfully get good Co/Al_2O_3/NiFe tunnel junctions [66]. The narrow range of useful Al thickness for NiMnSb junctions probably reflects the modestly higher surface roughness of the NiMnSb layers compared to Co layers deposited at cryogenic temperatures. Since the tunneling

probability is exponentially dependent on the thickness, even Å level roughness can play a significant role. . The greater tendency for Mn to oxidize than Co may also have an effect. We thus settled on 14 Å Al and varied the plasma oxidation time (t_{ox}) from 90 seconds to 180 seconds.

The relevant data measured for the junctions were the parallel state resistance (R_P), the JMR, defined as $(R_{AP}-R_P)/R_{AP}$, and the I-V characteristics. Junctions that appeared to be shorted and showed orders of magnitude lower resistance from its neighbors were excluded from the data. The data at 77 K was used for this study, since the higher voltages (~500-700 mV) required for the I-V data are less likely to short out the tunnel barriers at low temperatures. The R_P and JMR data are shown in Fig. 4.4. The data for 180 seconds is absent, as these junctions failed before completion of the measurement. This instability suggests that the oxidation was too long. The R_P and JMR data roughly shows a plateau in both quantities for t_{ox} between 105 and 115 seconds. The 90 second oxidation resulted in junctions that appeared to be shorted, with resistances under 100 Ω and no JMR. The JMR shows behavior which is in contrast with data for $Co/Al_2O_3/NiFe$ tunnel junctions, measured by van de Veerdonk, which showed a continuous increase in JMR for lower oxidation times [14]. Van de Veerdonk noted that theoretical calculations predict increasing JMR for decreasing tunnel barrier thickness. As indicated by the junctions with 12 Å Al, thinner tunnel barriers are apparently impossible to achieve on these NiMnSb films, and, hence, also the observation of the predicted increase in JMR. Additional information can be derived from fitting the I-V characteristics to Brinkman's formula [2] to derive the average barrier height and width. The barrier asymmetry is included in the fit, but not

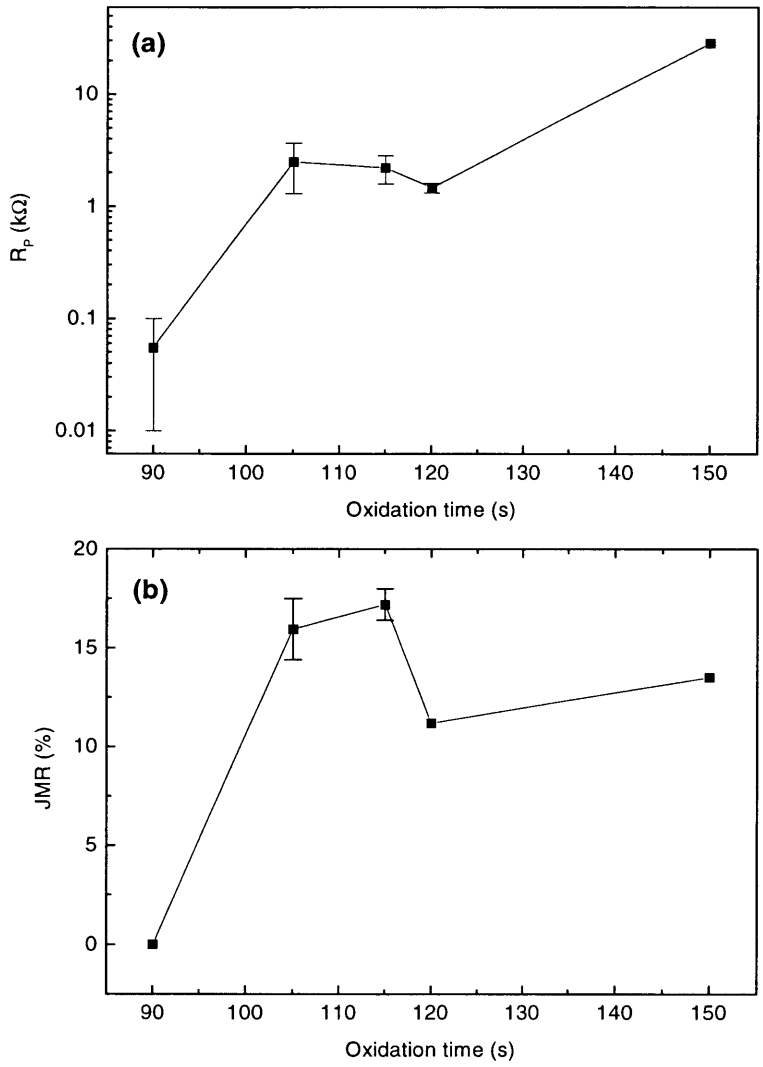

Figure 4.4: Parallel state junction resistance (R_P) and JMR as a function of oxidation time. Data is taken at 77 K. Error bars indicate the range of values observed.

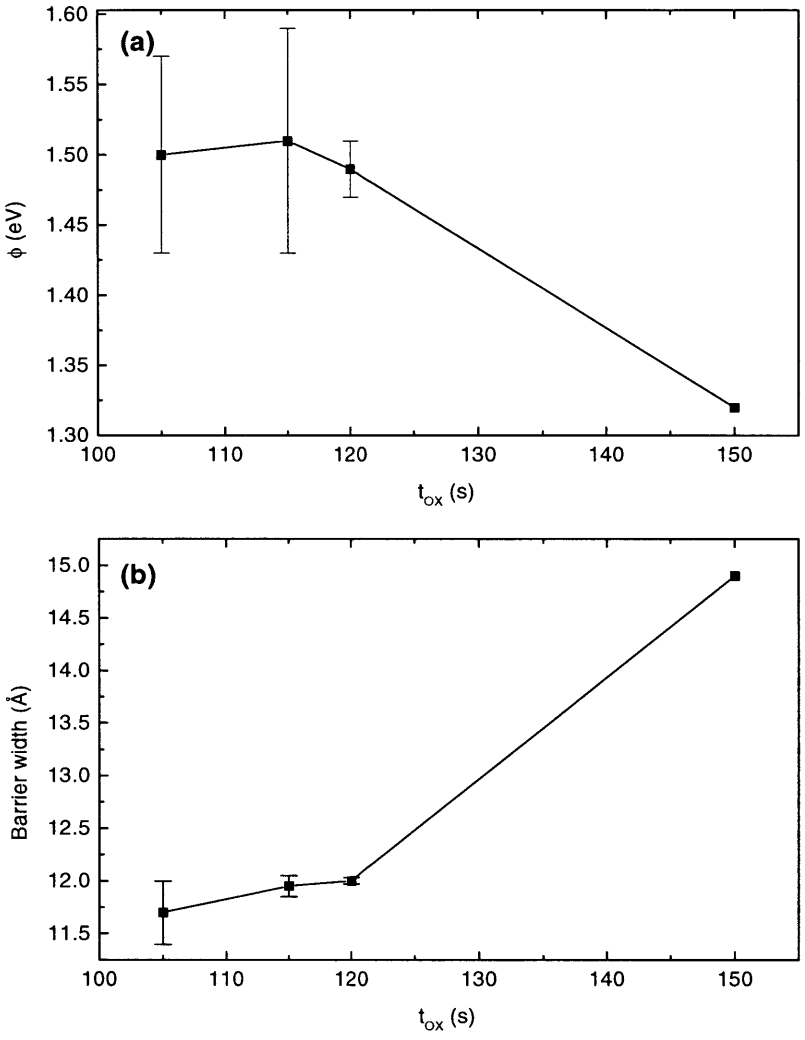

Figure 4.5: Tunnel barrier parameters as a function of plasma oxidation time. Data is from fit to Brinkman's formula. (a) Barrier height ϕ (b) Barrier width.

considered for comparison, since it is unclear if any useful information about the barrier quality and is contained in it. The data for the barrier parameters is shown in Fig 4.5. The barrier height shows a dramatic drop for t_{ox}=150 s, along with a corresponding increase in barrier width. These two facts reflect a lower quality tunnel barrier in this case, a strong indication that the oxidation has proceeded too far and oxidized some of the NiMnSb. The optimum oxidation time is apparently between 105 to 115 s, as the JMR and barrier height show a maximum at these points.

4.3 NiMnSb/Al_2O_3/Al Tunnel Junctions

Having established the optimum conditions for the tunnel barriers, NiMnSb/Al_2O_3/Al junctions were grown with 14 Å Al and t_{ox} of 115 s. The junctions were cooled to 0.4 K in a triple bath cryostat (liquid N_2, ^{4}He and ^{3}He), well below the Al critical temperature of ~ 2.8 K. The circuit used to measure the tunnel junctions is shown in Fig. 4.6. The dynamic conductance, dI/dV, was measured by an ac lock-in technique, with a 410 Hz, 20 μV ac modulation of the junction. The sample was mounted in a "tipping" probe, which allowed the angle of the sample to be adjusted in a controlled manner. Precise alignment of the Al film plane with the magnetic field was necessary for this measurement to minimize orbital depairing in the Al superconductor. This was achieved by minimizing dI/dV at zero voltage as the sample was tipped in a magnetic field of a few tesla (T).

The dI/dV data for a NiMnSb/Al_2O_3/Al tunnel junction in zero field and a field of 2.8 T are shown in Fig. 4.7. The zero field curve shows the superconducting energy gap of the Al film, with negligible leakage current at zero voltage indicating the high quality of the tunnel junction. With applied field, the superconductor quasiparticle density of states are Zeeman split, allowing

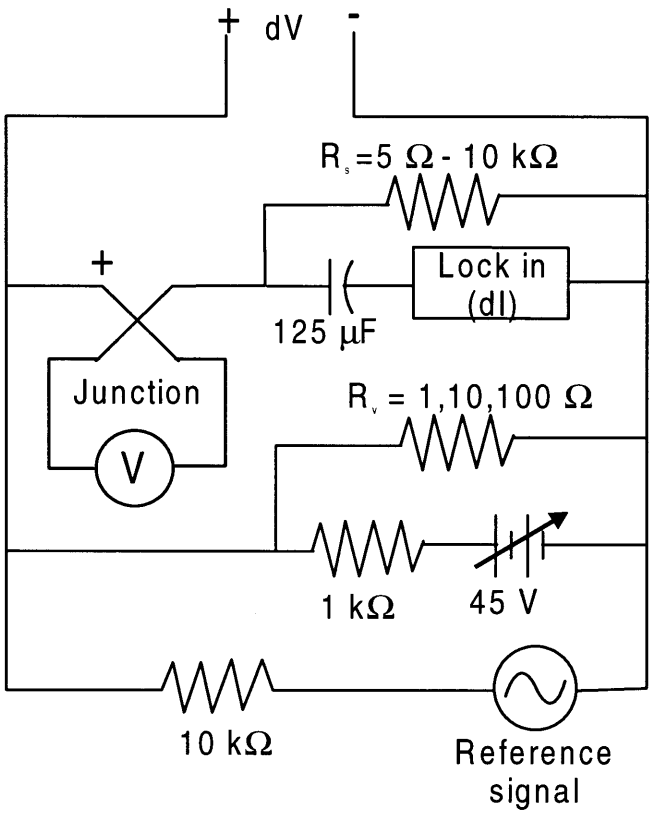

Figure 4.6 Circuit for dI/dV measurement.

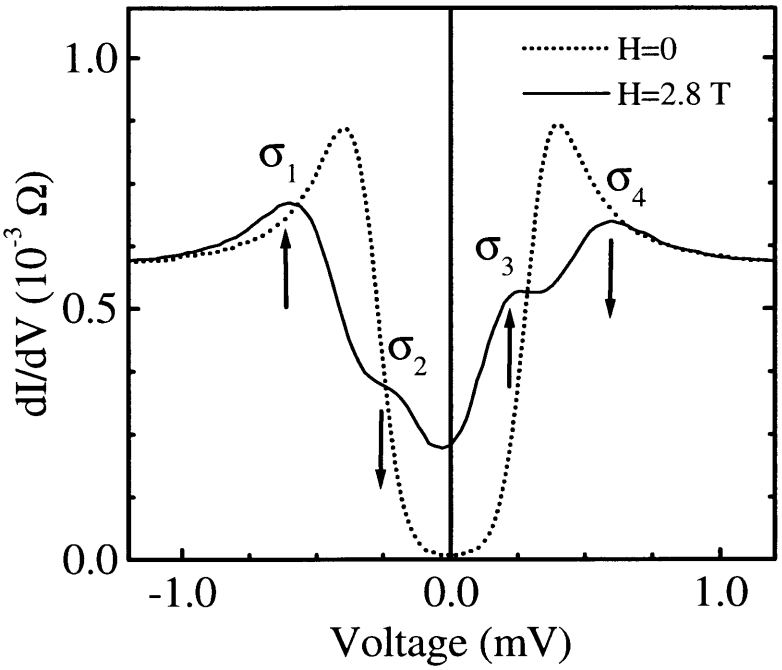

Figure 4.7: Spin-polarized tunneling in NiMnSb/Al_2O_3/Al junction. Data taken at 0.4 K

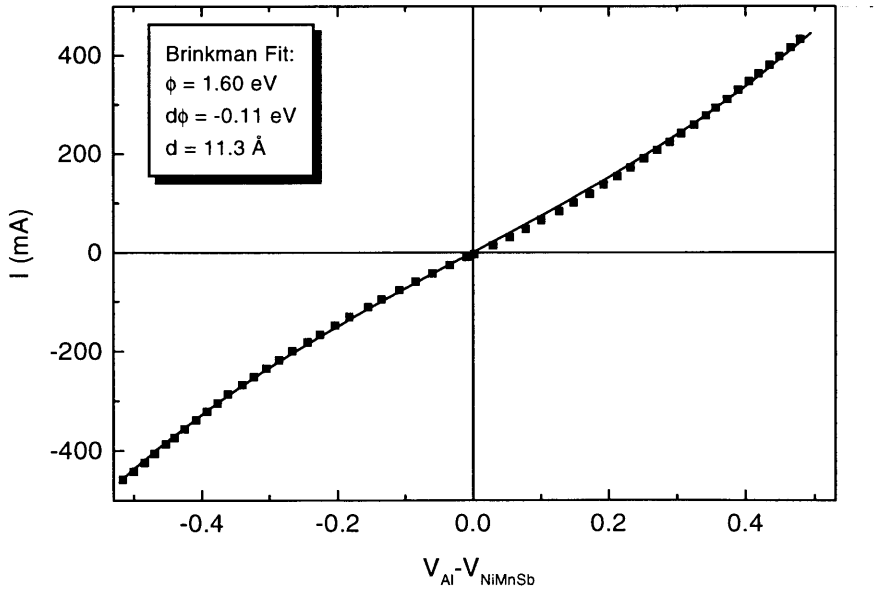

Figure 4.8 Current-voltage characteristics for NiMnSb/Al_2O_3/Al junction. Solid line represents the fit to Brinkman's formula.

the tunnel current to be resolved into spin up and spin down parts. The asymmetry of the dI/dV curve at 2.8 T reflects the spin-polarized tunnel current from the NiMnSb. The value for P can be calculated using Equation (1.8), reproduced here for convenience [4]

$$P = \frac{(\sigma_4 - \sigma_2) - (\sigma_1 - \sigma_3)}{(\sigma_4 - \sigma_2) + (\sigma_1 - \sigma_3)} . \qquad (1.8)$$

A value of 28 ± 2% for P is obtained for NiMnSb, including the 8% correction for spin-orbit scattering in the Al film. Two other junctions from this set of junctions showed the same value. This is in fact the first direct measurement of P using the spin-polarized tunneling technique of Tedrow and Meservey in any of the predicted half-metallic ferromagnets.

Following the polarization measurement, the I-V characteristic was measured for the junction at higher bias voltages. This allowed the effective barrier parameters to be determined by fitting the data to Brinkman's formula, Eqn. (1.3). The data is shown in Fig. 4.8, along with the results of the fitting procedure. The barrier height (ϕ) and asymmetry were 1.60 eV and 0.11 eV, respectively, and the barrier width was 11.3 Å. The barrier height is consistent with good Al_2O_3 tunnel barriers, which typically show 1.5-3 eV. The barrier width is lower than the nominal 18 Å Al_2O_3 expected from the 14 Å Al barrier for this junction. This probably reflects the roughness of the FM/I interfaces which results in non-uniformity in the tunnel barrier. In that case, the tunnel current is dominated by the areas with thinner barrier due to the exponential dependence of the tunneling probability on barrier thickness.

4.4 NiMnSb/Al_2O_3/NiFe/CoO Tunnel Junctions

Ferromagnet/insulator/ferromagnet junctions were grown under identical growth conditions as the FM/I/SC junctions. The JMR of these junctions were measured using a standard dc four-terminal configuration with the field applied along a NiMnSb [100] easy axis to achieve sharp reversal of the NiMnSb magnetization. For the low temperature measurements, the junctions were cooled in an applied field of about 300 Oe in this direction, in order to exchange bias the NiFe upper electrode using the AF CoO layer.

The junction resistance (R_J) vs. field data for a NiMnSb/Al_2O_3/NiFe/CoO junction at 295 K, 77 K and 4.2 K are shown in Fig. 4.9. Note that R_P for the best set of junctions showed a modest 30% rise in resistance between 295 K and 4.2 K. This is comparable to the best Co/Al_2O_3/NiFe junctions, which typically show 15-20% increase. The increase can be attributed to a number of things, but in general is due to the freezing out of inelastic tunneling processes at low temperature. These processes could include hopping from states at the FM/I interface or states within the barrier itself, magnon or phonon assisted processes, among other things [30]. The shape of the R_J vs. H curves can be explained by Julliere's model for FM/I/FM tunneling [20]. Minimum R_J is obtained when the two FM magnetizations are parallel; maximum R_J when they are antiparallel. The JMR rises quite dramatically between 295 and 77 K, and much of this rise is due to the pinning of the NiFe layer. With the NiFe magnetization fixed, full antiparallel alignment of the FM electrodes is easily achieved below 295 K. In comparison, the 295 K curve is quite sharply peaked, and it is likely that the magnetizations of the FMs are not fully antiparallel at the peak. Also responsible for the JMR increase are the intrinsic increase in surface polarization of the FMs in the FM/I/FM junctions, typically observed with decreasing

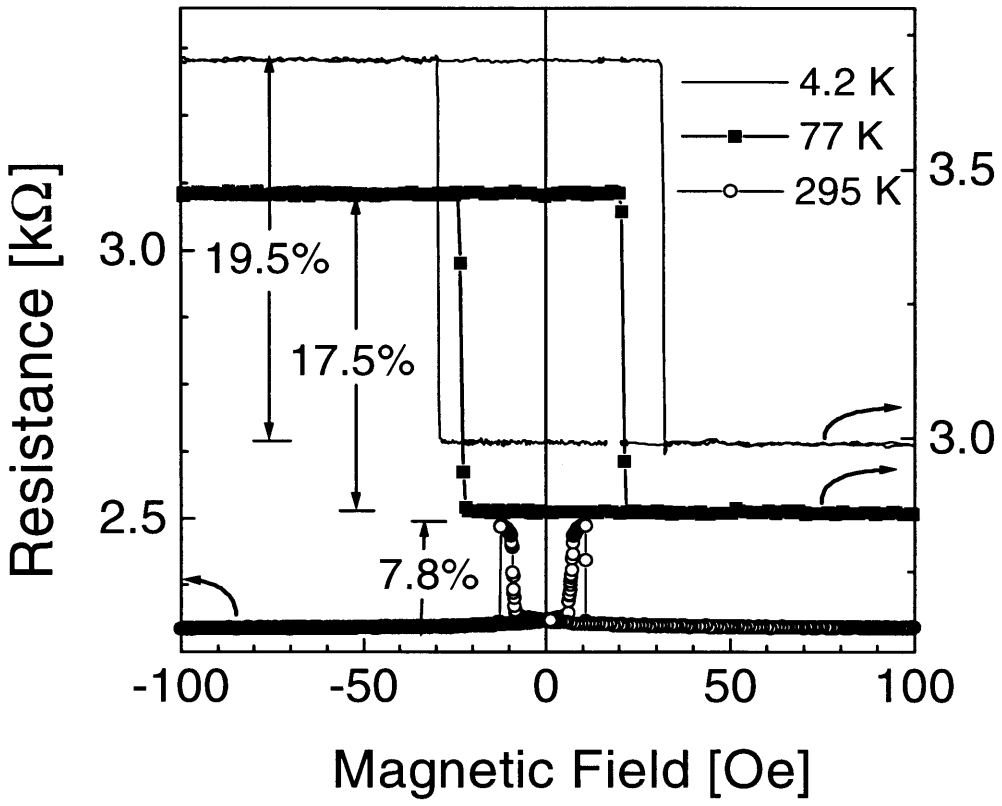

Figure 4.9: Magnetoresistance for NiMnSb/Al_2O_3/NiFe junction. Left axis corresponds to 295 K data; right axis to 77 K and 4.2 K data.

temperature, as well as the freezing out of the aforementioned inelastic tunneling processes [30]. The polarization of the NiMnSb can be deduced from Julliere's model of FM/I/FM tunneling [20], Eqn. (1.9), reproduced here for convenience

$$JMR \equiv \frac{\Delta R}{R_{AP}} = \frac{2P_1P_2}{1+P_1P_2}. \qquad (1.9)$$

The P for NiFe is known to be 45% from spin-polarized tunneling experiments [14], and solving for P_{NiMnSb}, using the maximum JMR of 19.5%, gives P_{NiMnSb} of 25%. This is in good agreement with the value from the FM/I/SC measurements. Several junctions made using these optimal process parameters showed roughly equivalent JMR values of between 18.5-19.5%.

Tunnel barrier quality was again measured for this junction by measuring I-V characteristics, shown in Fig. 4.10 and fitting for the barrier parameters. The barrier height and width are roughly constant between 295 K and 4.2 K, showing only modest changes, from 1.55 eV to 1.63 eV and 11.8 to 11.7 Å, respectively. The barrier parameters are comparable to those measured for the NiMnSb/Al_2O_3/Al junctions and indicate high quality junctions. Additional information on the possibility of a minority spin energy gap can be found by examining the differential conductance (dI/dV) and the bias voltage dependence on the JMR. The dI/dV vs. V should reflect the band structure of the FM electrodes. In most cases the energy band information is obscured by other effects, particularly inelastic processes, but a pronounced feature like a minority spin gap should be visible. Although only one of the electrodes is half-metallic some spectroscopic information might still be observable. The dI/dV data at 295 K, 77 K and 4.2 K are shown in Fig 4.11. A minority spin energy gap is expected to manifest itself as a pronounced increase in dI/dV at the edges of the gap for the antiparallel orientation, resulting

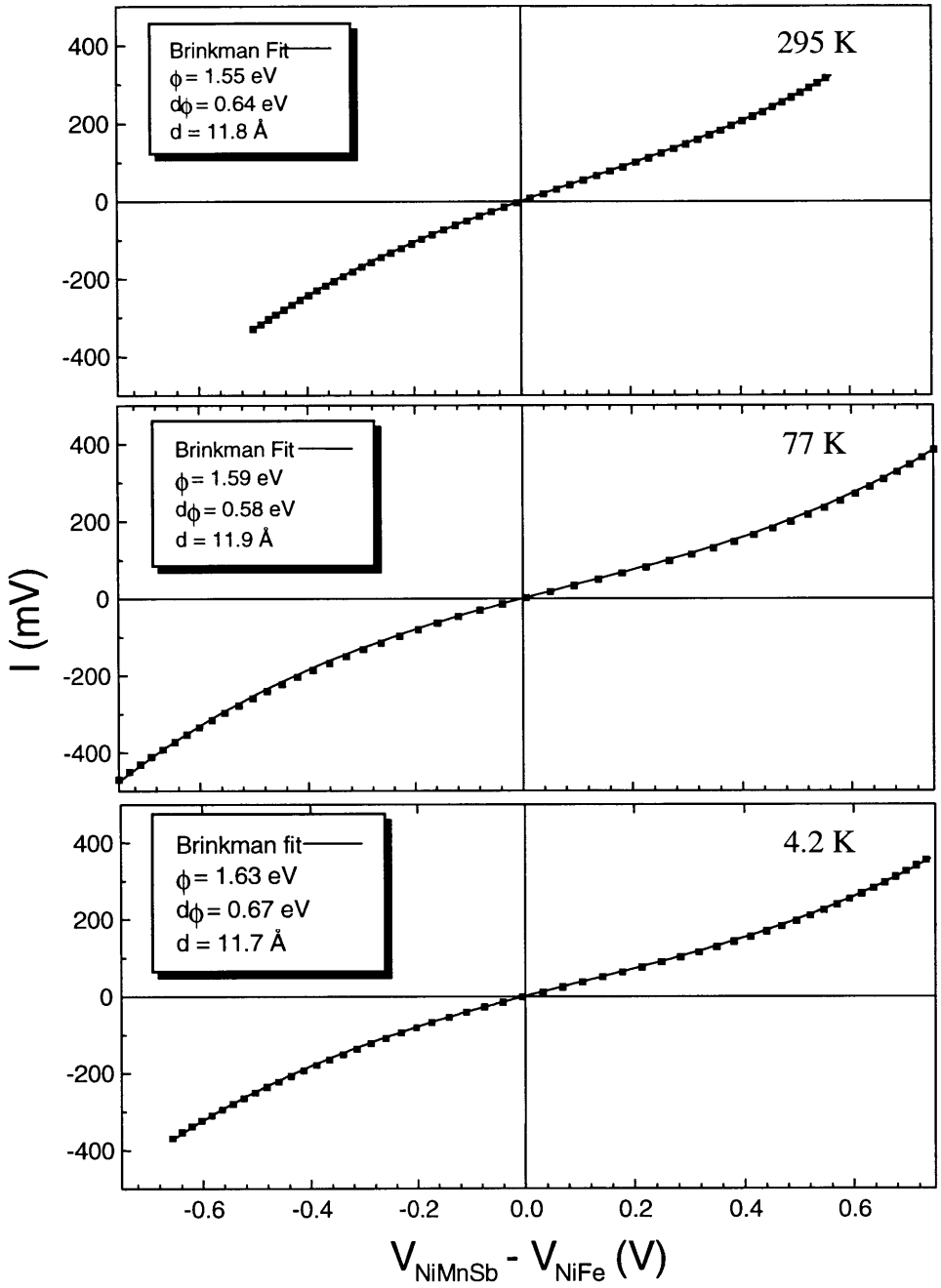

Figure 4.10: I-V characteristics for NiMnSb/Al_2O_3/NiFe junction. Solid line is the Brinkman fit through the data points.

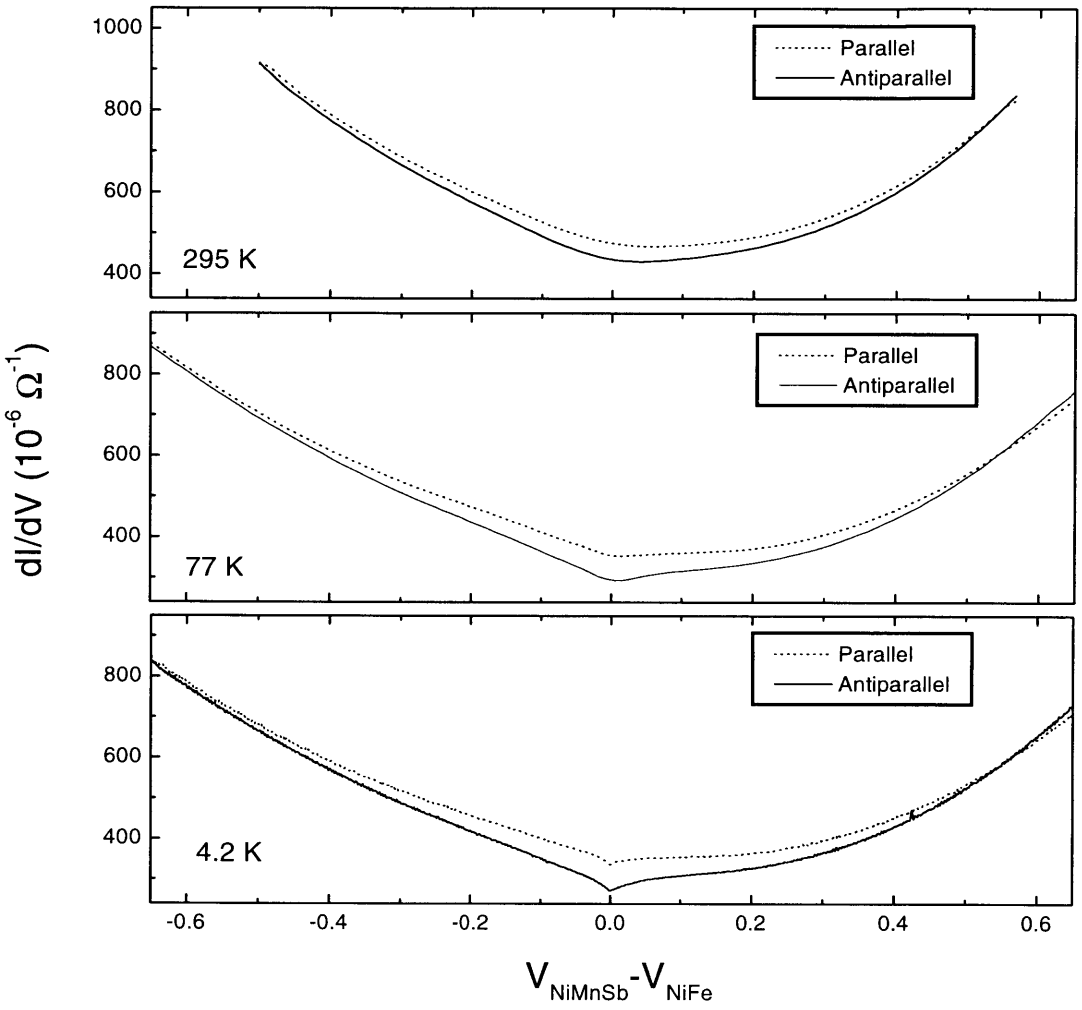

Figure 4.11 Differential conductance of NiMnSb/Al_2O_3/NiFe/CoO Tunnel Junction.

from the onset of minority spin states. However, no such feature is observed in the dI/dV data.

The minority spin gap should also affect the bias voltage dependence of the JMR, shown in Fig. 4.12. The JMR is expected to display a pronounced decrease in JMR around the voltages corresponding to the gap edges. Again, no extraordinary feature is found, and the curves show no evidence of an energy gap. Another aspect of tunneling for a half-metallic electrode is the absence of magnon excitations. This is expected to lead to a slower decline in magnetoresistance with voltage, since the cusp-like feature commonly observed has been attributed to magnon-assisted tunneling. Only one of the electrodes is NiMnSb, but a slower decrease might still be expected. However, the data still exhibits a characteristic cusp at low temperatures, as pronounced as in a $Co/Al_2O_3/NiFe$ junction. The cusp is smeared out at 295 K, probably due to the existence of other inelastic transport processes which depress the JMR value. This is commonly observed in normal FM junctions as well.

The influence on the magnetocrystalline anisotropy of the NiMnSb was also observed in these junctions. The junction magnetoresistance (JMR) was measured with magnetic field applied at different angles (θ) with respect to the NiMnSb [100] axis. Fig. 4.13 shows the R_J vs. H curves at 295 K for θ=0, 20° and 45°. In Fig. 4.13a, the field is applied along the NiMnSb[100] easy axis. As the field is increased in the reverse direction, the initial rise in R_J is caused by the reversal of the soft NiFe magnetization ($\mathbf{M}_{NiFe}$). The subsequent sudden drop indicates that the NiMnSb magnetization ($\mathbf{M}_{NiMnSb}$) reverses direction in a single step. In contrast, for θ=20°, in Fig. 4.13b, two sharp drops in R_J shows $\mathbf{M}_{NiMnSb}$ switching in 90° steps, from the [100] to the [010] direction before finally switching to the $[\bar{1}00]$ direction. In Fig. 4.13c,

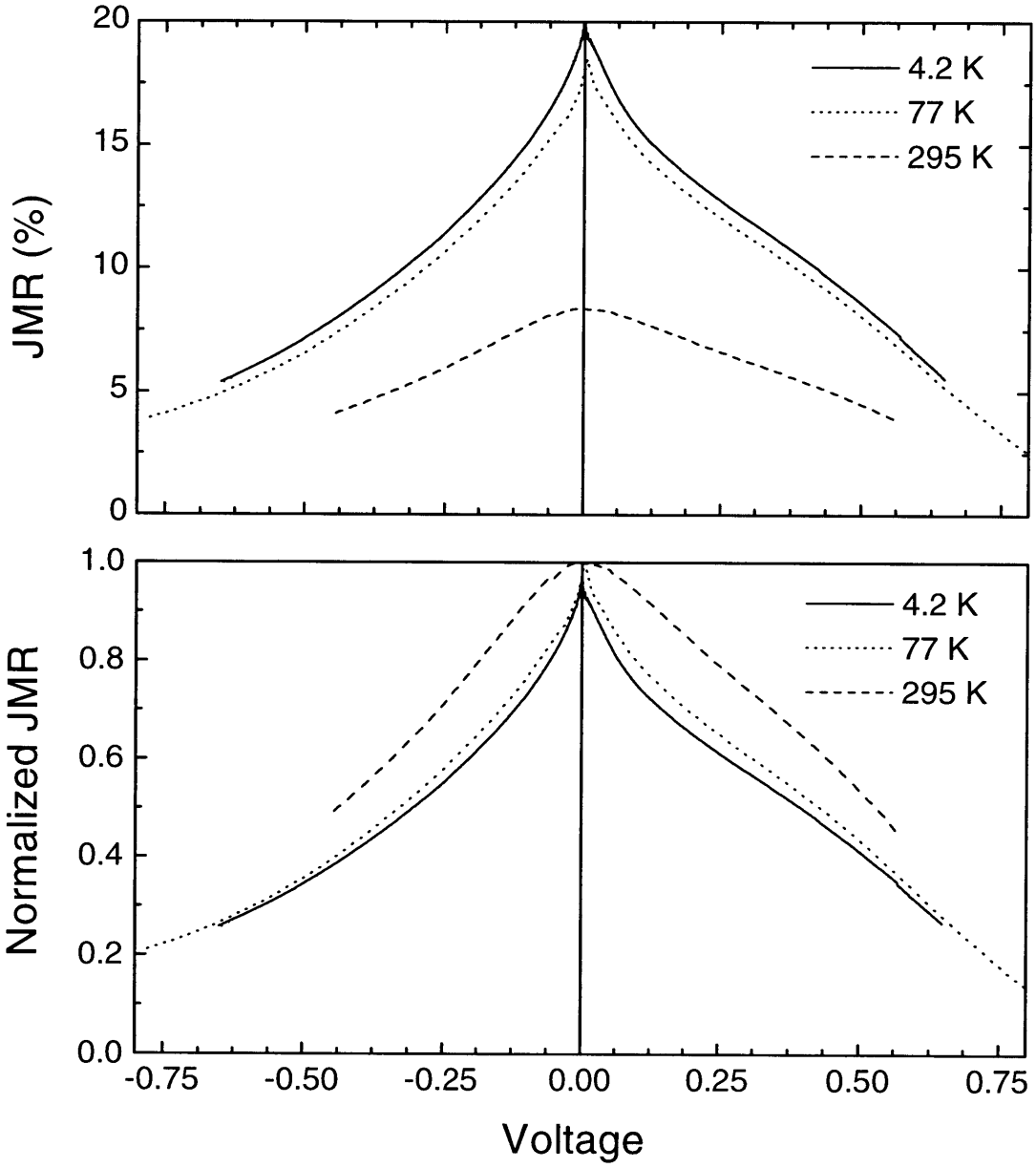

Figure 4.12: Bias dependence of magnetoresistance in NiMnSb/Al_2O_3/NiFe/CoO tunnel junction. Bottom curve is normalized to the zero voltage JMR.

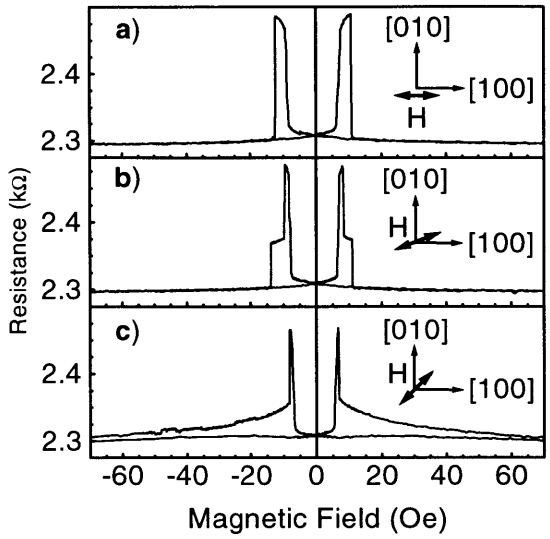

Figure 4.13: Magnetocrystalline anisotropy in NiMnSb/Al_2O_3/NiFe/CoO junction at 295 K. Inset shows the direction of the field with respect to the NiMnSb crystalline axes.

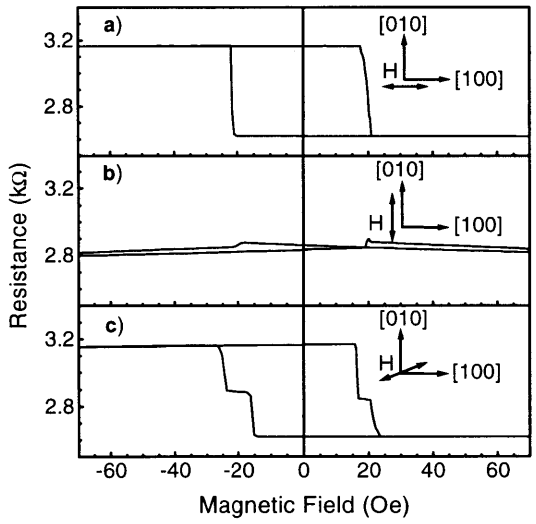

Figure 4.14: Magnetocrystalline anisotropy in NiMnSb/Al_2O_3/NiFe/CoO junction at 77 K. Inset shows the direction of the applied field with respect to the NiMnSb crystal axes. NiFe exchange biased in [100] direction.

applying the field along the [110] hard axis suppresses this second drop, and the final magnetization reversal occurs purely by the rotation of $\mathbf{M}_{NiMnSb}$. These measurements illustrate the four-fold symmetry of the NiMnSb, with easy axes in the <100> directions.

The hysteresis of the NiMnSb magnetization becomes clearer after cooling the junctions to 77 K in a magnetic field ($\mathbf{H}_{bias}$) along the NiMnSb [100] direction. The resulting strong exchange bias pins the magnetization of the NiFe layer, and the change in R_J then depends only on the direction of $\mathbf{M}_{NiMnSb}$. Maximum JMR of 18.0% is observed when the field ($\mathbf{H}$) is applied parallel to ($\mathbf{H}_{bias}$), in which case the R_J vs. H curve is a simple square hysteresis loop (Fig. 4.14a), indicating complete antiparallel alignment at the maximum in R_J. For $\mathbf{H} \perp \mathbf{H}_{bias}$, (Fig. 4.14b), the JMR nearly vanishes, since $\mathbf{M}_{NiFe}$ and $\mathbf{M}_{NiMnSb}$ remain perpendicular throughout the sweep. Finally, when the field is applied 20° from $\mathbf{H}_{bias}$ (Fig. 4.14c), $\mathbf{M}_{NiMnSb}$ reverses as it did at room temperature with two sharp transitions in both directions of the field sweep, each corresponding to 90° change in $\mathbf{M}_{NiMnSb}$.

It is clear that four stable remanent magnetization states are possible for the NiMnSb due to its cubic magnetocrystalline anisotropy. However, when the NiFe is biased in the NiMnSb [100] direction as in the previous case, two of those states have equal R_J. Four distinct R_J states can be observed by biasing the NiFe slightly off the NiMnSb[100] direction. The JMR and memory effect when $\mathbf{H}_{bias}$ is 22° from the [100] direction of the NiMnSb is shown in Fig 4.15. As expected, four nonvolatile remanent R_J states are evident, each separated by more than 4.5%. From an application point of view, it should be noted that the JMR falls as approximately $\cos \theta_B$ for small θ_B, where θ_B is the angle between the [100] axis and the bias direction, so at $\theta_B = 22°$, the JMR is still above 90% of the maximum value. Further, although the four-state spin

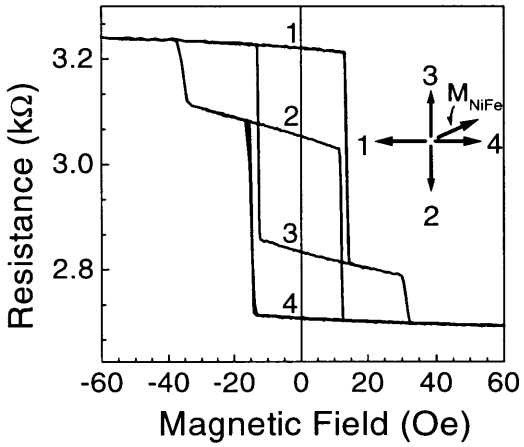

Figure 4.15: Four-state spin-tunneling device. Inset shows the magnetization direction for the four states, along with the pinning direction of the NiFe magnetization.

tunneling device is demonstrated here at 77 K, room temperature operation can be easily achieved by using an antiferromagnet with higher Neel temperature such as FeMn. This would separate the switching fields of the two FMs and give higher JMR at 295 K. The actual utility of such a four-state device for information storage is as yet unclear, but it does offer a possible alternative for increasing storage density in memory applications, *i.e.*, increasing the storage capacity for each individual device rather than the packing density of the devices.

4.5 Dependence of Magnetoresistance on NiMnSb Thickness

Tunneling results were measured for NiMnSb junctions of different thicknesses, ranging from 150 Å to 800 Å. These revealed that the properties of the NiMnSb varied strongly with film thickness. The JMR curves for NiMnSb/Al_2O_3/NiFe junctions with 150 Å, 300 Å, 500 Å and 800 Å are shown in Fig. 4.16. For the lowest NiMnSb thickness, 150Å, the junctions show significantly lower magnetoresistance (MR) than the higher thicknesses. The shape of the curve for these junctions indicates a higher coercity for the NiMnSb, as well as a much more gradual magnetization reversal, in contrast to the sharp reversal in the thicker films. Note that the 150 Å NiMnSb junctions are not exchange biased with CoO at 77 K.

The JMR curves suggest strong pinning of the NiMnSb at low film thicknesses. As a result, we measured the magnetoresistance (MR) for NiMnSb films ranging from 100 Å to 500 Å, since the MR of the FM electrode itself can often give information about the process of magnetization reversal. The NiMnSb MR data is shown in Fig. 4.17, measured with field both parallel and perpendicular to the current. The MR data shows markedly different behavior for the 100 Å film in that it shows *isotropic* MR. This is in fact similar to the MR commonly

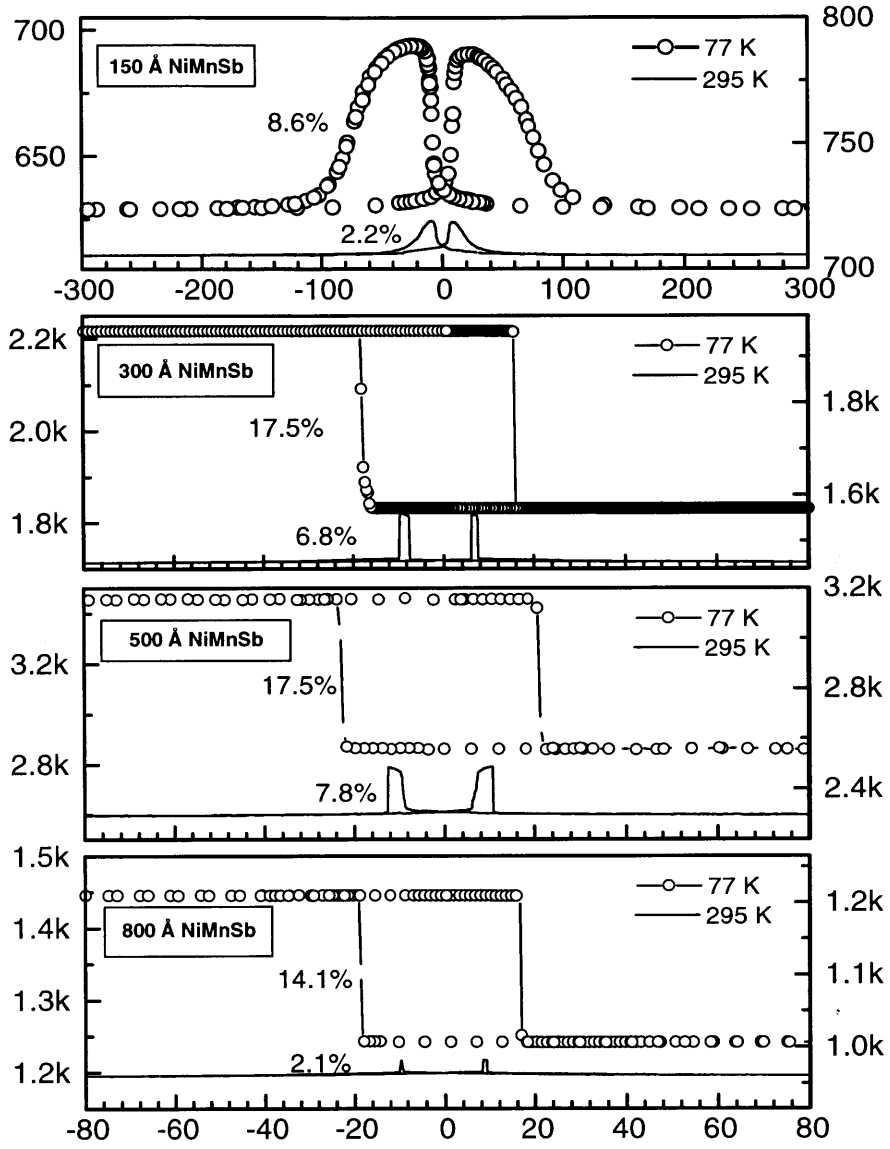

Figure 4.16: Magnetoresistance of NiMnSb/Al_2O_3/NiFe Junctions for different NiMnSb thickness. Left axes correspond to 77 K data, right to 295 K.

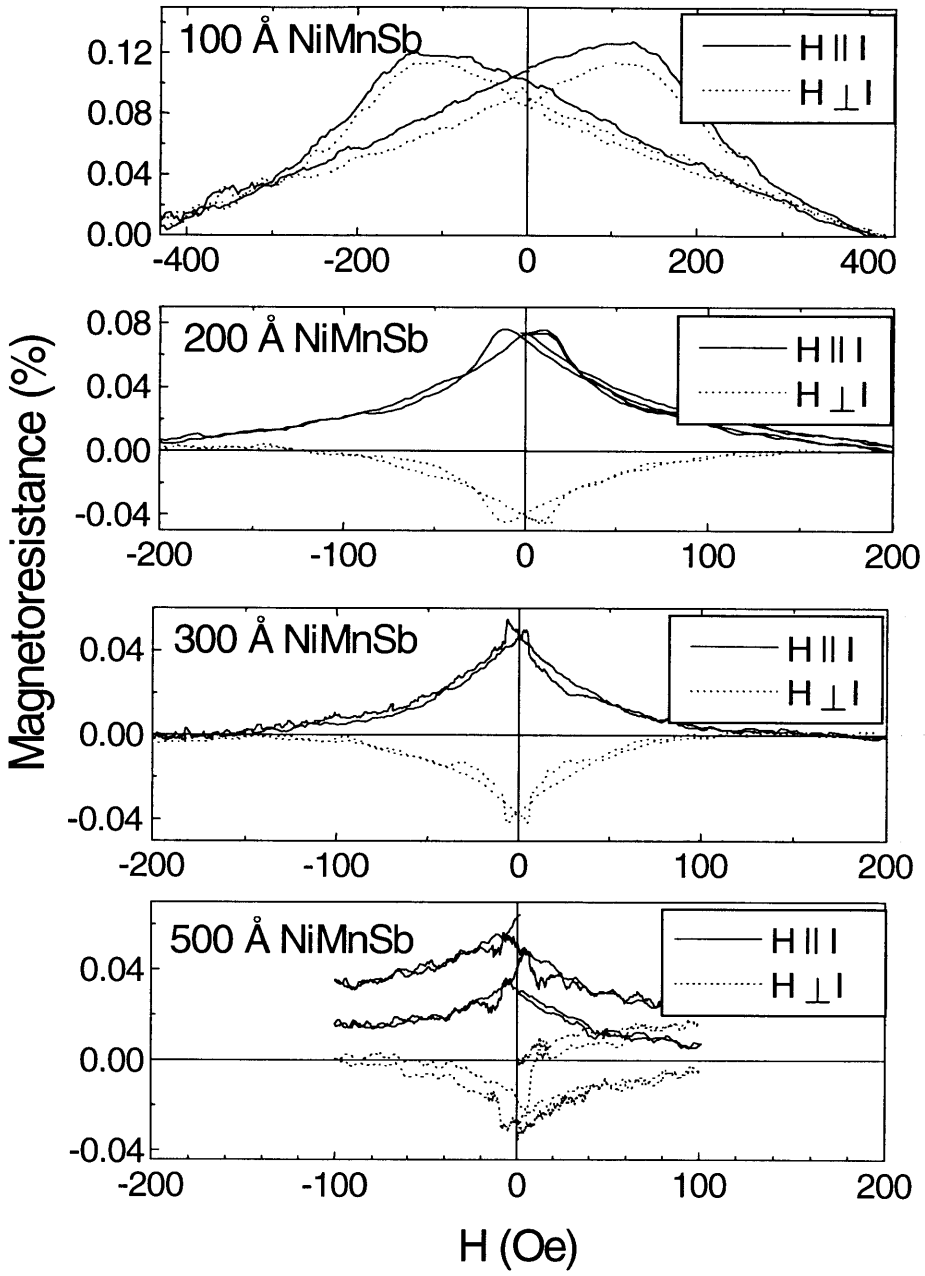

Figure 4.17 Magnetoresistance of NiMnSb electrodes for different film thickness.

observed in *polycrystalline* NiMnSb films [67]. Very high field is needed to saturate the MR, and, in fact, the MR continues to slope downward even up to 5 kOe. The origin of this MR is not entirely clear, but it is likely that the MR is dominated by some form of interfacial scattering. In contrast, the 200 Å and higher films show anisotropic MR (AMR), which is more typical for magnetic materials and results from the spin-orbit interaction. The magnitude of the AMR for the thicker films is very small, reflecting the low spin-orbit interaction in NiMnSb [67].

The above transport data suggest that the thinner films are of lower quality than the thicker films. To investigate this, AFM was performed on NiMnSb films of varying thicknesses, all grown at T_S=200°C with d_V=30 Å. The images, shown in Fig. 4.18, reveal that the 100 Å film shows a large number of pits at the surface. The measured dimensions of the pits are about 250 Å across and 40 Å deep. However, the size of the pits is close to the size of the AFM tip (~100 Å), so the measured depth may be lower than the actual depth. These pits are probably responsible for both the pinning of the NiMnSb domain walls, as well as the electron scattering evident in the MR of the films. Depending on the exact nature of the pits, they may also cause a reduction in the observed polarization, for example, if they extend down to the V seed layer. The number of pits decreases dramatically for the 200 Å film, coinciding with the observation of normal AMR and a much lower coercivity in the NiMnSb, and by 300 Å they disappear completely.

The films also become somewhat smoother as the film thickness increases. This can be explained by considering the strain relaxation mechanisms for the NiMnSb film. In other large misfit systems ($f \geq 0.012$), it has been observed that the film initially relaxes the strain energy by roughening, either by island formation or pit formation [68, 69]. These pits are regions of high

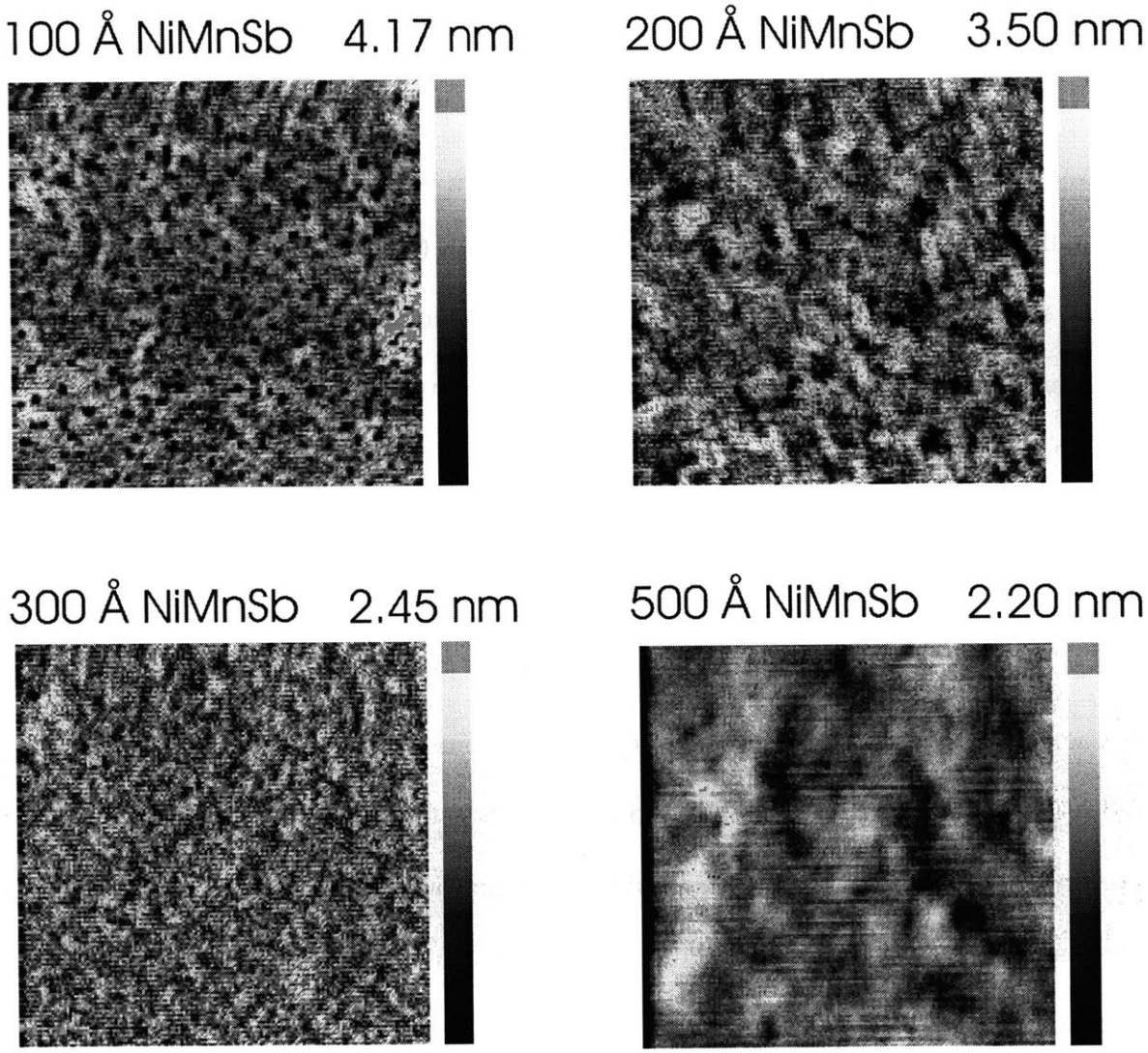

Figure 4.18: AFM images of NiMnSb Films of different thickness. Images are 1400 X 1400 nm

strain, and, thus, there is little barrier to dislocation nucleation at the pits. As the film continues to grow, relaxation occurs by the nucleation of dislocations at the pits, resulting in a general smoothening of the film for thicker films [68, 70]. A good estimate of the dislocation density can then be determined from the density of pits, which was found to be $1.3 \times 10^{10}/cm^2$.

It is thus apparent that NiMnSb film thicknesses of at least 300 Å are required in order to achieve optimum smooth films, free of pits.

4.6 Ultraviolet-Assisted Oxidation

One concern that arose in the plasma oxidized tunnel junctions was the possibility of damage arising from the presence of energetic oxygen ions in the plasma. These could lead to oxidation of the bottom FM electrode surface, as well as structural damage at the FM/I interface. This is of particular concern for NiMnSb, since the magnetic properties, as well as the half-metallicity, depend strongly on the crystal structure. A less energetic oxidation process is thus desirable. Natural oxidation in pure O_2 is one possibility which has been investigated recently [71]. However, the resistivity of the junctions achieved are invariably extremely low, which is problematic for the geometry used in this study. When the resistivity of the junction approaches that of the FM electrodes, nonuniform current flow in the electrodes in the junction area leads to spurious resistance measurements in the cross geometry used [72]. As a result, R_J of at least about 200 Ω is needed to avoid this problem. An alternative method of growing tunnel barriers was therefore attempted, namely ultraviolet (UV)-assisted oxidation. This method has been used to produce Al_2O_3 barriers for Josephson junctions [73] and relies on the chemical activity of ozone or atomic oxygen produced by UV light to oxidize the Al. Being a gentler oxidation

process than the plasma oxidation, this method would eliminate the possible structural damage by oxygen ion bombardment of the film surface and hopefully give improved control over the tunnel barrier growth.

The setup for the UV oxidation is shown in Fig. 4.19. A U-shaped 6 watt, mercury bulb was mounted in the load lock, 8.5 cm above the substrates. The oxidation parameters varied were the substrate temperature (T_{uv}), O_2 pressure (P_{ox}) and oxidation time. Most of the sample sets for this investigation were Co/Al_2O_3/NiFe junctions, which are comparatively easier to fabricate, since the oxidation parameters had to be determined from scratch. The prior work on UV oxidation [73] used 10 torr O_2 and 10 minute oxidation times at 295 K. This was found to be grossly insufficient to produce junction resistances in the necessary range in our setup. In fact, a number of runs were performed for P_{ox}=10-12 torr, and the oxidation efficiency was found to be much too low. P_{ox} was subsequently increased to 760 torr. Table 4.1 shows a summary of the sets made at this P_{ox}. One important fact that was noticed was that the UV illumination had a significant influence on the oxidation rate. Sets that were oxidized while not facing the UV bulb were always less than a few Ω and always lower resistance than the sets facing the bulb. Thus the time of oxidation was taken to be the time each set was actually facing the UV source.

The sets made with T_{uv} of 100°C show that a thickness (d_{Al}) of 14 Å Al is moderately over oxidized after 60 minutes. Set M110 for example has a relatively low barrier of 1.0 eV for the junctions with 14 Å Al oxidized for 60 min. M111 has an even lower barrier of 0.39 eV for the same conditions. The 14 Å Al oxidized for 120 min in M110 was grossly over-oxidized, which is reflected in enormous increase of resistance from being shorted at 295 K to a resistance of a few kΩ at 77 K. This is indicative of a semiconducting tunnel barrier, probably Co oxide at

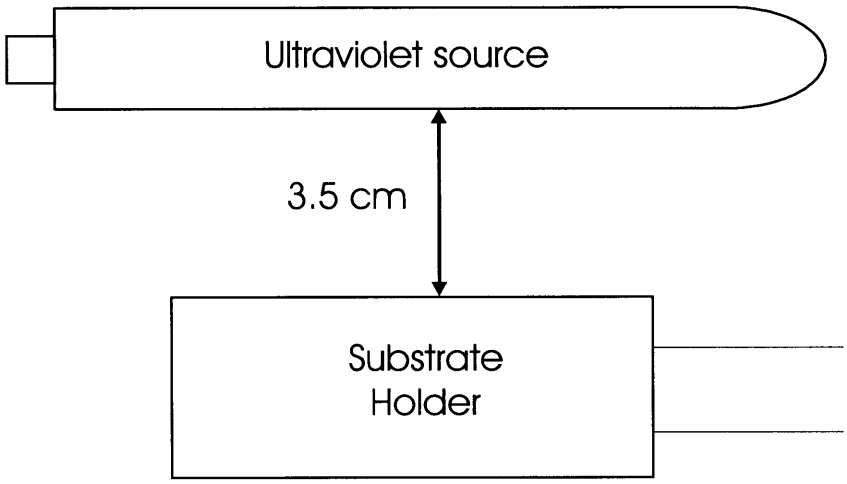

Figure 4.19: Ultraviolet-assisted oxidation setup.

Table 4.1 Summary of UV oxidation

Set	d_{Al}(Å)	t_{UV}(min)	T_{UV}(°C)	$R_{295\ K}$(kΩ)	$JMR_{295\ K}$(%)	ϕ(eV)
M110	14	60	100	3.6-5.1	7.6-8.4	1.0
	18	60	100	0.28-0.33	9.8-10.4	2.05
	14	120	100	Short (4.0 at 77 K)	0	----
	18	120	100	0.55-0.61	8.5-9	2.10
M111	14	60	100	7.0-11.0	0	0.39
	18	60	100	Short	0	----
M112	10	60	25	Short	0	----
	12	60	25	7.9-46.0	2.7-4.1	0.43
	14	60	25	0.060-0.093	12.7-14.8	----
	16	60	25	Short	0	----
M114	10	60	60	Short	0	----
	12	60	60		0	0.31
	14	60	60		0	0.34
	16	60	60	Short	0	----
M115	14	30	60	0.056-0.267	11.3-13.0	1.88
	16	30	60	Short	0	----
M116*	14	45	60	0.073-0.232	2.4-5.2	1.19
	16	45	60	0.115-0.280	2.0%	0.82

*NiMnSb/Al_2O_3/NiFe/CoO junction

the FM/I interface or Co diffusion into the barrier [14,63]. The 18 Å Al samples in M110 have relatively good tunneling properties, with high JMR and high barrier heights. However, oxidation at this high a temperature for such extended periods is rather undesirable due to the possibility of interdiffusion between the FM and the Al.

The set oxidized at room temperature (M112) shows that after 60 min, 12 Å Al is significantly over oxidized, while 14 Å is weakly oxidized, with resistances under 100 Ω. Increasing the temperature to 60°C (M114) results in heavy over-oxidation of both the 12 Å and 14 Å Al after 60 min. oxidation. The oxidation time was cut to 30 minutes for M115, which led to relatively good tunnel properties for the 14 Å sample, albeit with somewhat low R_J. The sole run with NiMnSb was M116, for which t_{uv} of 45 min. at T_{uv} of 60°C was used. The JMR for the best junction in this set is shown in Fig. 4.20 at 295 K and 77 K. The junction shows a significantly lower JMR of 12.0% at 77 K and 5.2% at 295 K, compared to the best plasma oxidized junctions, which showed 18.0 % and 9.0%, respectively. In addition, the I-V characteristics, shown in Fig. 4.21, reveal a somewhat lower quality tunnel barrier, with a barrier height of only 1.09 eV.

Some understanding of the UV oxidation process can be found by examining the general trend of the oxidation rate. It is well known that Al forms a self-limiting oxide, with the initial formation of 1-3 layers of Al_2O_3 occurring very rapidly. Subsequently, the oxidation rate virtually comes to a stop, since Al_2O_3 is a very good diffusion barrier. In order to form useful tunnel barriers for this study, this barrier to further Al oxidation must be overcome. From the UV oxidation data, it is clear that increasing both the temperature and the oxygen pressure increases the oxidation rate. These are consistent with an oxygen diffusion-limited mechanism. The theory for thermally-activated oxides in the thin-film regime was first put forward by Cabrera and Mott [74]. The proposed driving force for the oxidation was the electric field induced by negative oxygen ions on the outer surface of the oxide. This field causes either metal cations to migrate to the surface, or oxygen anions to the metal/insulator interface. The data in

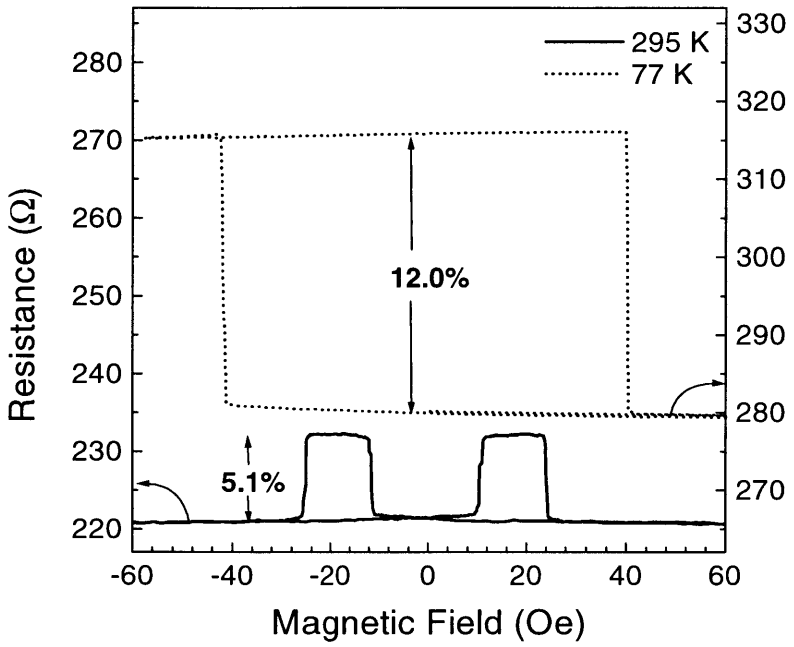

Figure 4.20: NiMnSb/Al_2O_3/NiFe/CoO junction with UV oxidized barrier.

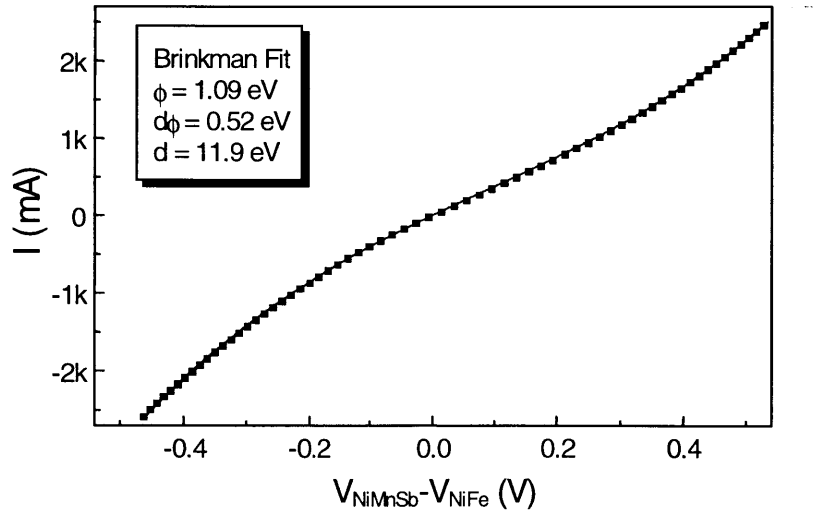

Figure 4.21: Current-voltage characteristics for NiMnSb/Al_2O_3/NiFe/CoO junction with UV oxidized barrier. Solid line shows the Brinkman fit through the data points.

this study supports the latter phenomenon. A corresponding electron flux from the metal is necessary to maintain charge neutrality, but this is not expected to be rate limiting, since clearly electrons can tunnel through the oxide in this regime. The picture of oxygen ion transport through the oxide has also been reported previously for Al oxidation [75]. The enhancement of oxidation rate by direct UV illumination suggests a possible mechanism for the enhancement. The UV radiation breaks O_2 bonds at the surface of the Al_2O_3, which increases the surface concentration of oxygen atoms. These are more readily ionized than molecular oxygen and, thus, can diffuse into the Al_2O_3 more easily. The rate of oxidation is therefore enhanced.

Although the tunnel junctions with NiMnSb showed lower JMR than the plasma oxidized barriers, the process, being a new approach, has not been optimized. Further study should lead to improvements in the tunnel junctions.

4.7 Point Contact Andreev Reflection

The spin-polarization of the NiMnSb films were also measured by a newly developed method, namely point contact Andreev reflection (PCAR), in collaboration with Dr. Robert Soulen's group at the Naval Research Lab [76]. This technique examines the transport across a metal-superconductor ballistic point contact in order to determine the spin-polarization of the metal. Transport at the metal-superconductor interface occurs by the conversion of normal current in the metal to supercurrent in the superconductor, a process which is called Andreev reflection [77] named after the theorist who explained the phenomenon. In order for this process to occur, the electron in the metal must be paired with an electron of opposite spin in order to form the electron pairs composing the supercurrent in the superconductor. This second electron

necessarily must come from the opposite spin band of the metal. As a result, a hole of opposite spin is back reflected from the metal-superconductor interface. The current across the contact is thus increased from the normal, non-superconducting state by the current from the Andreev reflected holes.

In a totally unpolarized metal (P=0), Andreev reflection proceeds unhindered, and the current is doubled from the normal state conductance. In contrast, in a half-metallic material, with P=100%, the process is totally suppressed, since there are no available spin down electrons at the Fermi energy to form the required electron pairs. These are depicted in Fig. 4.22. For the intermediate values of P, the current can be analyzed by adapting the Blonder-Tinkham-Klabwijk theory describing conventional (P=0) Andreev reflection [78]. The theory incorporates interfacial scattering by a scattering parameter (Z). In the ideal case, a ballistic point contact, Z=0, while the opposite extreme Z=∞, corresponds to a tunnel junction. This scattering acts to suppress Andreev reflection at low voltages, and its presence will be reflected at the gap edges of the superconducting gap by the conductance peaks characteristic of a tunnel junction. The following analysis assumes Z is negligible. The current can be decomposed into separate unpolarized and fully polarized components:

$$I = I_{\uparrow} + I_{\downarrow} = 2I_{\downarrow} + (I_{\uparrow} - I_{\downarrow}) = I_{unpol} + I_{pol}, \qquad (4.1)$$

with unpolarized, $I_{unpol,}$ current obeying conventional BTK theory, and the polarized current, I_{pol}, making no contribution to the supercurrent. The polarization can be determined from the differential conductance, dI/dV:

$$\frac{dI}{dV} = (1 - P_C)\frac{dI_{unpol}}{dV} + P_C \frac{dI_{pol}}{dV}. \qquad (4.2)$$

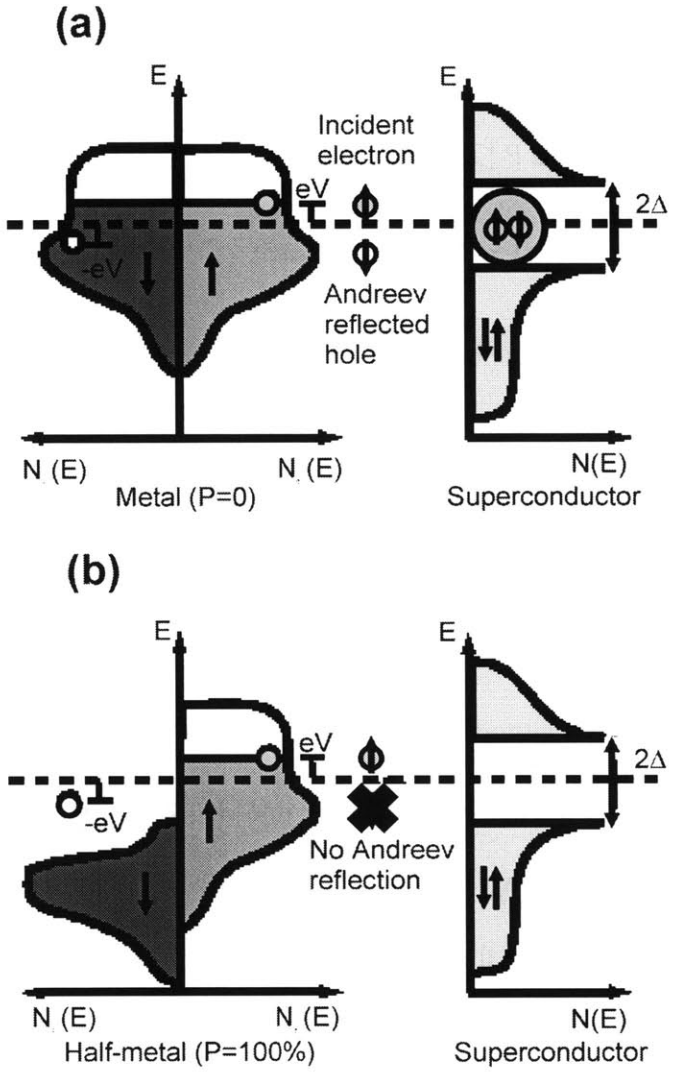

Figure 4.22 Andreev reflection between metal and superconductor. (a) P = 0% (b) P=100%

With minimal interfacial scattering and for eV <<Δ and k_BT<<Δ, where 2Δ is the uperconducting energy gap,

$$\frac{1}{G_n}\frac{dI_{unpol}}{dV} = 2, \text{ and } \frac{dI_{pol}}{dV} = 0,. \qquad (4.3)$$

Then the equation for dI/dV and P [79] becomes:

$$\frac{1}{G_n}\frac{dI}{dV}_{(eV\to 0, T\to 0, Z\to 0)} = 2(1-P). \qquad (4.4)$$

Measurements were conducted using superconducting rods of Nb or Ta sharpened to a point by mechanical polishing. Scanning electron microscopy showed that the point of the rod was conical with a rounded end with radius of approximately 100 μm. Protrusions at the end of about 1 μm were also present which probably made the actual contact with the film. The rod was positioned by a micrometer mechanism, and transport measurements were performed using a conventional four-terminal method. The analysis was performed on only the data for point contacts with ohmic contact resistance between 1-100 Ω and exhibiting small interfacial scattering. The dI/dV data is shown in Fig. 4.23 for NiMnSb, as well as a few other materials for comparison. The polarization was then calculated from Eqn. 4.4. The data is tabulated in Table 4.2 for a variety of materials studied, along with P derived from tunneling measurements, where available. As a consistency check, data was also collected using a Fe sharpened point into a superconducting Ta or V base layer to make the point contact. The NiMnSb shows a polarization of 58%, higher than the polarization from spin tunneling, but still less than the predicted 100%. In fact, the predicted half-metals NiMnSb, LSMO and CrO_2 show larger polarization than conventional ferromagnets. However, the difference is rather modest in

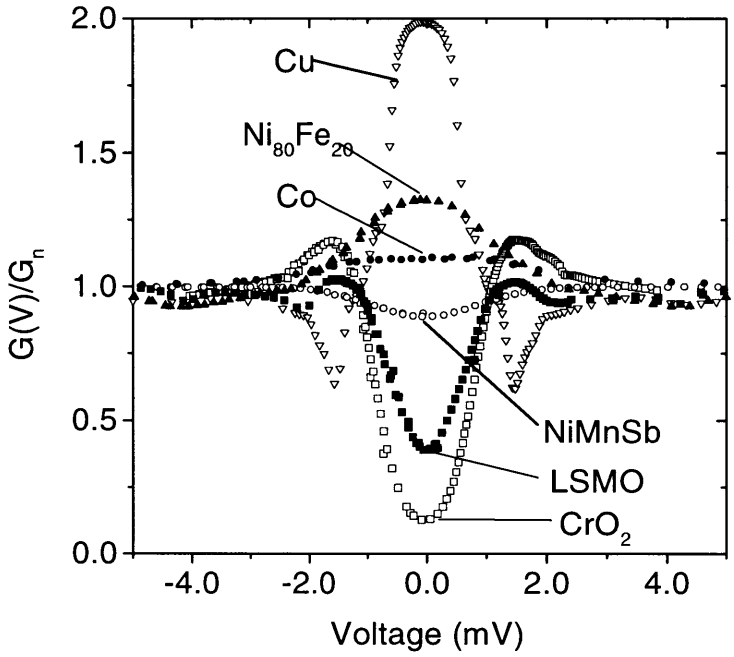

Figure 4.23: Differential conductance for metal-superconductor contacts. Andreev reflection at low voltages becomes increasingly suppressed with increasing spin-polarization.

Ferromagnet	Point	Base	P (SPT)	P (PCAR)
$Ni_{80}Fe_{20}$	Nb	$Ni_{80}Fe_{20}$ film	45%	37% ± 5
Co	Nb	Co foil	45%	42%± 2
Fe	Nb	Fe film	41%	42% ± 2
	Ta	Fe film		45% ± 2
	Fe	Ta foil		46 ± 2
	Fe	V crystal		45 ± 2
Ni	Nb		27%	43% ± 2
	Ta			44% ± 4
NiMnSb	Nb		28%	58% ± 2.3
LSMO	Nb		---	78% ± 4.0
CrO_2	Nb		---	90% ± 3.6

Table 4.2: Spin-polarization data from point contact Andreev reflection [76]. Data from spin-polarized tunneling (SPT) [14] also included for comparison, where available.

NiMnSb. LSMO and CrO_2 show substantially larger polarization, of 78% and 90% respectively. Comparing the PCAR data to the tunneling data for other materials shows reasonably good correspondence between the two methods, with the notable exception of Ni. The discrepancy in the Ni is probably because the value of P obtained by tunneling for Ni is very sensitive to impurities at the FM/I interface, more so than other materials studied [4].

Chapter 5: Conclusions and Further Studies

The spin-polarization measured in this work by spin dependent tunneling is clearly significantly lower than the expected 100%. It is useful to consider some possible sources for this discrepancy. An important thing to note is that the calculation of the band structure which predicted half-metallicity assumed a perfect $C1_b$ lattice. Consequently, any deviations from perfection at the surface of the NiMnSb could have a dramatic influence on the real band structure of the NiMnSb films.

Some common defects in thin films are planar defects such as grain boundaries. The influence of these can be estimated by simply considering the fraction of the surface area that are affected by these defects. For planar defects, as a conservative estimate, we can assume the affected areas are totally unpolarized (P=0). The current will then be made up of an unpolarized contribution from the grain boundaries themselves, and a fully spin-polarized contribution from the rest of the film. This is depicted as shown in Fig. 5.1, assuming a spherical grain. If we assume the current density is equal for the polarized and unpolarized regions, the normalized spin up current and spin down currents are then given by

$$I_\uparrow / I_0 = (1 - A_{unpol}) + A_{unpol}/2 \qquad (5.1) \qquad I_\downarrow / I_0 = A_{unpol}/2 \qquad (5.2)$$

where A_{unpol} is the fractional area of the unpolarized regions and I_0 is the total current. The measured polarization of the tunnel current is then given by

$$P = \frac{I_\uparrow - I_\downarrow}{I_\uparrow + I_\downarrow} = 1 - A_{unpol} \qquad (5.3)$$

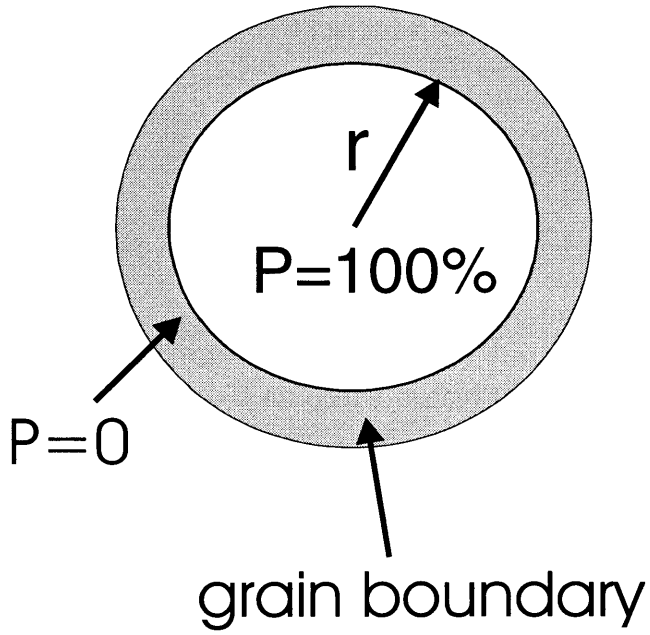

Figure 5.1: Planar defect at NiMnSb surface

We can estimate the reduction due to grain boundaries by a simple calculation of the area of boundaries. From the AFM image for the 500 Å sample in 4.18, the approximate minimum grain size is 2000 Å, based on the morphological features present in the image. The grain boundary width is expected to be about 10 Å. The fractional area of grain boundaries is then $(\pi r_2^2 - \pi r_1^2)/ \pi r_2^2$, where r_2 is 1010 Å and r_1 is 1000 Å. Grain boundaries thus make up approximately 2% of the surface area and thus cannot be expected to lead to a significant decline in polarization. In fact to get a decline of polarization to 50% requires a grain size of about 50 Å, which is unrealistically small. Other planar defects, such as twin boundaries and antiphase boundaries are possible as well. Although they were not explicity imaged, we can get some idea about the prominence of these defects from other measurements. For example, the x-ray diffraction measurements showed no evidence of twinning, so the twin boundaries can be excluded. Also, antiphase boundaries are unlikely to play a significant role, since these typically lead to pinning of domain wall motion [80], while the NiMnSb films above 300 Å thickness showed low coercivities and sharp magnetization reversal. In fact, in CuMnAl, a Heusler alloy with a similar structure as NiMnSb, this pinning at antiphase boundaries was directly observed by Lorentz microscopy [81]. We therefore conclude that planar defects are unlikely to play a direct role in reducing the spin-polarization of the NiMnSb. They can, however, influence junction characteristics by adding to the roughness of the films, which affects the subsequent tunnel barrier formation.

Another possible defect at the surface of thin films is a threading dislocation, which distorts the unit cell in its immediate vicinity. The influence on the polarization can be estimated by the extent of the strain field around a dislocation. The minority spin energy gap in NiMnSb is

expected to persist for a lattice constant between 5.87 Å and 6.09 Å, and ferromagnetism to persist to 5.77 Å [60]. The experimental lattice constant was 5.92 Å from Table 3.1. Thus, a strain (ε) of about 0.01 is needed to close the energy gap and start to introduce minority spin electrons, while a strain of about 0.03 is needed to reach the paramagnetic state. The strain around the dislocation can be approximated by $\varepsilon = b/r$, where b is the magnitude of the burgers vector and r is the distance from the dislocation [82]. Take b to be about a lattice spacing, or $6x10^{-8}$ cm. Then the threshold radius (r_{th}), for half-metallicity is ε is b/0.01, or $6x10^{-6}$ cm. The threshold for ferromagnetism (r_f) is b/0.03 or $2x10^{-6}$ cm. As a first approximation, the polarization can be estimated to follow a linear relationship between these two radii from 100% to 0%. This is shown schematically in Fig. 5.2. The region in the immediate vicinity of the dislocation is highly strained and modeled as an unpolarized paramagnetic region. Then just outside r_f, $P=P(r)=100\%(r-r_f)/(r_{th}-r_f)$. The spin up current and spin down currents around the dislocation become

$$I_{\uparrow} / I_0 = \pi r_f^{\,2} / 2 + \int_{r_f}^{r_{th}} 2\pi r \left(\frac{1+P(r)}{2} \right) dr \qquad (5.4)$$

$$I_{\downarrow} / I_0 = \pi r_f^{\,2} / 2 + \int_{r_f}^{r_{th}} 2\pi r \left(\frac{1-P(r)}{2} \right) dr \qquad (5.5)$$

Evaluating the spin-polarization around a dislocation (P_{dis}) yields a value of 52%. The net surface spin-polarization of the NiMnSb can be calculated assuming various values of dislocation density (ρ). For $\rho=10^8/cm^2$ and $10^9/cm^2$ for example, the P is expected to be 99.5% and 95%, respectively. For larger dislocation densities ($\sim 10^{10}/cm^2$), the strain fields of adjacent

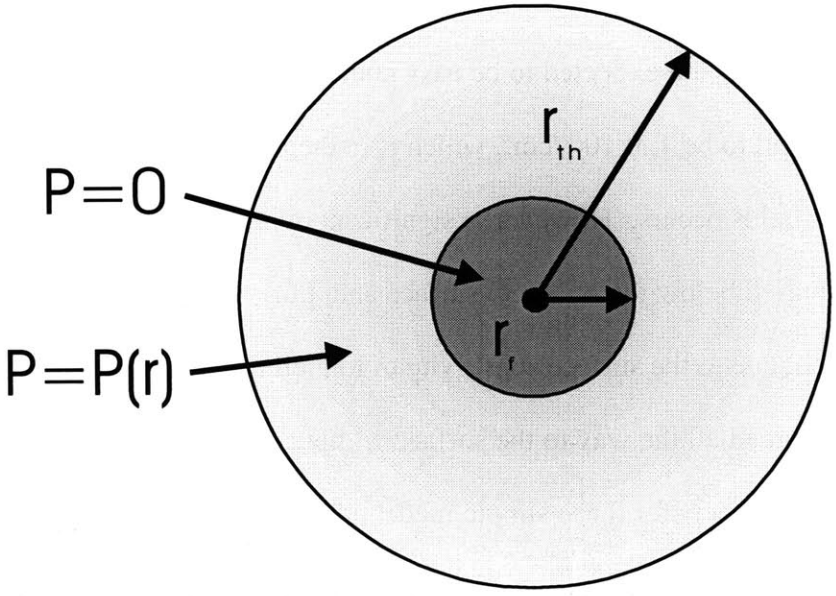

.Figure 5.2: Model of polarization around a threading dislocation.

dislocations begin to overlap, and these assumptions break down. At the onset of this overlap (r_{dis}=7x10^9/cm^2), the P is reduced to 62%. We can get an upper limit on the density of threading dislocations from the density of pits seen for the 100 Å NiMnSb films in Fig. 4.18. As mentioned earlier, these pits are expected to be easy nucleation sites for dislocations. The density of pits was found to be 1.3x10^{10}/cm^2, which is in the regime where significant overlap of the dislocation strain fields occurs. However, a significant number of these dislocations are expected to remain buried below the NiMnSb surface and, thus, would not influence the measured polarization, due to the surface sensitivity of tunneling. It is difficult to say how many of these dislocations thread all the way to the surface without actual TEM images, for instance. In addition, the actual numbers for these simple model calculations cannot be taken too seriously. Nevertheless, it is apparent that dislocations cannot be excluded from consideration when trying to determine possible reasons for the reduced values of P measured. For high threading dislocation density, the NiMnSb surface can be highly strained and can deviate significantly from the structure of the half-metallic state.

It is also necessary to consider atomic level disorder, or disorder in the arrangement of the atoms in the NiMnSb unit cell. Figure 5.3 shows the $C1_b$ structure with the four available sites for the atoms. Recall that, ideally for NiMnSb, A is occupied by Ni, B by Mn, D by Sb and C is empty. Recent calculations were performed by D. Orgassa *et al.* [83] which introduced different kinds of disorder into the NiMnSb unit cell and calculating the resulting band structure. These showed that it takes only very modest amounts of disorder to close the energy gap and reduce the polarization. Three types of disorder were considered, all primarily involving the Mn site, as the Mn is responsible for virtually the full moment of the NiMnSb, as well as the opening

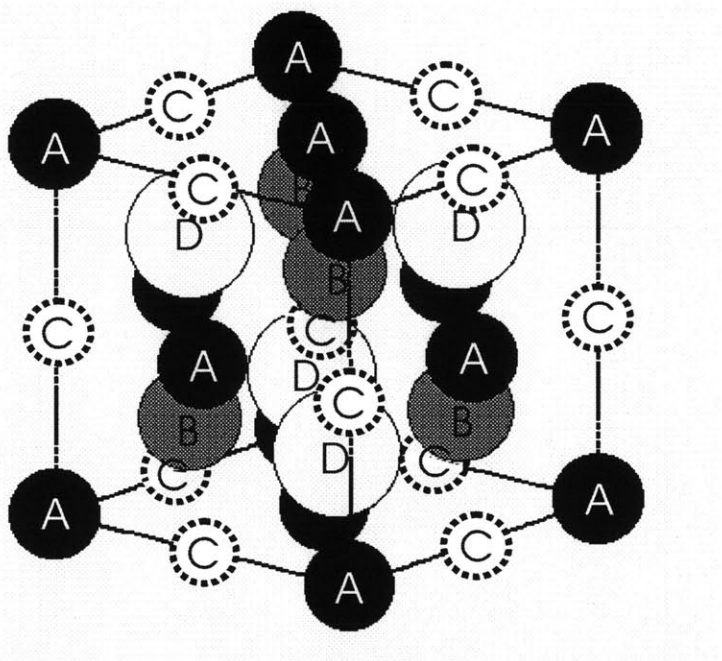

Figure 5.3: General Heusler alloy unit cell. For C1b NiMnSb, Ni is at site A, Mn at site B, Sb at site D, and site C is empty.

Table 5.1 Types of disorder considered in [83]

Disorder type	Scheme	Site A	Site B	Site C	Site D
A-B	A↔B	$Ni_{1-x}Mn_x$	Ni_xMn_{1-x}		Sb
C	AB↔C	Ni_{1-x}	Mn_{1-x}	Ni_xMn_x	Sb
C'	BD↔C	Ni	Mn_{1-x}	Mn_xSb_x	Sb_{1-x}

Table 5.2 Total spin-polarization (P) and s-electron polarization (P_s) calculated in [83]

Disorder type	Level (%)	P(%)	P_s(%)
A-B	5	52	82
	10	29	64
C	5	67	89
	10	31	60
C'	5	24	34
	10	10	19

of the minority spin energy gap [1]. Table 5.1 summarizes the types of disorder considered. Orgassa *et al.* found that between 1% and 5% disorder was enough to introduce minority spin states at the Fermi level (E_F). Calculations on the spin-polarization at E_F showed that P decreased with increasing disorder (Table 5.2). Orgassa noted that the relevant P is probably the P of the s-electrons (P_s), since the tunneling electrons are expected to be primarily s-character [3,16]. However, holes in the Sb band are responsible for conduction in NiMnSb [1,84], and the

relevant electrons for tunneling in the disordered NiMnSb may be some combination of the s and p electrons.

In considering the possible types of disorder, it is also important to recall that the loss of half-metallicity is expected to be accompanied by a change in the magnetic moment of the NiMnSb from the ideal value of 4 μ_B. The decrease in moment was found to vary with the type of disorder [85]. The A-B type disorder, for example, shows a substantial drop to 3.5 μ_B at 5% disorder. At this level of disorder, 82% of P_s is maintained, and thus it is unlikely that this type of disorder is present in the bulk. In comparison, type C and C' show decreases in moment of 3.7 and 3.8 μ_B at 5% disorder. The C type disorder maintains a substantial amount of the s-polarization (89%) at this level of disorder, and also can also be virtually ruled out. The C' disorder, in contrast, shows a very steep decline in polarization with only a weak loss of magnetic moment. It is thus the type of atomic disorder that is most likely to cause such a decreased P. Kautzky et al. found exactly this type of disorder in sputter deposited films of PtMnSb [86] and also NiMnSb [87]. Disorder of about 10% was estimated for those films by structure factor analysis of x-ray diffraction data. However, according to the authors, the composition of the film itself was off-stoichiometry at almost this level, as determined by Rutherford back scattering (RBS). In contrast, RBS measurements on films in this study showed stoichiometric NiMnSb. EXAFS analysis is under way which may resolve the question of disorder in these films.

It is also important that one does not lose sight of the most fundamental limitation of spin dependent tunneling, namely the extreme surface sensitivity of the phenomenon. This gives the technique special relevance when it comes to application potential of a material for

magnetoelectronics, but can also lead to problems. One of the most notable materials in which these problems with the surfaces and interfaces arise is elemental nickel. It is still unclear whether the ultimate value of polarization has been reached for Ni, even after 20+ years of study on seemingly such a simple material [88]. It is thus most critical to examine the surface and interfacial phenomena for NiMnSb tunnel junctions. The fact that the point contact Andreev reflection measured a substantially larger spin-polarization points to the problem in the tunnel junctions being one related to the FM/I interface. One potential problem is oxidation of the underlying FM electrode. Examination of the properties of $Co/Al_2O_3/NiFe$ junctions with increasing oxidation time suggest that some degree of oxidation of the Co occurs before completion of the Al oxidation [14]. Given the small amount of surface roughness, and the resulting inhomogeneity of the tunnel barrier, this is not altogether surprising. Junctions with Co as the bottom electrode are apparently somewhat insensitive to this oxidation, as magnetoresistance values close to those expected from Julliere's model can be achieved. In contrast, NiMnSb junctions are expected to be very sensitive to oxidation, since the most likely oxide to form is Mn oxide. This can be detrimental for two reasons. First, spin-scattering of the tunneling electron spins can occur, which is commonly observed in overoxidized $Co/Al_2O_3/NiFe$ junctions. Secondly, the formation of the Mn oxide effectively depletes the NiMnSb of Mn. This is a serious concern, given that Mn is the atom which carries most of the moment and is responsible for the opening of the minority spin gap,.

Other open questions regarding the NiMnSb film itself also exist. For example, the surface structure of the NiMnSb has not been examined. Recently, RHEED experiments on (111) NiMnSb and PtMnSb films observed $C1_b$ structure at the surface [89]. In some cases,

surface reconstruction was found, but the reconstruction could be removed by deposition of 2 Å Al. No information is available for (001) NiMnSb films, however. The other major remaining question is the degree of atomic disorder in the NiMnSb films, especially at the surface. The PCAR data suggest that the problem is not entirely related to the FM/I surface, as the P observed is still significantly less than 100%. The lower P could reflect, for example, atomic disorder in the bulk or damage to the NiMnSb structure in the vicinity of the tip.

In regards to improving the polarization of the NiMnSb tunnel junctions, it seems very difficult to achieve truly perfect FM/I interfaces using the current techniques for producing tunnel barriers. The Å-level inhomogeneities will almost certainly mean unoxidized Al in some places and Mn oxide in others, both of which are detrimental to the spin-polarization. One simple idea is to deposit an ultra-thin layer of Mn on top of the NiMnSb before the Al deposition. This at least prevents the loss of Mn from the NiMnSb itself, and then the loss of polarization will be primarily from the spin-scattering due to the Mn oxide. A somewhat similar idea was used by the author which resulted in a slight improvement in the JMR of polycrystalline NiMnSb junctions (Appendix A) [46]. In that case, additional Mn was incorporated into the bulk of the films, since the level of vacuum was only 10^{-7} torr, where oxidation is more likely. However, although this idea may improve the polarization, it is unlikely that the full polarization will be observed. A more promising method would be to use MBE grown tunnel barriers. The structure of NiMnSb is such that a number of candidate tunnel barrier materials exist. The $C1_b$ structure is essentially identical to the fluorites (CaF_2, SrF_2, etc.), making them one possibility. Another promising class of materials are the wide gap III-V (e.g. AlAs/AlSb) semiconductors since NiMnSb closely resembles the zincblende structure. A major advantage of these materials

is the ability to engineer the lattice constant to precisely match NiMnSb. A great wealth of prior work is also available concerning the growth of these materials. A potential problem might be leakage due to the relatively low energy gap in these semiconductors, compared to true insulators. However, one expects that as long as spin conservation holds and the current is perpendicular to the planes of the FM/I interfaces, a large JMR should be observed [38]. There remain theoretical questions also as to whether the minority spin energy gap persists to the surface of NiMnSb, as well as how the tunnel barrier material affects the band structure at the FM/I interface. The actual termination plane may also play a role, *e.g.*, in the (001) direction, two different possibilities exist for NiMnSb, a plane of Ni atoms or a plane of Mn and Sb atoms.

It should be pointed out that the growth method presented here allows a number of other Heusler alloys to be investigated, some of which are also predicted to be half-metallic in the $C1_b$ structure. Figure 5.4 shows the x-ray diffraction patterns for CoMnSb and PtMnSb films grown at T_S=200°C and 30 Å V seed layer. As is the case for NiMnSb, good epitaxial (001) films are evident for these materials. As mentioned earlier, PtMnSb is also half-metallic [1, 60], and calculations on CoMnSb also predict half-metallicity in the $C1_b$ state [90]. However, bulk CoMnSb is known to deviate from the $C1_b$ structure, with Co and Sb atoms displaced from their positions in the $C1_b$ unit cell [91].

In regards to magnetoelectronics applications for NiMnSb, a number of other work has demonstrated the potential for patterning films of NiMnSb using both wet and plasma etching techniques [92]. In addition, MgO (001), the substrate material in this work, has been grown on Si (001) wafers by laser ablation [93] and evaporation [94]. Therefore, in principle, NiMnSb devices could be fabricated using existing Si process technology. However, in order for there to

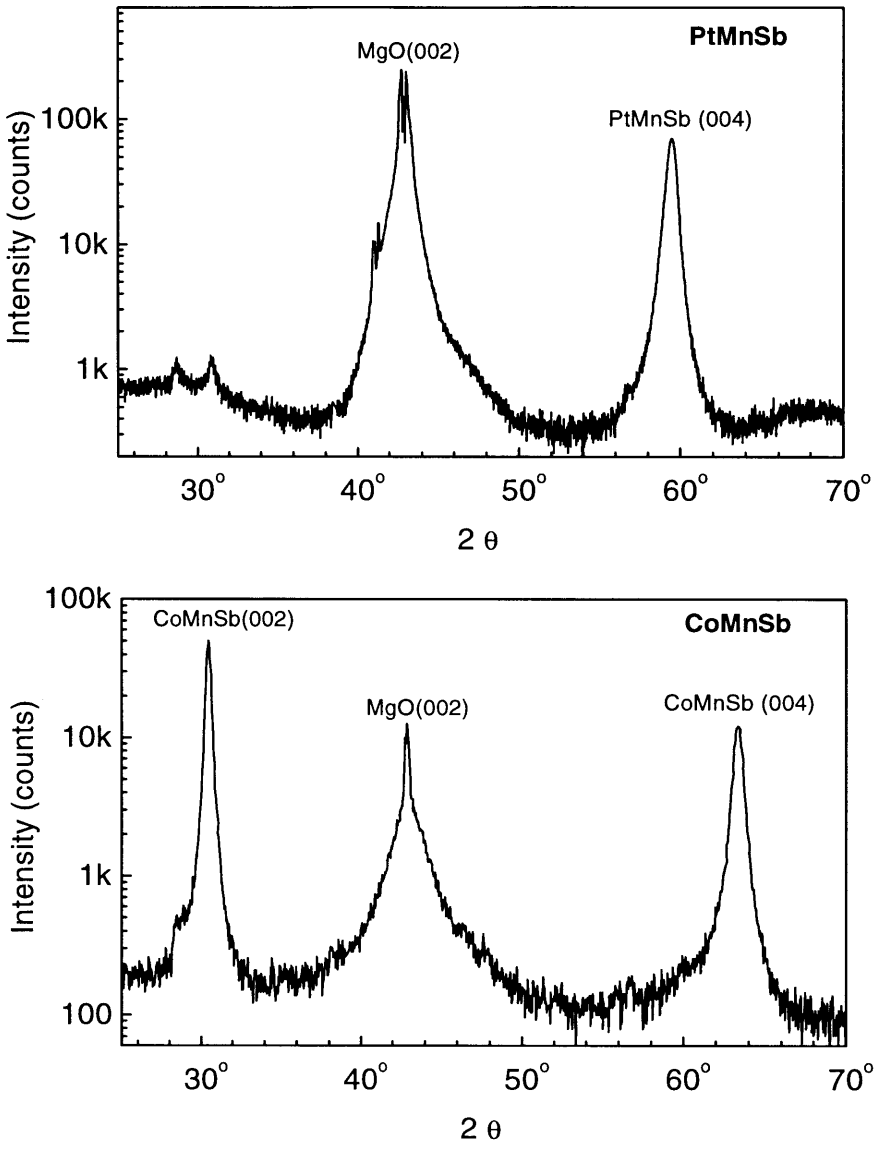

Figure 5.4: X-ray diffraction patterns for PtMnSb and CoMnSb. Films are grown using identical parameters as in NiMnSb, i.e., T_S=200°C, d_V=30 Å.

be a significant impetus to do so, it must first be demonstrated that NiMnSb offers a substantial advantage over existing ferromagnetic materials, *i.e.*, that it indeed has 100% spin-polarized electrons. Thus, it is important for continued work in fabricating NiMnSb spin dependent tunnel junctions, focussed particularly on achieving an ideal FM/I interface.

In conclusion, significant progress has been made in the fabrication of spin dependent tunnel junctions with the predicted half-metallic ferromagnet NiMnSb. The spin-polarization was found to be 28%, significantly lower than the predicted 100%, but substantially higher than indicated in previous attempts to fabricate NiMnSb magnetoelectronic devices [44-46]. In addition, the ability to grow epitaxial NiMnSb films has been demonstrated at reduced temperatures, which allows a wide variety of the related Heusler alloys (PtMnSb, CoMnSb, PdMnSb, etc.) to be investigated.

Appendix A: Ferromagnet/Insulator/Ferromagnet Junctions with Polycrystalline NiMnSb

Our prior work focussed on polycrystalline NiMnSb films grown on glass substrates. A 30 Å Mn seed layer was used to improve film adhesion and reduce its surface roughness. Films of 300 Å NiMnSb were deposited by co-evaporation in 10^{-7} torr vacuum on the Mn layer with a substrate temperature of 400°C. The x-ray diffraction, shown in Figure A.1, shows polycrystalline $C1_b$ NiMnSb. Subsequently, tunnel junctions of NiMnSb/Al_2O_3/NiFe were fabricated. The typical behavior of such a junction is shown in Figure A.2. At room temperature (RT) the JMR peaks are very sharp, indicating that the coercivities of the two FMs are close to each other. Thus, full antiparallel orientation is not achieved at the peaks, and the JMR is only 2.4%. At 77 K, however, the peaks are very broad, indicating well separated coercivities. The JMR increased significantly to 7.0%. At this level of vacuum and at the elevated substrate temperature, some oxidation of Mn may occur, which would detrimental to the polarization, as this depletes the NiMnSb of the element responsible for most of its magnetization. Addition of 10% more Mn to the films, i.e., $NiMn_{1.1}Sb$, resulting in a slight improvement of the JMR to 8.1% at 77 K, while the best JMR for stoichiometric NiMnSb was only 6.1%. Further increase of Mn concentration to $NiMn_{1.2}Sb$ resulted in a modest decline in JMR to 7.5% at 77 K. These suggest that Mn oxidation may indeed be a problem. Determination of the spin-polarization of these NiMnSb films, based on Julliere's formula reveals a polarization of only 10%.

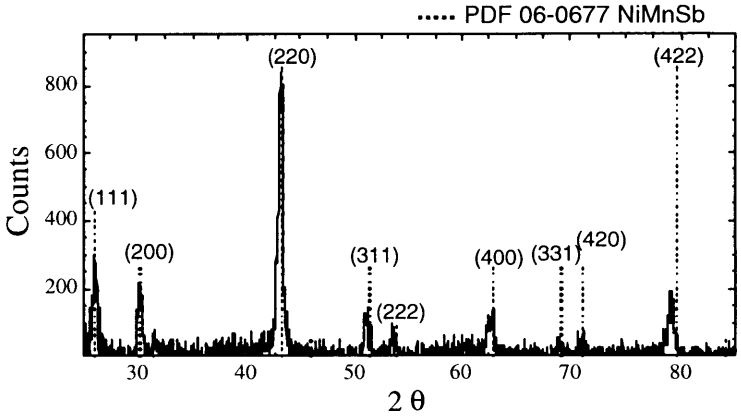

Figure A.1: X-ray diffraction for polycrystalline NiMnSb film.

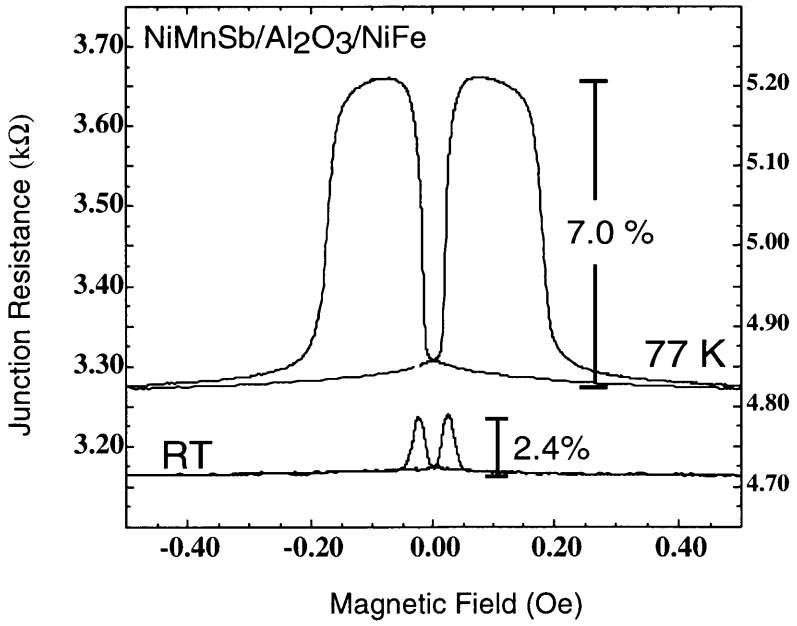

Figure A.2: Magnetoresistance of polycrystalline NiMnSb/Al_2O_3/NiFe tunnel junction

References

[1] R. A. de Groot F. M. Mueller, P. G. van Engen, and K. H. J. Buschow, Phys. Rev. Lett. **50**, 2024 (1983).

[2] W. F. Brinkman, R. C. Dynes and J. M. Rowell, J. Appl. Phys., **41**, 1915.

[3] E. L. Wolf, Principles of Electron Tunneling Spectroscopy (Clarendon Press, Oxford, 1985).

[4] R. Meservey and P. M. Tedrow, Physics Reports, **238**, 173 (1994).

[5] I. Giaever, Phys. Rev. Lett., **5**, 147, 464 (1960).

[6] J. Bardeen, L. N. Cooper and J. R. Schrieffer, Phys. Rev., **108**, 1175 (1957)

[7] R. Meservey, P. M. Tedrow and P. Fulde, Phys. Rev. Lett., **25**, 1270 (1970).

[8] P.M. Tedrow and R. Meservey, Phys. Lett. **58A**, 237 (1978).

[9] P.M. Tedrow and R. Meservey, Phys. Letters **51A**, 57 (1975); R. Meservey, P.M. Tedrow and R.C. Bruno, Phys. Rev. B **17**, 2815(1978); G. Gibson, P.M. Tedrow and R. Meservey, Phys. Rev. B **40**, 137 (1989).

[10] P.M. Tedrow and R. Meservey, Solid State Comm. **27**, 1397 (1978). Phys. Lett. A **69**, 285 (1978).

[11] A. A. Abrikosov and L. P. Gor'kov, Zh. Eksp. Teor. Fiz, **42**, 1088 (1962); Sov. Phys. JETP, 15 (1962).

[12] L. Hodges, H. Ehrenreich and N.D. Lang, Phys. Rev. **152**, 505 (1966).

[13] P. M. Tedrow and R. Meservey, Phys. Rev B, **7**, 318 (1973).

[14] R.J.M. van de Veerdonk, Ph.D. thesis, Eindhoven University of Technology (1999).

[15] R. Meservey,. *Inelastic Electron Tunneling Specroscopy* (ed. T. Wolfram), p 230 (1978).

[16] J. A. Hertz and K. Aoi, Phys. Rev. B, **8**, 3252 (1973).

[17] J. –N. Chazalviel and Y. Yafet, Phys. Rev. B, **15**, 1062 (1977).

[18] M. B. Stearns, J. Magn. Magn. Mater., **5**, 167 (1977).

[19] R. Meservey, D. Paraskevopoulos and P.M Tedrow, Phys. Rev. B, **22**, 1331 (1980).

[20] M. Julliere, Phys. Lett., **54A**, 225 (1975).

[21] R. Meservey, P. M. Tedrow and J. S. Brooks, J. Apply. Phys., **53**, 1563 (1982); G. A. Gibson and R. Meservey, J. Appl. Phys., **58**, 1584 (1985).

[22] Y. Suezawa and Y. Gondo, J. Magn. Magn. Mater., **126**, 524 (1993)

[23] T. Miyazaki, T. Yaoi and S. Ishio, J. Magn. Magn. Mater., **98** L7 (1991); J. Magn. Magn. Mater., **126**, 430 (1993).

[24] J. Nowak and J. Rauluskiewicz, J. Magn. Magn. Mater., **109**, 79 (1992).

[25] Y. Suezawa, F. Takahashi and Y. Gondo, Jap. J. Appl. Phys., **31**, L1451 (1992).

[26] R. Meservey, P. M. Tedrow and V. R. Kalvey, Solid State Commun., **36**, 969 (1980); J. Appl. Phys. , **52**, 1617 (1981).

[27] J. S. Moodera and R. Meservey, Phys. Rev. B, **29**, 2943 (1984).

[28] J. S. Moodera, L. R. Kinder, T. M. Wong and R. Meservey, Phys. Rev. Lett., **74**, 3273 (1995).

[29] J. S. Moodera, J. Nowak and R. J. M. van de Veerdonk, Phys. Rev. Lett., **80**, 2941 (1998).

[30] C.H. Shang, J. Nowak, R. Jansen and J.S. Moodera, Phys. Rev. B, **58**, R2197 (1998).

[31] D.T. Pierce, R.J. Celotta, J.Unguris and H.C. Siegmann, Phys. Rev. B **26**, 2566 (1982); D. Mauri, D. Scholl, H.C. Siegmann and E. Kay, Phys. Rev. Lett. **61**, 758 (1988).

[32] D. Scholl, M. Donath, D. Mauri, E. Kay, J. Mathon, R.B. Muniz and H.C. Siegmann, Phys. Rev. B **43**, 13309 (1991).

[33] D.L. Mills and A.A. Maradudin, J. Phys. Chem. Solids **28**, 1855 (1967); J. Mathon and S. B. Ahmad, Phys. Rev. B **37**,660 (1988).

[34] A. M. Bratkovsky, Appl. Phys. Lett., **72**, 2334 (1998).

[35] J.S. Moodera, unpublished results.

[36] K. Schwarz, J. Phys. F: Metal Phys. **16**, L211 (1986).

[37] J.-H. Park, E. Vescovo, H.-J. Kim, C. Kwon, R. Ramesh and T. Venkatesan, Nature, **392**, 794 (1998).

[38] A.M. Bratkovsky, Phys. Rev. B, **56**, 2344 (1997).

[39] J. Z. Sun, L. Krusin-Elbaum, P. R. Duncombe, A. Gupta and R. B. Leibowwitz, Appl. Phys. Lett., **70**, 1769 (1997).

[40] K.P. Kämper, W. Schmitt, G. Güntherodt, R.J. Gambin and R. Ruf, Phys. Rev. Lett. **59**, 2788 (1988)

[41] J. S. Moodera and D. M. Mootoo, J. Appl. Phys., **76**, 6101 (1994).

[42] K. E. H. M. Hanssen, P. E. Mijnarends and L. P. L. M. Rabou, Phys. Rev. B, **42**, 1533.

[43] G. L. Bona, F. Meier, M. Taborelli, E. Bucher and P.H. Schmidt, Solid State Comm., 56, 391 (1985).

[44] J. A. Caballero, Y. D. Park, J. R. Childress, J. Bass, W.-C Chiang, A. C. Reilly, W. P. Pratt Jr., F. Petroff, J. Vac. Sci. Technol. A, **16**, 1801 (1998).

[45] R. Kabani, Ph.D. Thesis, Tufts University (1992) unpublished.

[46] C. T. Tanaka, J. Nowak and J. S. Moodera, J. Appl. Phys., **81**, 5515 (1997).

[47] A. Szytula, Z. Dimitrijevic, J. Todorovic, A. Kolodziejczyk, J. Szelag, A. Wanic, Phys. Stat. Sol. A, **9**, 97 (1972).

[48] R. B. Helmholdt, R. A. de Groot, F. M Mueller, P. G. van Engen and K.H.J. Buschow, J. Magn. and Magn. Mat., **43**, 249 (1984).

[49] P.J. Webster and R.M. Mankikar, J. Magn. Mag. Mater. **42**, 300 (1984).

[50] A. Kimura, S. Suga, T. Shishidou, S. Imada, T. Muro, S.Y. Park, T. Miyahara, T. Kaneko and T. Kanomata, Phys. Rev. B **56**, 6021 (1997).

[51] L. Castelliz, Monatsch. Chem. **83**,1314 (1952); L. , Z. Metallkde **46**, 201 (1955).

[52] R. Kabani, M. Terada, A. Roshko and J. S. Moodera, J. Appl. Phys., **67**, 4898 (1990).

[53] J. A. Caballero, YD Park, A Cabbibo, JR Childress, F. Petroff and R. Morel, J. Appl. Phys. **81**, 2740 (1997).

[54] J. F. Bobo, K. Bessho, F. B. Mancoff, P. R. Johnson, M. C. Kautzky, R. L. White, and B. M. Clemens, Mater. Res. Soc. Symp. Proc. **475**, 21 (1997).

[55] M.C. Kautzky and B.M. Clemens, Appl. Phys. Lett., **66**, 1279 (1995).

[56] J.E. Mattson JE. E.E. Fullerton, C.I. Sowers, S.D. Bader SD, J. of Vac. Sci. & Tech. A, **13**, 276 (1995).

[57] M. Gutsche, H. Kraus H, J. Jochum, B. Kemmather and G. Gutekunst, Thin Solid Films, **248,** 18 (1994).

[58] Y. Ikuhara, P. Pirouz, S. Yadavalli and C.P. Flynn, Phil. Mag. A **72**, 179 (1995).

[59] S.J. Jenkins and G.P. Srivastava, Surf. Sci. **398**, L308 (1998).

[60] S.J. Youn and BI Min, Phys. Rev. B **51**, 10436 (1995).

[61] M.J. Otto, R.A.M. van Woerden, P.J. vanderValk, J. Wijngaard, C.F. vanBruggen, C. Haas and K.H.J. Buschow, J. Phys.: Condens. Matter **1**, 2341 (1989).

[62] B.D. Cullity, *Introduction to Magnetic Materials* (1972).

[63] J.S. Moodera, E.F. Gallagher, K. Robinson and J. Nowak, Appl. Phys. Lett. **70**, 3050 (1997).

[64] W.J. Gallagher, S.S.P. Parkin, L. Yu, X.P. Bian, A. Marley, R.A. Altman, S.A. Rishton, K. P. Roche, C. Jahnes, T.M. Shaw and X. Gang, J. Appl. Phys. **81**, 3741 (1997).

[65] S.I. Park, A. Marshall, R.H. Hammond, T.H. Geballe TH and J. Talvacchio, J. of Mater Res. **2**, 446 (1987).

[66] J.S. Moodera, private communication.

[67] C. Hordequin, J.P. Nozieres and J. Pierre, J. of Magn. Magn. Mater. **183**, 225 (1998).

[68] J. Tersoff and F.K. LeGoues, Phys. Rev. Lett. **72**, 3570 (1994).

[69] W.H. Yang and D.J. Srolovitz, Phys. Rev. Lett. **71**, 1593 (1993).

[70] D.E. Jesson, S.J. Pennycook, J.-M. Baribeau and D.C. Houghton, Phys. Rev. Lett. **71**, 1744 (1993).

[71] K. Matsuda, A. Kamijo, T. Mitsuzuka and H. Tsuge, J. Appl. Phys. **85**, 5261 (1999).

[72] R.J.M. van de Veerdonk, J. Nowak, R. Meservey, J.S. Moodera and W.J.M. de Jonge, Appl. Phys. Lett. **71**, 2839 (1997)

[73] L. Fritzsch, H-J. Koehler, F. Thrum, G. Wende and H-G. Meyer, Physica C **296**, 319 (1998).

[74] N. Cabrera and N.F. Mott, Rep. Prog. Phys. **12**, 163 (1948).

[75] C. Ocal, S. Ferrer and N. Garcia, Surf. Sci. **163**, 335 (1985).

[76] R.J. Soulen Jr., J.M. Byers, M.S. Osofsky, B. Nadgorny, T. Ambrose, S.F. Cheng, P.R. Broussard, C.T. Tanaka, J. Nowak, J.S. Moodera, A. Barry, J.M.D. Coey, Science **282**, 85 (1998)

[77] A. F. Andreev, Zh. Eksp. Teor. Fiz. **46**, 1823 (1964).

[78] G.E. Blkonder and M. Tinkham, Phys. Rev. B **27**, 112 (1983).

[79] M.J.M. de Jong and C.W.J. Beenakker, Phys. Rev. Lett. **74**, 1657 (1995)

[80] B.N. Cox, J. Phys. F: Metal Phys., **9**, 2067 (1979).

[81] A.J. Lapworth and J.P. Jakupovics, Phil. Mag. **29**, 253-73 (1974).

[82] E.A. Fitzgerald, S. Samavedam, Y.H. Xie, and L.M. Giovane, J.Vac. Sci. Tech. A **15**, 1048 (1997).

[83] D. Orgassa, H. Fujiawara, T.C. Schulthess and W.H. Butler, submitted to Phys. Rev. B.

[84] M.J. Otto, R.A.M. van Woerden, P.J. van der Valk, J. Wijngaard, C.F. van Bruggen and C. Hass, J. Phys.: Condens. Matter **1**, 2351 (1989)

[85] D. Orgassa, private communication.

[86] M.C. Kautzky, F.B. Mancoff, J-F. Bobo, P.R. Johnson, R.L. White and B.M. Clemens, J. Appl. Phys. **81**, 4026 (1997).

[87] M.C. Kautzky *et al.* (unpublished).

[88] J.S. Moodera, private communication.

[89] F.B. Mancoff *et al.* (unpublished).

[90] J. Kubler, Physica B&C, **127B+C**, 257 (1984).

[91] J.P. Senateur, A. Rouault, R. Fruchart and D. Fruchart, J. Solid State Chem. **5**, 226 (1972).

[92] X.A. Cao, J.A. Caballero, K.B. Jung, J.W. Lee, S. Onishi, J.A. Childress and S.J. Pearton, Solid State Elec. **42**, 1705 (1998); K.B. Jung KB, J. Hong J, H. Cho, J.A. Caballero JA, J. R. Childress, S.J. Pearton, M. Jenson, A.T. Hurst Jr., Surf. Sci. **138-139**, 111 (1999).

[93] P.A. Stampe and R.J. Kennedy, Thin Solid Films **326**, 63 (1998).

[94] T.H. Kim, C.T. Tanaka and J.S. Moodera, unpublished results.

Biographical Note

Clifford Takashi Tanaka

Education

1996-1999	Ph.D. in Materials Science & Engineering, Massachusetts Institute of Technology, Cambridge, MA *Thesis: "Investigation of Half-Metallic Ferromagnetism in NiMnSb Spin Dependent Tunnel Junctions". Advisor: Dr. J. S. Moodera*
1994-1996	S.M. in Materials Science & Engineering, Massachusetts Institute of Technology, Cambridge, MA *Thesis: "Ferromagnet-insulator-ferromagnet tunneling with one half-metallic electrode". Advisor: Dr. J. S. Moodera*
1990-1994	B.S. in Physics with Honors, Carnegie Mellon University, Pittsburgh, PA

Awards/Honors

1999	Navy Alan Berman Research Publication award
1998	Best Student Presentation - 43rd Magnetism and Magnetic Materials Conf.
1994	Andrew Carnegie Scholar
1994	Carnegie Mellon Univ., Dept. of Physics Cutkosky Award
1994	NSF Graduate Fellowship, Honorable Mention

List of Publications

Growth and characterization of epitaxial NiMnSb thin films
C.T. Tanaka, J. Nowak, R. Jansen and J.S. Moodera (in preparation)

Spin-polarized tunneling studies of a half-metallic ferromagnet
C.T. Tanaka, J. Nowak and J.S. Moodera, submitted to J. Appl. Phys.

Spin polarized tunneling
J.S. Moodera, T.H. Kim, C.T. Tanaka and C.H. deGroot, to appear in Phil. Mag. 1999

Formation of doped Al_2O_3 tunnel barriers by plasma oxidation of δ-doped Al
R. Jansen, B. Davis, C.T. Tanaka and J.S. Moodera, submitted to J. Appl. Phys.

Andreev reflection: a new means to measure the spin polarization of ferromagnetic materials
R.J. Soulen Jr., M.S. Osofsky, B. Nadgorny, T. Ambrose, P. Brussard, S.F. Cheng, J. Byers, C.T. Tanaka, J. Nowak, J.S. Moodera, G. Laprade, A. Barry and M.D. Coey, J. Appl. Phys. **85**, 4589 (1999).

Dielectric tensor for magneto-optic NiMnSb
X. Gao, J.A. Woollam, R.D. Kirby, D.J. Sellmyer, C.T. Tanaka, J. Nowak and J.S. Moodera, Phys. Rev. B **59**, 9965 (1999).

Cluster-based Monte Carlo simulation of ferrofluids
S.W. Davis, W. McCausland, H.C. McGahagan, C.T. Tanaka and M. Widom, Phys. Rev. E, **59**, 2424-8 (1999).

Measuring the spin polarization of a metal with a superconducting point contact
R.J. Soulen Jr., J.M. Byers, M.S. Osofsky, B. Nadgorny, T. Ambrose, S.F. Cheng, P.R. Broussard, C.T. Tanaka, J. Nowak, J.S. Moodera, A. Barry and J.M.D. Coey, Science, **282**, 85-8 (1998).

Magnetoresistance in ferromagnet-insulator-ferromagnet tunnel junctions with half-metallic ferromagnet NiMnSb compound
C. T. Tanaka, J. Nowak and J. S. Moodera, J. Appl. Phys., **81**, 5515-17 (1996)

Calculation of magnetic moments in Ho_2C_3 nanocrystals
S. A. Majetich, J.O Artman, C. Tanaka and M. E. McHenry, J. Appl. Phys., **76**, 6307-9. (1995)

1599-53